Distance Measurement in Air with a Femtosecond Frequency Comb Laser

Proefschrift

ter verkrijging van de graad van doctor
aan de Technishe Universiteit Delft,
opgezag van de Rector Magnificus prof. ir. K. C. A. M. Luyben,
voorzitter van het College voor Promoties,
in het openbaar te verdedigen op maandag 11 oktober 2010 om 10:00 uur

door

Moxi Cui

Master of Science
Delft University of Technology
geboren te Beijing, China

Dit proefschrift is goedgekeurd door de promotor:
Prof. dr. ir. H. P. Urbach.

Copromotor:
Dr. N. Bhattacharya.

Samenstelling promotiecommissie:

Rector Magnificus,	voorzitter
Prof. dr. H.P. Urbach,	Technische Universiteit Delft, promotor
Mw. dr. N. Bhattacharya,	Technische Universiteit Delft, copromoter
Prof. dr. ir. J.J.M. Braat,	Technische Universiteit Delft
Dr. S.A. van den Berg,	VSL
Prof. dr. ir. M.K. Smit,	Technische Universiteit Eindhoven
Prof. ir. R.H. Munnig Schmidt,	Technische Universiteit Delft
Prof. dr. ir. H.B. van Linden van den Heuvell	Universiteit van Amsterdam

The work described in this thesis was performed at the Faculty of Applied Sciences, Department Imaging Science and Technology, Optics Research Group, Technische Universiteit Delft, The Netherlands. The experimental work was mainly performed at VSL, Delft, The Netherlands. This work is part of the Industrial Partnership Programme "Metrology with frequency comb lasers" of the Stichting voor Fundamenteel onderzoek der Materie (FOM). It is supported and co-financed by VSL as part of the VSL metrological research programme, which is funded by the Ministry of Economic Affairs of The Netherlands.

Copyright © 2010 by M. Cui

All rights reserved. No part of this publication may be reproduced, stored in a retrieval system or transmitted in any form or by any means: electronic, mechanical, photocopying, recording or otherwise, without prior written permission of the author.

Contents

1 Introduction **1**
- 1.1 Background: The evolution of ultrashort pulses . . . 1
- 1.2 Frequency comb metrology: A ruler on frequency, time and distance . . . 2
- 1.3 Distance measurements using lasers . . . 2
- 1.4 Inter-satellite distance metrology . . . 3
  - 1.4.1 Grace . . . 3
  - 1.4.2 Darwin/TPF . . . 3
  - 1.4.3 Lisa/BBO . . . 4
- 1.5 Goal of our research and the outline of this thesis . . . 4

2 Distance Measurement Interferometry **5**
- 2.1 Laser interferometry . . . 5
  - 2.1.1 Single wavelength interferometry . . . 5
  - 2.1.2 Multiple wavelength interferometry . . . 6
  - 2.1.3 Frequency sweeping interferometry . . . 8
- 2.2 White-light interferometry . . . 10
  - 2.2.1 Coherence length . . . 10
  - 2.2.2 White-light interferometry . . . 10
  - 2.2.3 White-light channeled spectrum interferometer . . . 10
- 2.3 Determination of the refractive index . . . 12
  - 2.3.1 Refractive index of air . . . 12
  - 2.3.2 Refractive index of other media . . . 14

3 Stabilized femtosecond ultrashort pulse **15**
- 3.1 Time and frequency domain pictures of a pulse train . . . 15
- 3.2 Femtosecond pulse generation . . . 16
  - 3.2.1 A brief history of mode locking . . . 16
  - 3.2.2 The Ti:Sapphire mode locked femtosecond laser . . . 17
- 3.3 Femtosecond pulse propagation . . . 18
  - 3.3.1 Group velocity dispersion . . . 18
  - 3.3.2 Self-phase modulation . . . 21
- 3.4 Femtosecond pulse characterization . . . 21
  - 3.4.1 Field autocorrelation . . . 21
  - 3.4.2 Intensity autocorrelation . . . 22
  - 3.4.3 Fringe resolved autocorrelation . . . 23
  - 3.4.4 SPIDER . . . 24
  - 3.4.5 FROG . . . 24
- 3.5 Using the femtosecond frequency comb for distance interferometry . . . 24

4 Linear Technology of ultrashort pulse detection **27**
4.1 General introduction to linear measurement techniques . . . 27
4.2 First order cross correlations: linear detection in time . . . 29
4.2.1 Mathematical analysis of the cross correlation . . . 29
4.2.2 The cross correlation functions of a symmetric power spectral density . . . 31
4.2.3 The cross correlation functions from an asymmetric power spectral density . . . 34
4.3 Spectral interferogram: linear detection in frequency . . . 34
4.3.1 Mathematical analysis of the spectral interferogram . . . 37
4.3.2 The spectral interferogram of a symmetric power spectral density . . . 39
4.3.3 The spectral interferogram of an asymmetric power spectral density . . . 42
4.4 Relation between the cross correlation and the spectral interferogram . . . 44
4.4.1 The difference between the position of the maximum of the cross correlation function and the multiple of the inter-pulse distance . . . 44
4.4.2 The spectrogram . . . 46

5 Distance measurement using correlations **49**
5.1 Cross correlations in an unbalanced Michelson interferometer . . . 49
5.2 Measurement of short distances using cross correlations . . . 50
5.2.1 Experimental setup . . . 50
5.2.2 Measurement procedure . . . 51
5.2.3 Measurement results . . . 52
5.3 Measurement of long distances with cross correlations . . . 53
5.3.1 Experimental setup . . . 53
5.3.2 Modifications implimented in the experimental setup . . . 55
5.3.3 Measurements procedure . . . 56
5.3.4 Numerical model for analysis . . . 57
5.3.5 Cross correlations up to 200 m propagation in air . . . 60
5.3.6 Measurement results . . . 60

6 Distance measurement in frequency domain **65**
6.1 Spectral interferograms in an unbalanced Michelson interferometer . . . 65
6.2 Measurement of short distances with spectral interferograms . . . 66
6.2.1 Experimental setup and measurement principle . . . 66
6.2.2 A new calibration approach . . . 69
6.2.3 Measurement procedure . . . 70
6.2.4 Measurement results . . . 72
6.2.5 Resolution of the the grating spectrometer . . . 73
6.2.6 Influence of the grating spectrometer resolution on distance measurement . . . 73
6.3 Measurement of long distances with spectral interferograms . . . 75
6.3.1 Experimental setup and measurement procedure . . . 75
6.3.2 Numerical model for analysis . . . 77
6.3.3 Calculate the displacement using more frequencies . . . 79
6.3.4 Spectral interferograms at 100 m path length differences . . . 80
6.3.5 Measurement results . . . 80

7 Conclusion **83**

Nomenclature **85**

Bibliography **87**

Summary **95**

Samenvatting **97**

Acknowledgments **99**

Curriculum Vitae **101**

List of Publications **103**
Refereed publications 103
Conference presentations 103
Poster presentations (1st author only) 104
Magazines 104

Chapter 1

Introduction

1.1 Background: The evolution of ultrashort pulses

This thesis is written in the year 2010, which marks the 50th anniversary of the birth of the laser. In 1960, Theodore H. Maiman constructed the first laser at Hughes Research Laboratories, Malibu, California [1]. The first laser used a solid-state flash lamp-pumped ruby crystal to produce red light at 694 nm. Later in 1960, Ali Javan, and William R. Bennett constructed the first gas laser, using helium-neon, that was capable of continuous operation [2]. In 1970, Zhores Alferov in the USSR, Izuo Hayashi and Morton Panish of Bell Telephone Laboratories, independently developed the first room-temperature, continuous operation diode laser with a heterojunction structure [3, 4]. In the following 40 years, lasers are being used in carrying out business, health care and communication all over the world. Nowadays, we use lasers to read and write CDs and DVDs, to guide commercial aircrafts, and provide worldwide communications. All these applications take advantage of the distinctive properties of laser light: monochromatic, directional and coherent.

One of the most important development in the history of the laser is the invention of short pulsed lasers. Unlike continuous wave lasers, pulsed lasers emit very narrow pulses where very high peak powers can be achieved. An ultra short pulsed laser is a laser that emits ultrashort pulses, whose durations are on the order of the femtosecond (10^{-15} s). In the 1970's, a few hundred femtosecond pulses were generated in passively mode-locked dye lasers [5]. In the 1980 and 1990's, Ti:Sapphire crystal became the most widely used source of ultra short pulsed lasers and pulses could be generated from a few hundreds of femtoseconds to a few tens of femtoseconds, depending on the configuration of the laser [6]. Titanium Sapphire has not only good thermal and mechanical properties, but also tuning range as large as 500 nm. Alongside this, new mode-locking mechanisms were developed. Kerr lens mode locking was first reported in 1991 and in a few years, pulses as short as a few femtoseconds were generated [7]. In 1999, the self-referenced phase stabilization technique was first reported by two groups simultaneously [8, 9]. In 2005, the Nobel prize was awarded to Theodor W. Hänsch and John L. Hall who were the key people in each of these groups which made this discovery. A phase-stabilized femtosecond laser generates a long train of pulses who have fixed inter-pulse distances and phase relations. This stabilized pulse train corresponds to a frequency comb in the spectrum, with very narrow and accurate comb lines. The invention of the frequency comb opened up a new era of ultrafast measurement techniques.

1.2 Frequency comb metrology: A ruler on frequency, time and distance

To most people in the world, one second is simply a "tick" on the clock. But to the physicist, the definition of this "tick" has never been easy. Before the 1960s, the definition of the second was based on the motion of the earth: one second was defined as 1/86400 of the average time required for the earth to complete one rotation about its axis or a day. However, the definition of "a day" is not easy. Astronomical observations revealed that the period of earth's rotation is also changing slightly over the years. Thus the motion of the earth can not be considered a suitable standard to define the unit of time.

At the 13th General Conference on Weights and Measures in 1967, the second obtained a new definition taking advantage of the invention of atomic clocks. A second was defined as "the duration of 9,192,631,770 periods of the radiation corresponding to the transition between the two hyperfine levels of the ground state of the cesium 133 atom". Up to now, the best cesium fountain atomic clock is NIST-F1, located at the National Institute of Standards and Technology in the United States of America. Its accuracy is better than one second in more than 60 million years [10].

A frequency comb allows a direct link from the microwave frequency of a cesium clock to optical frequencies. A stabilized frequency comb has a wide spectrum spanning an octave of wavelengths, with equidistant lines separated by the repetition frequency of the laser. All the frequencies in the comb are tracable to the reference clock. A frequency comb can thus be used as an optical ruler to measure:

- **Optical frequency** If the comb frequencies are known, any optical frequency that falls within the bandwidth of the comb can be measured by measuring the beat frequency of the unknown optical frequency and the frequency comb. The beat notes reveal the difference in frequency between the unknown frequency and the comb frequencies [8, 11–13].

- **Time interval** Most events in atoms and molecules occur on fs and ps time scales. Ultrafast spectroscopy involves studying ultrafast events that take place in a medium by using ultrashort pulses and delays for time resolution. Here the femtosecond laser works as a super high speed illumination and detection system, which diagnoses and resolves ultrafast phenomena, such as the dynamics of biological molecules [14, 15].

- **Distance** In the 17th General Conference on Weights and Measures in 1983, the meter is defined as the distance traveled by light in free space in 1/299792458 of a second. The connection between the definition of meter and the cesium clock makes the frequency comb a promising tool for distance measurement [16, 17].

1.3 Distance measurements using lasers

In distance measurement, accuracy, ambiguity range, coherence length of the source, complexity of the system, measurement speed and absolute or incremental characters, are all important considerations during the selection of a certain technique. Since the laser could be used for measuring distances, a huge range of applications led to many different techniques depending upon the applications. For example, measuring the distance between satellites in low earth orbit needs high

accuracy, absolute measurement and most important, with a simple system because the room on a satellite is dramatically limited. The frequency sweeping interferometry is more fit for this task since it uses only one laser. For long distance measurements in atmosphere, the complexity of the system becomes less important, but the turbulence of the refractive index of air has to be taken into account. Thus multiple wavelength interferometry becomes more powerful for its large choice of synthetic wavelengths. The white light interferometry can achieve nanometer accuracy, but the coherence length of the source is very short. This makes it especially good for measuring the roughness of the sample surface, normally in the order of micrometers.

When the femtoseond frequency comb laser was invented, the combination of femtosecond technique with the traditional interferometry opened up a new chapter on distance metrology. On one hand, the femtosecond frequency comb can be viewed as a multi-wavelength source. There are around 10^5 stabilized wavelengths equally spanning a whole frequency range. The ambiguity range is the inter-pulse distance, around 1 m for a typical femtoscond pulse laser. On the other hand, because of the broad spectrum, the femtosecond laser can also be considered as a white light source, but with very long coherence length [18]. The line width of the femtosecond laser is less than 10 kHz for a normal Ti:Sapphire laser, corresponding to a coherence length of more than 10 km [18, 19].

1.4 Inter-satellite distance metrology

In recent times, many science missions are being proposed and carried out in outer space. For this, satellites have to fly in formation in space. The launching, deployment and final commissioning of these satellites plays huge demands on the metrology systems.

1.4.1 Grace

Satellite arrays are used for instruments that are too large to fit on a single satellite. By using a combination of metrology and closed loop control of the formation, it becomes possible to form a much larger, virtual structure. Very high accuracy distance measurements are needed for some satellites that fly in close formation and cooperate constantly. One of the great successes is the Grace mission, launched in 2002, which tries to measure the gravitational field of the earth [20]. The mission used a microwave ranging system to accurately measure changes in the speed and distance between two identical spacecraft flying in a polar orbit about 220 kilometers apart, 500 kilometers above Earth. The ranging system is so sensitive it can detect separation changes as small as 10 μm, about one-tenth the width of a human hair over a distance of 220 kilometer.

1.4.2 Darwin/TPF

An intriguing question is whether there are earth-like planets outside of our solar system. Traditional ways to find exo-planets are normally indirect detection methods, such as measuring the Doppler shift in the optical spectrum of the star. Direct detection methods to find the exo-planet are difficult, mainly because the planet is much smaller and darker than its parent star. Darwin is the planned space mission from the European space agency (ESA) to investigate exo-planets using aperture synthesis in the far infrared [21]. In the Darwin mission, three free-flying space telescopes, each three to four meters in diameter, will fly in formation as an astronomical interferometer. These

telescopes will collect light from distant stars and planets and recombine it interferometrically onto a fourth spacecraft, which would carry the beam combiner, spectrometers, and cameras. In 2002, National agency National Aeronautics and Space Administration (NASA) proposed a similar mission called TPF (Terrestrial Planet Finder). Multiple small telescopes on a fixed structure or on separated spacecraft floating in precision formation would simulate a much larger, very powerful telescope.

1.4.3 Lisa/BBO

High accuracy distance measurement among satellites are required when the scientific mission is to detect the gravitational wave. The Laser Interferometer Space Antenna (LISA) mission is to detect and observe, in detail, gravitational waves from astronomical sources [22]. LISA is intended to measure gravitational waves by using laser interferometry over astronomical distances. It will use three spacecraft arranged in an equilateral triangle to form a giant Michelson interferometer with arms about 5 million kilometers long. When a gravitational wave disturbs the space-time field between two of the spacecraft, small differences in the relative lengths of the arms should be measurable. A proposed successor of LISA will be the Big Bang Observer (BBO), who will observe the gravitational waves from the time shortly after the Big Bang. The proposed instrument is a collection of four instruments like LISA, each composed of three spacecraft flown in a triangular pattern.

1.5 Goal of our research and the outline of this thesis

In this thesis, we will investigate the possibility for long distance measurement by using a stabilized femtosecond pulsed laser. The expected accuracy is in the order of 10^{-8}. During this thesis, we measured a path length up to 100 m on a 50 m bench in the lab of VSL. The accuracy is around one micron, limited by the influnce of air turbulence. The phenomenon of propagating ultra short pulses in dispersive media will be investigated.

We start from an overview of all the coherent distance measurement techniques in Chapter 2. In Chapter 3, we will give an introduction to ultrashort pulses and investigate the possibility to use the stabilized femtosecond pulses as a tool for long distance measurement. Chapter 4 is a general description for linear measurement techniques for ultrashort pulses. This is the most important part of this thesis because it will bring us to two different measurement methods, based on measuring cross correlations and spectral interferograms respectively. The experiments will be further discussed and tested in Chapter 5 and Chapter 6 for the two methods. Chapter 7 contains the conclusion and discussion.

Chapter 2

Distance Measurement Interferometry

An optical interferometer is an optical instrument which combines two or more light waves to give interference. The interference can be achieved by using different optical configurations, for example, Mach-Zehnder, Michelson, Sagnac or Twymann-Green interferometers. The most commonly used interferometer for displacement measurement is the Michelson interferometer. It is composed of a single beam splitter which is used for dividing the beam into two arms: a fixed reference arm and a movable measurement arm. The two beams travel over two different paths and recombine at the detector. The quasi-monochromatic continuous wave laser such as HeNe laser is often used as the source of the Michelson interferometer. However, compact and low-cost Michelson interferometers were developed by using stabilized laser diodes as light sources, normally with shorter coherent lengths.

Optical Interferometer can provide extreme precise measurements of distance, displacement and shapes of surfaces [23, 24]. Interferometry has been very important for precise distance measurement. The high accuracy is provided by interference giving rise to periodic variation of intensity with optical path changes, for example from the displacement of a mirror in the interferometer. The period of the variation corresponds to a change in optical path by one wavelength, λ, which is about $1/2$ μm when visible light is used. By careful measurement and analysis of the interference fringes, measurement uncertainties of less than $1/1000$ of a fringe can be achieved. However, the accuracy will be further limited by the practical realizations, e.g., the interferometer alignment or the drift of optical components.

2.1 Laser interferometry

2.1.1 Single wavelength interferometry

Although most lasers generate Gaussian beams, we will approximate the beam by a plane wave to simplify the calculation. The complex form of a plane wave before entering the interferometer is,

$$E(t)|_{l=0} = 2|E|e^{-i(\omega_0 t+\phi_0)} \tag{2.1}$$

where $|E|$ is the scalar amplitude, ω_0 is the optical frequency and ϕ_0 is the initial phase. Suppose the distance of the reference arm and the measurement arm is l_r and l_m respectively, and the intensities

of both arms are equal. Ignoring the absorption of the media, we have,

$$E_m(t, l_m) = |E|e^{-i(\omega_0 t - 2kl_m + \phi_0)} \qquad E_r(t, l_r) = |E|e^{-i(\omega_0 t - 2kl_r + \phi_0)} \tag{2.2}$$

where k is the wave vector. Here the factor 2 comes from the back and forth propagation of the light. Within this thesis, we always use small l to denote the length of an arm of the interferometer and capital L to denote the path length of the light, or the path length difference in a Michelson interferometer.

$$k = 2\pi n_0/\lambda_0 \tag{2.3}$$

with λ_0 the wavelength in vacuum and n_0 the refractive index at λ_0 . The detected combined intensity is,

$$I(L) = |E_m + E_r|^2 = 2|E|^2(1 + \cos\Delta\phi_0) \tag{2.4}$$

Here the phase difference of the two beams returning from both arms is,

$$\Delta\phi_0 = 2k(l_m - l_r) = \frac{2\pi n_0 L}{\lambda_0} \tag{2.5}$$

where $L = 2(l_m - l_r)$ is the path-length difference between the two arms. Substitute Eq. 2.5 into Eq. 2.4, we have,

$$I(L) = 2|E|^2\left[1 + \cos(2\pi n_0 L/\lambda_0)\right] \tag{2.6}$$

The intensity will therefore depend on the optical path difference between the two arms of the interferometer.

Due to the short wavelengths of visible light, the sensitivity of a single wavelength interferometric measurement using visible light is very high. Accuracy better than 10 nm can be obtained by using commercially available interferometers. One disadvantage of such interferometers is that the non-ambiguity range is also limited to the optical wavelength. The consequence of the short non-ambiguity range is the incremental manner of measuring: the reflector has to be moved over the entire length to be measured and must remain fairly accurately in the required path during the movement. This may sometimes be inconvenient or difficult, particularly at very long distances.

2.1.2 Multiple wavelength interferometry

An excellent solution to increase the non-ambiguity range is performing the measurement at more than one wavelength [25]. The true distance is then obtained by comparing the measurement results of different wavelengths. Let us first consider an interferometer that uses two different wavelengths at λ_1 and λ_2. Suppose the initial beams of wavelength λ_1 and λ_2 are,

$$E_1(t)|_{l=0} = 2|E_1|e^{-i(\omega_1 t + \phi_1)} \quad E_2(t)|_{l=0} = 2|E_2|e^{-i(\omega_2 t + \phi_2)} \tag{2.7}$$

where, $|E_1|$, ω_1 and ϕ_1 are the scalar amplitude, optical frequency and the initial phase corresponding to λ_1. The symbols $|E_2|$, ω_2 and ϕ_2 have the same for wavelength λ_2. Suppose the beam splitter is 50-50% and the absorption is ignored, the light coming back from both arms are,

$$E_{1r}(t, l_r) = |E_1|e^{-i(\omega_1 t + \phi_1 - 2k_1 l_r)} \quad E_{1m}(t, l_m) = |E_1|e^{-i(\omega_1 t + \phi_1 - 2k_1 l_m)}$$
$$E_{2r}(t, l_r) = |E_2|e^{-i(\omega_2 t + \phi_2 - 2k_2 l_r)} \quad E_{2m}(t, l_m) = |E_2|e^{-i(\omega_2 t + \phi_2 - 2k_2 l_m)} \tag{2.8}$$

where k_1 and k_2 are the wave vectors corresponding to λ_1 and λ_2. Both reflected beams are focused onto a slow detector. The averaged interference signal becomes

$$I(l_r, l_m) = \left\langle |E_{1r} + E_{1m} + E_{2r} + E_{2m}|^2 \right\rangle = \left\langle (E_{1r} + E_{1m} + E_{2r} + E_{2m})(E_{1r} + E_{1m} + E_{2r} + E_{2m})^* \right\rangle \tag{2.9}$$

The brackets <> denote the time average. The expansion of Eq. 2.9 contains 16 terms. But due to the time averaging, all the cross terms containing both wavelengths, such as $E_{1r}E_{2r}^{*}$ or $E_{2m}E_{1r}^{*}$, are zero. Eventually, we have,

$$I(L) = 2|E_1|^2(1+\cos\Delta\phi_1) + 2|E_2|^2(1+\cos\Delta\phi_2) \tag{2.10}$$

where,

$$\Delta\phi_1 = 2\pi n_1 L/\lambda_1 \quad \Delta\phi_2 = 2\pi n_2 L/\lambda_2 \tag{2.11}$$

Here n_1 and n_2 is the refractive index at λ_1 and λ_2 respectively. Eq. 2.10 is simply the incoherent superposition of the individual interference signals for λ_1 and λ_2. The intensity $I(L)$ shows a beat frequency of the optical path difference. To see this, we suppose the wavelength λ_1 and λ_2 are close to each other, let us define,

$$\frac{2}{\lambda_0} = \frac{1}{\lambda_1} + \frac{1}{\lambda_2} \tag{2.12}$$

If $|E_1| = |E_2| = |E|$, then Eq. 2.10 becomes,

$$I(L) = 4|E|^2 + 2|E|^2\left(\cos\Delta\phi_1 + \cos\Delta\phi_2\right) = 4|E|^2\left[1+\cos\left(\frac{\Delta\phi_1+\Delta\phi_2}{2}\right)\cos\left(\frac{\Delta\phi_1-\Delta\phi_2}{2}\right)\right] \tag{2.13}$$

By substituting Eq. 2.11 into Eq. 2.13, we have,

$$I(L) = 4|E|^2\left\{1+\cos\left[\pi n_0 L\left(\frac{2}{\lambda_0}\right)\right]\cos\left[\pi n_0 L\left(\frac{1}{\lambda_1}-\frac{1}{\lambda_2}\right)\right]\right\} \tag{2.14}$$

Here n_0 is the refrective index at λ_0. By defining the synthetic wavelengths,

$$\frac{2}{\Lambda_0} = \left|\frac{1}{\lambda_1}-\frac{1}{\lambda_2}\right| \tag{2.15}$$

we can write,

$$I(L) = 4|E|^2\left[1+\cos(2\pi n_0 L/\lambda_0)\cos(2\pi n_0 L/\Lambda_0)\right] \tag{2.16}$$

Here, the phase difference is sensitive to a new synthetic relatively long wavelength Λ_0, rather than the optical wavelength λ_1 and λ_2. Therefore, compared with the single wavelength interferometer, the non-ambiguity length is now increased to the synthetic wavelength, which is longer than both optical wavelengths. Figure. 2.1 shows the interference signal as a function of L for two wavelengths at λ_1=800 nm and λ_2=850 nm. The beat signal is shown in Fig. 2.1-c).

However, the sensitivity of the measurement is reduced when the measured length $L/2$ is calculated by only using the synthetic wavelength. To overcome this problem, it is effective to use the synthetic wavelength for calculation of the fringe order of the optical wavelengths and benefit from the lower uncertainty of the latter for the length measurement. In this case the measurement uncertainty with the synthetic wavelength must not exceed one quarter of the optical wavelength to get the correct fringe order. The maximum possible synthetic wavelength is therefore limited.

The non-ambiguity length can be further increased by adding lasers with more wavelengths [26]. For more than three wavelengths, suppose the amplitude of the n-th wavelength is E_n, the optical frequency is ω_n, the initial phase is ϕ_n and the wave vector is k_n, Eq. 2.9 can be now written as,

$$\begin{aligned} I_\omega(l_r,l_m) = &\left(\sum_{n=1}^{N}|E_n|e^{i\phi_n}e^{i(\omega_n t-2k_n l_r)} + \sum_{n=1}^{M}|E_n|e^{i\phi_n}e^{i(\omega_n t-2k_n l_m)}\right) \\ &\left(\sum_{n=1}^{N}|E_n|e^{-i\phi_n}e^{-i(\omega_n t-2k_n l_r)} + \sum_{n=1}^{N}|E_n|e^{-i\phi_n}e^{-i(\omega_n t-2k_n l_m)}\right\rangle \end{aligned} \tag{2.17}$$

where N is the total number of wavelengths used. The expansion of Eq. 2.18 has N^2 terms, but similarly as in the two wavelengths case, the slow detector reads only the averged interference signal, which leaves only $4\times N$ non-zero terms,

$$\langle I(L)\rangle = 2\sum_{n=1}^{N}|E_n|^2(1+\cos\Delta\phi_n) \tag{2.18}$$

where

$$\Delta\phi_n = 2\pi n(\lambda_n)L/\lambda_n \tag{2.19}$$

Within this thesis, the frequency mode number is always labelled by n. The refrective index always appears with footnotes or as a function of the frequency ω or wavelength λ hence can always be distinguished with the mode number. Again, $L = 2(l_m - l_r)$ is the path length difference between the two arms.

Normally speaking, for more than three wavelengths, there are many synthetic wavelengths. Starting from the longest one, each synthetic wavelength is used to get the fringe order of the next shorter one and finally that of the optical wavelength. But there are some practical difficulties with using more than two lasers. The system becomes complex and the multiplex detection of different wavelengths is difficult.

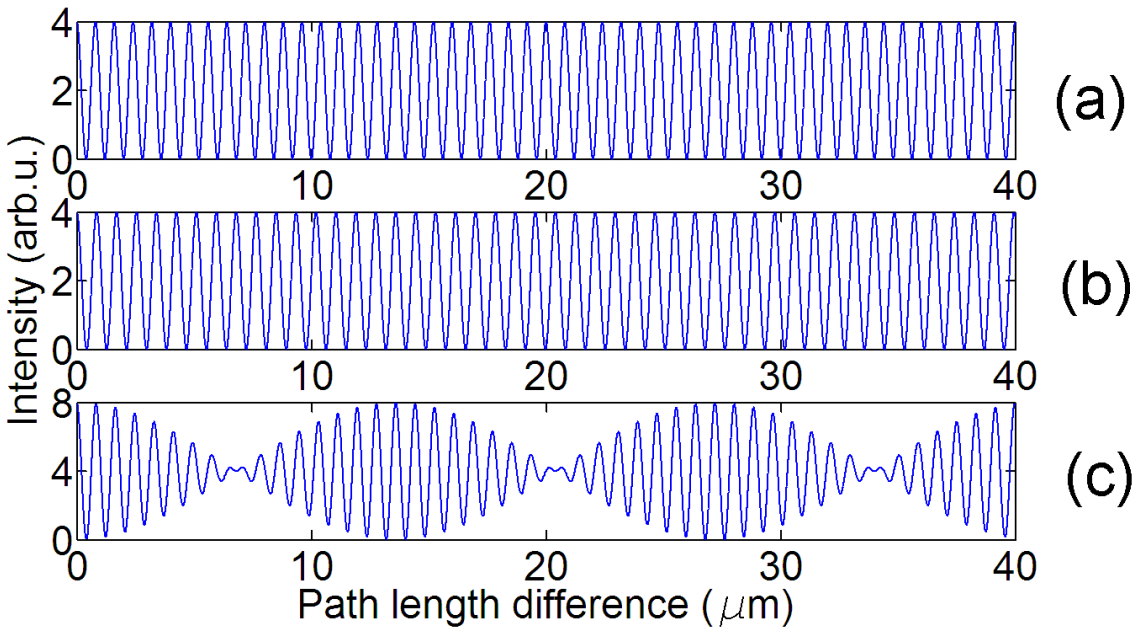

Figure 2.1: (a) Interference signal as a function of the optical path difference L using one wavelength at 800 nm, (b) Interference signal using one wavelength at 850 nm and (c) Interference signal obtained by using both wavelengths.

2.1.3 Frequency sweeping interferometry

In multiple wavelength interferometry, the synthetic wavelength is generated using two or more optical wavelengths. Another way to solve the ambiguity problem of the single wavelength interferometry is using a tunable laser as source. This technique is called frequency-sweeping interferometry

(FSI). The key difference between the frequency sweeping interferometry and the two wavelength interferometry is that, in frequency sweeping interferometry, the phase ϕ is measured continuously during the frequency sweeping from λ_1 to λ_2. Unwrapping this phase yields the full phase difference $\Delta\phi$ without any modulo 2π uncertainty. Compared to the multiple wavelength interferometry, FSI relies only on a tunable laser and a frequency-sweep range measurement subsystem. If the change of the refrective index can be ignored, the maximum synthetic wavelength Λ is inversely proportional to the frequency sweep range $\Delta\omega$:

$$\Lambda = \frac{2\pi c}{n_c \cdot \Delta\omega} \tag{2.20}$$

where n_c means the refractive index at the center of the sweeping range. Normally, the frequency sweep range is measured by a Fabry-Perot interferometer by counting the resonances of the cavity. The sweep begins from a particular cavity mode and during the sweeping, the number of resonances is detected and counted. The frequency sweep range is given by,

$$\Delta\omega = 2\pi r \cdot FSR \tag{2.21}$$

where FSR is the free spectral range of the Fabry-Perot cavity and r is the number of FSR detected. While the frequency is swept, detection electronics counts the number of fringe periods and also the remaining fractional part. The measured length is given by

$$\frac{L}{2} = \left(N_0 + \frac{\phi}{2\pi}\right) \cdot \frac{\Lambda}{2} \tag{2.22}$$

where N_0 is an integer and ϕ is the remaining fringe phase. By substituting Eq. 2.18 into Eq. 2.20, we have,

$$\frac{L}{2} = \left(N_0 + \frac{\phi}{2\pi}\right) \cdot \frac{c}{2r \cdot FSR \cdot n_c} \tag{2.23}$$

The optical path length difference is determined directly by counting the interference fringes as the laser wavelength is scanned through a known change. To implement this technique with high accuracy, it needs a laser to offer continuous tuning over a wide wavelength range. Solid state and dye lasers usually have a large tuning range. Recently, the highly coherent and tunable diode lasers have been made more compact, efficient and reliable. They have been successfully used to measure absolute distances [27, 28].

The main drawback of frequency-sweeping interferometry is that, the technique is sensitive to variations of distance drift during the sweep. During the measurement, the fringes in the detector are generated by frequency sweeping, but also, by the changes in distance caused by drift. A path length change of a single optical wavelength during the frequency sweep could therefore be misinterpreted as a path length change of one synthetic wavelength. This will cause the noise error to be multiplied by the amplification factor Λ/λ. This factor could be as large as 10^4 in a normal frequency sweeping interferometry, which means a drift of 1 nm in the measurement arm will introduce an error of 10 μm in the measurement. A first order correction for this was given by Swinkels and coworkers [29]. This drawback makes the frequency sweeping interferometry difficult for measuring a long distance in air because the fringes will be washed out due to the turbulence.

2.2 White-light interferometry

2.2.1 Coherence length

So far we only considered perfectly monochromatic waves. However, even the single mode laser sources have an average emission spectrum which is confined to a narrow band centered about the central frequency. The coherence length can be used for quantifying the degree of temporal coherence as the propagation length over which coherence degrades significantly. The coherence length is related to the spectrum width as,

$$L_c = c \cdot \tau_c = \frac{2\pi c}{\Delta\omega} \tag{2.24}$$

where τ_c is known as coherence time and $\Delta\omega$ is the line width of the light source. The coherence length of the light source is important in an interferometer because it determines the maximum path length difference between the two arms where pronounced interference fringes can be observed.

2.2.2 White-light interferometry

A white light source refers to a light source with a broad optical bandwidth. The light source does not necessarily operate in the visible spectral range, really generating white light. The white light source can be a super luminescent diode, or can be obtained by launching light from a bulb into a single-mode fiber. White-light interferometers are widely used in non-contact surface height measurements on 3D structures. From Eq. 2.22, we can see that, the coherence length of a white light source is fairly small. This means that only when the two arms of the interferometer are close to each other, the coherent fringes can be observed [30]. In order to obtain interference, the white light interferometer is normally made by two independent interferometers. The first one is called the sensing interferometer which has a path-length difference to be measured, which is much longer than the coherence length of the white light source. In the second so called receiver interferometer, the path length difference is compensated and the output light beams are interfered. Suppose the path length differences of the sensing and receiver interferometers are L_s and L_v respectively, we have $L_s >> L_c$ and $L_v >> L_c$, but $|L_s - L_v| < L_c$. When $L_s = L_v$ the interference reaches its maximum, then the measured distance, such as the surface height can be monitored by measuring the change of L_v. The interferogram is then scanned, either mechanically in the temporal regime or electronically with a photo diode array in the spatial regime.

2.2.3 White-light channeled spectrum interferometer

In 1995, Schenell proposed to use the white light source combined with a spectral interferometer [31]. Figure. 2.3 shows the principle of their measurement. The distance $L/2$ to be measured is the difference between the two arms of the Michelson interferometer formed by a beam splitter (BS) and two plane mirrors. The beam of the white-light source (WLS) is collimated into the interferometer and the output light is reflected by a diffraction grating. The diffracted beam is then focused by the lens onto a linear photo diode array (PDA). Suppose the spectrum of the white light source is $\hat{E}(\omega)$, the spectral interference observed by the PDA should be,

$$S(\omega) = 2|\hat{E}(\omega)|^2 \left[1 + \cos\left(\varphi_m - \varphi_r\right)\right] \tag{2.25}$$

where φ_r and φ_m refer to the spectral phase of both arms. The phase difference is given by,

$$\varphi(\omega) = \varphi_m - \varphi_r = \omega n(\omega) L/c \tag{2.26}$$

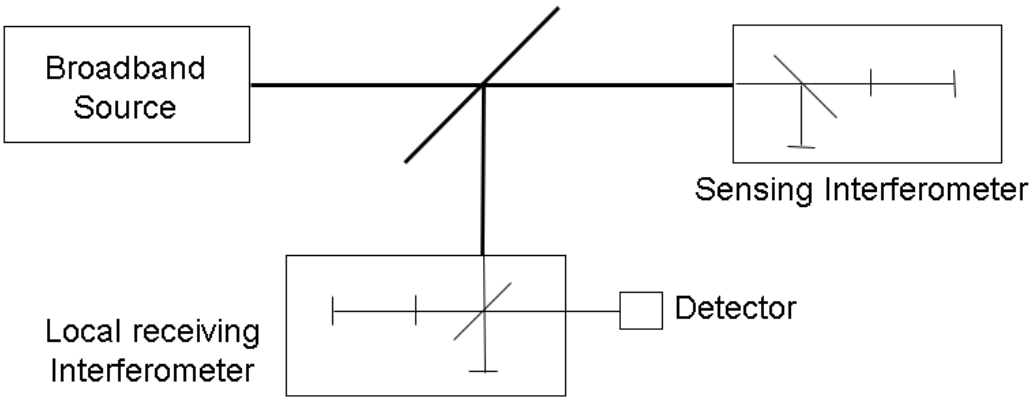

Figure 2.2: Schematic of the experimental setup of the white light interferometer

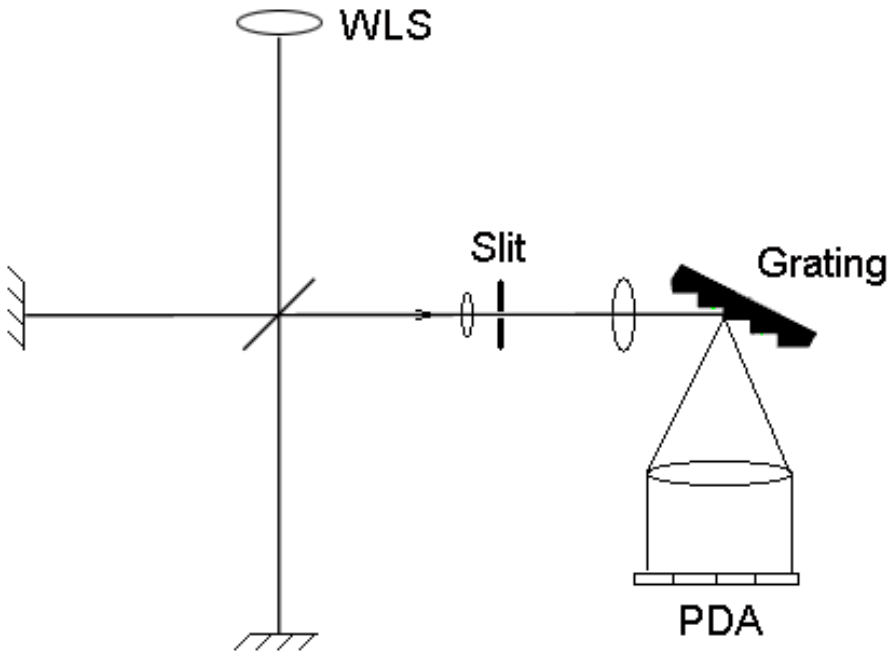

Figure 2.3: Schematic of the experimental setup of the white light channeled spectrum interferometer for absolute distance measurement using a diffraction grating and a photo diode array

with $n(\omega)$ the refractive index as a function of ω and L the path length difference between the two arms. If the refractive index $n(\omega)$ can be approximated by a constant n_c, then $\varphi(\omega)$ is a linear function of ω and the absolute distance L is directly obtained from the slope $d\varphi/d\omega$ through

$$L = \frac{c}{n_c}\frac{d\varphi}{d\omega} \tag{2.27}$$

A typical spectrum interference signal is shown in Fig. 2.4-(a). The spectral amplitude of the white light source is simulated as a Gaussian function, centered at 3.7474×10^{14} Hz (800 nm) with a bandwidth (Full width half maximum) of 1×10^{14} Hz (217 nm). This corresponds to a coherence length of 3 μm. Figure. 2.4-(b) and Fig. 2.4-(c) show the spectral interferences at L equals to 10 μm and 20 μm respectively. We can see that, the modulation depths drop significantly as the measured distance exceeds the coherence length of the white light source. Using a narrower bandwidth white light source can make it possible to measure a longer distance, but more than 1 mm distance can hardly be achieved without using the receiving interferometer.

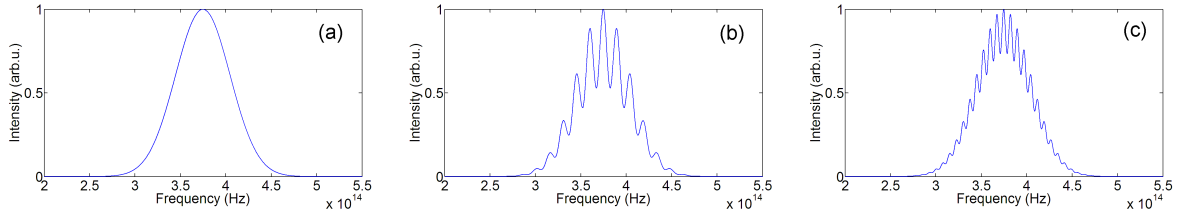

Figure 2.4: (a) Simulation of the power spectral density of a typical white light source. (b) The interference signal at $L = 10$ μm and (c) the interference signal at $L = 20$ μm. The modulation depths drop as the measured distance exceeds the coherence length of the white light source.

2.3 Determination of the refractive index

2.3.1 Refractive index of air

In most distance measurement interferometers, the wavelengths of the light in air are the basic length scales. The wavelength in air is related to the vacuum wavelength by the refractive index,

$$\lambda = \lambda_0 / n_{air} \tag{2.28}$$

The refractive index of normal air differs from 1 by about 2.7×10^{-4}. For interferometric length measurements in air n_{air} has to be determined very accurately. However, uncertainties of the air refractive index smaller than 10^{-8} are only possible under well-defined laboratory conditions using sophisticated instruments for either measurement of environmental parameters together with appropriate equations or optical refractometers.

The physical background of the refractive index of air is based on the Lorenz-Lorentz equation for the refractive index of a mixture of gases [32]:

$$\frac{n_{air}^2 - 1}{n_{air}^2 + 2} = \sum \frac{4}{3}\pi\left(\frac{N_A}{M_i}\right)\alpha_i\rho_i \tag{2.29}$$

where N_A is the Avogadro's number, M_i is the molecular weight, α_i is the polarizability and ρ_i is the partial density of the ith component of the mixture. To calculate the partial density of each

T (°C)	10	15	20	25	30
SVP (mmHg)	9.21	12.79	17.54	23.76	31.8

Table 2.1: The saturated vapor pressure (SVP) of water in air at different temperatures.

component in moist air requires an accurate measured set of the environmental parameters as air pressure, temperature and humidity.

Alternatively to the above-mentioned formalism, there exist a number of empirical equations for the refractive index of air which are called Edlén equations, published by Bengt Edlén in 1966 [33]. K. P. Birch and M. J. Downs added further corrections to the Edlén's equation in 1993 [34] and again in 1994 [35]. The basis of these specialized equations are the precise measurements of the refractive index of air under well-defined laboratory standard conditions, that is, these equations may not be valid in other environmental parameters (e.g., in geodetically length measurement) where Ciddor equation is mandatory [36–38]. In our experiments, we used the Edlén's equations because the experiments were performed in controlled laboratory conditions. According to K. P. Birch and M. J. Downs, the revised form of the Edlén's equations are,

$$(n_{air}-1)_{tp} = \frac{p(n_{air}-1)_s}{96095.43} \times \frac{1+10^{-8}\times(0.601-0.00972T)p}{1+0.0036610T} \tag{2.30}$$

where the unit of pressure is Pa and temperature is °C. $(n-1)_{tp}$ is the refractivity of air at temperature T and atmospheric pressure p and $(n-1)_s$ is given by the revised dispersion equation,

$$(n_{air}-1)_s \times 10^8 = 8342.54 + 2406147\times(130-\sigma^2)^{-1} + 15998\times(38.9-\sigma^2)^{-1} \tag{2.31}$$

where σ is the vacuum wave number in μm^{-1}. For the difference in the refractive index of moist air, containing a partial pressure f of water vapour, and dry air at the same total pressure the following revised expression has been obtained,

$$n_{tpf} - n_{tp} = -f(3.7345 - 0.0401\sigma^2)\times 10^{-10} \tag{2.32}$$

Here the humidity is measured by the partial pressure f. The amount of water vapor in the air at any given time is usually less than that required to saturate the air. The relative humidity is the percent of saturation humidity, generally calculated in relation to saturated vapor density.

$$Relative \quad Humidity = \frac{Actural \quad vapor \quad density}{Saturation \quad vapor \quad density}\times 100\% \tag{2.33}$$

and the saturation vapor density is linked to the partial pressure. Table.2.1 shows the saturated vapor pressure (SVP) at different temperatures around 20°C. In Fig. 2.5 we show a typical variation of n_{air} as a function of frequency at standard environmental conditions, of 20 °C, 1013.25 hPa and 45% humidity.

The uncertainty associated with the Edlén's equations is 1×10^{-8} [39]. Normal fluctuations in conditions such as temperature and air pressure will cause a variation of not much over 10^{-6}. TABLE 2.2 shows the sensitivity of the air refractive index to changes of environmental parameters at standard conditions. A slightly change on enviromental conditions will influence the measured distance. In cases where the distances are so long that variation of n along the path would cause a significant error, then the temperature, pressure and humidity must be measured along the path as well as at the end points. For some distance measurements, instead of a direct determination of n, use is made of

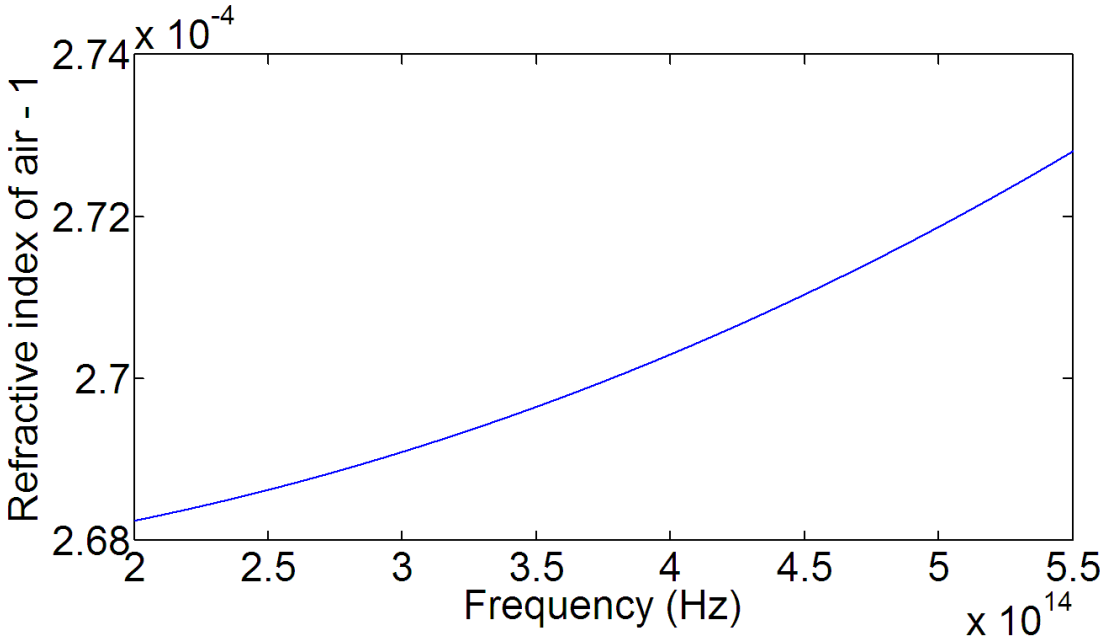

Figure 2.5: Typical variation of n_{air} as a function of frequency at standard environmental conditions, of 20 °C, 1013.25 hPa and 45% humidity.

Influence	Change	Sensitivity in n	Fluctuations at 100 m
Temperature	0.1 °C	-0.95e-7	+9.46 μm
Pressure	1 hPa	+2.70e-7	-26.9 μm
Relative Humidity	1%	-0.08e-7	+0.8 μm

Table 2.2: Sensitivity of the air refractive index to changes of environmental parameters at standard conditions.

a technique whereby one compares the longer distance with a known standard short length through the atmosphere, thus eliminating to first approximation the need for considering n, which tend to be the same over the standard and measured length. For open paths of more than one kilometer, interferometry can hardly be used because rapid fluctuations in the atmospheric density cause the fringes to wash out. Instead, amplitude or polarization modulation of a light beam is used.

2.3.2 Refractive index of other media

In case in one of the arms of the interferometer other kinds of dispersion media, such as water or glass (BK7, flint glass, etc.) are placed, the appropriate refractive index relations have to be used. In this thesis, we performed some typical simulations using BK7. The refractive index equations of BK7 has been taken from the Sellmeier equation [40].

Chapter 3

Stabilized femtosecond ultrashort pulse

3.1 Time and frequency domain pictures of a pulse train

An ultrashort pulse is an electromagnetic field whose time duration is of the order of femtoseconds or even less [41]. Neglecting the spatial dependence, the electric field of an unchirped pulse is given by,

$$E(t) = \sqrt{I(t)}e^{-i(\omega_c t - \phi_0)} \tag{3.1}$$

where ω_c is the carrier frequency, ϕ_0 is the initial phase and $I(t)$ is the pulse intensity. Here, we decomposed an ultrashort pulse into an envelope function and a continuous carrier wave with frequency ω_c. We call the pulse unchirped when the phase of the electric field depends linearly on time. A pulse has a power spectrum that is the shifted Fourier transform of its envelope function so that it is centered at the optical frequency of its carrier. Generally, the width of the spectrum will be inversely proportional to the temporal width of the envelope.

$$\hat{E}(\omega) = \sqrt{S(\omega)}e^{-i\varphi(\omega)} \tag{3.2}$$

Here, $S(\omega)$ is the power spectral density and $\varphi(\omega)$ is the spectral phase.

For a train of identical pulses, separated by a fixed interval L_{pp} in vacuum, the spectrum is a comb of regularly spaced frequencies, with a mutual separation equal to the repetition frequency $f_r = c/L_{pp}$, where c is the speed of light in vacuum. Considering the initial phase of a pulse ϕ_0, there is a phase shift between the peak of the envelope and the closest peak of the carrier wave. As a train of pulses propagates in a dispersive media, the difference between the group and phase velocity will cause a phase increment $\Delta\phi$ from pulse to pulse. This phase shift results in an offset frequency f_0, generally referred to as the carrier-envelope offset (CEO) frequency. The CEO and the repetition frequency are related by $f_0 = (\Delta\phi/2\pi)f_r$. This is illustrated in Fig. 3.1. The comb lines can be written as,

$$f_n = n \cdot f_r + f_0, \tag{3.3}$$

with n the mode number of the frequency comb.

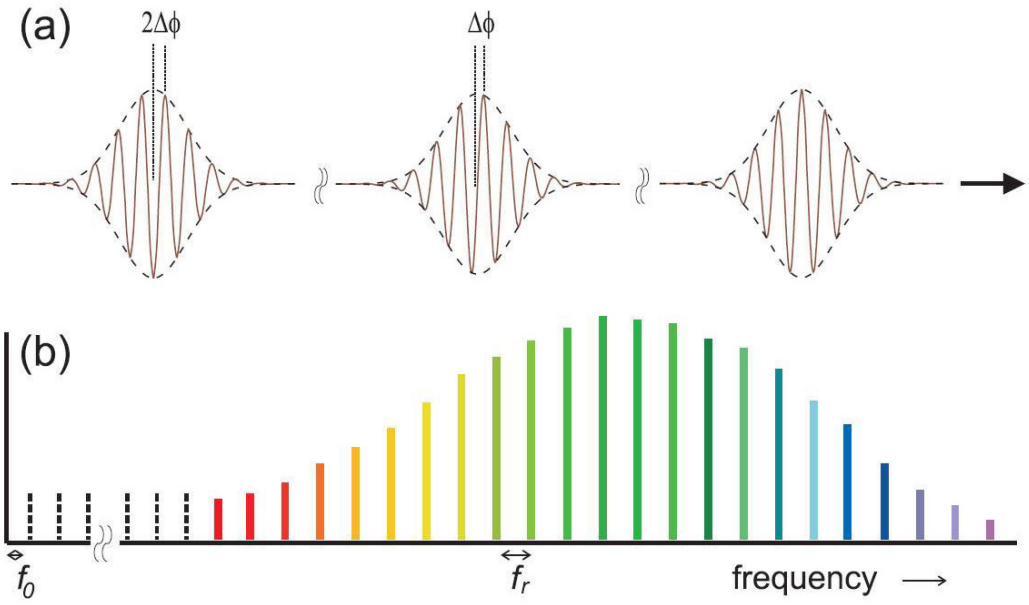

Figure 3.1: a) Illustration of the carrier-envelope phase shift in the time domain. A pulse to pulse phase shift $\Delta\phi$ is observed. b) Corresponding optical frequency spectrum with f_0 the offset frequency due to the carrier-envelope phase shift, and f_r the pulse repetition rate

3.2 Femtosecond pulse generation

3.2.1 A brief history of mode locking

In general, a multimode continuous wave laser oscillates in many spacially different modes. The phases of these modes are unrelated. Since the invention of the solid state laser in the 1960's, people realized that, if the oscillating modes can be forced to have frequencies that are separated by a multiple of a given (repetition) frequency f_r, such that at some instant in time and place they are all in phase, then the mode amplitude will add constructively, resulting in an intensity maximum [42]. The result then is a periodic sequence of short mode-locked pulses separated by time interval $1/f_r$. The width of the pulses will be approximately equal to the inverse of the total bandwidth of the laser output, or $1/Nf_r$, where N is the total number of oscillating laser modes. Mode locking requires a mechanism that results in a higher net gain for short pulses as compared to continuous wave (cw) operation. This mechanism can be either active or passive. Active mode locking means inserting some elements into the laser cavity that sinusoidally modulates the amplitude of the pulse, either by acousto-optic modulation or electro-optic modulation [43]. Because of the limitation of the electronics, active mode-locking can hardly go faster than nanosecond domain. On the other hand, passive mode-locking means inserting some material, e.g. a saturable absorber, into the laser cavity that favors only high intensities [44,45]. The weak pulses are suppressed and the strong pulse is shortened and amplified. The ultimate limit on minimum pulse duration in such a mode-locked laser is due to the interplay between the passive medium, the net gain bandwidth and the group-velocity dispersion (GVD).

Remarkable progress in the generation of femtosecond pulses with solid state lasers has made due to the discovery of the Kerr-lens mode locking (KLM) with a Ti:sapphire crystal in 1991 [6, 7]. The Kerr-lens effect is a phenomenon that a medium's refractive index depends on the light intensity. If the pulse is more intense in the center, it induces a lens. If a pulse experiences additional focusing

due to high intensity and the nonlinear refractive index, and we align the laser for this extra focusing, then a high-intensity beam will have better overlap with the gain medium. In the cavity, losses are too high for a low-intensity cw mode to lase, but not for high intensity femtosecond pulse. This technique makes it possible to generate stable femtosecond pulses [8].

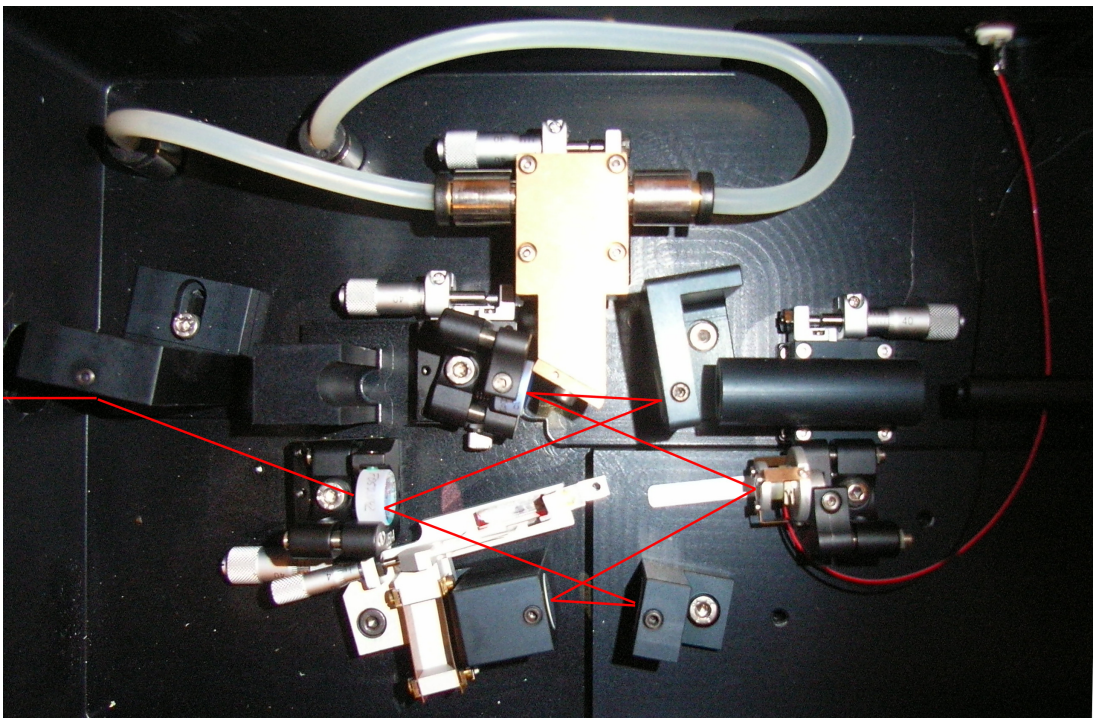

Figure 3.2: The femtosecond laser cavity in VSL. The cavity has a butterfly design, with specially coated chirped mirrors.

3.2.2 The Ti:Sapphire mode locked femtosecond laser

In this section we will introduce the Ti:Sapphire mode locked laser in the laboratory at VSL[1], which we used for all the experiments described in this thesis. The heart of the femtosecond laser is a titanium-doped sapphire crystal, pumped with a single frequency green laser, with the power of 5.5 W. The cavity of our laser has a design as shown in Fig. 3.2. The Ti:Sapphire crystal generates a pulse train with pulse widths as short as 40 fs. The output pulse spectrum is a frequency comb, centered at 820 nm with a width of 20 nm. The output repetition frequency f_r equals to approximately 1 GHz. The CEO frequency f_0 is around 180 MHz. The mirrors inside the cavity are specially coated chirped mirrors, in order to compensate the group velocity dispersion.

In order to obtain a stable output frequency comb, both f_r and f_0 have to be stabilized. The stabilization of both f_r and f_0 is achieved because one of the high-reflector mirror is mounted on a piezoelectric transducer tube that allows both tilt and translation. Measurement of f_r can be achieved by simply detecting the pulse train's repetition rate with a fast photodiode. By comparing a high harmonic of the pulse repetition rate with the output of a high-stability radio frequency synthesizer, a feedback loop can lock the repetition rate f_r by translating the mirror. The measurement of f_0 is more complicated and requires an interferometric measurement. The ultrashort pulses are first sent through a special nonlinear dispersive optical fiber to broaden the spectrum of the mode-locked laser into an octave. Inside the fiber, nonlinear processes including self-phase

modulation and group velocity dispersion take place. The offset frequency is obtained by taking the difference between $2f_n$ and f_{2n}. This is done by shining the output of the nonlinear optical fiber onto a nonlinear crystal and combing the doubled signal with f_{2n} on a photo detector. The resulting RF heterodyne beat is $2f_n - f_{2n} = 2(nf_r + f_0) - (2nf_r + f_0) = f_0$, which is just the offset frequency. Because the pulse spectrum is spatially dispersed across the high reflector mirror, tilting of this mirror provides a linear phase change with frequency, thereby controlling the CEO frequency f_0. The experimental setup for locking the carrier-envelope offset is shown in Fig. 3.3.

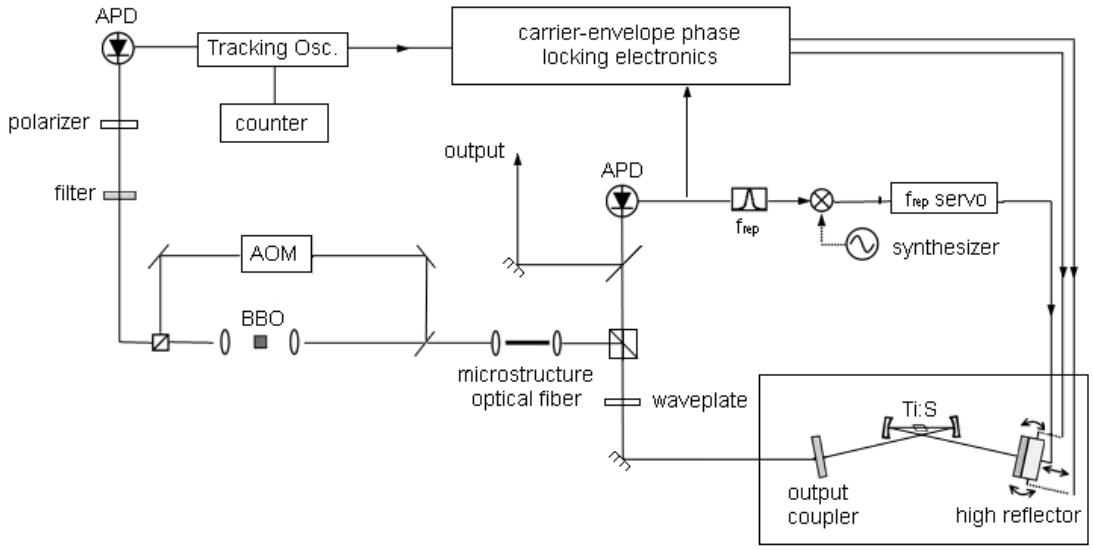

Figure 3.3: Experimental setup for locking the carrier-envelope relative phase. The femtosecond laser is located inside the shaded box. The high-reflector mirror is mounted on a transducer to provide both tilt and translation.

3.3 Femtosecond pulse propagation

3.3.1 Group velocity dispersion

The expression in Eq. 3.1 is only correct for a non-chirped pulse. When a pulse propagates in a dispersive medium, the low frequencies will move faster (or slower) than the high frequencies. The pulse will therefore be broadened and chirped. This effect is called group velocity dispersion [32, 46]. In this section, we will explain this effect for a Gaussian shapes pulse. In the time domain, a normalized nonchirped Gaussian shaped pulse can be written as,

$$E_{in}(t) = e^{-(t/2\tau_{HW})^2} e^{-i\omega_c t + \phi_0} \tag{3.4}$$

where, τ_{HW} is the half width at $1/e$ maximum of the pulse envelope, ω_c is the carrier frequency and ϕ_0 is the initial phase. In the frequency domain,

$$\hat{E}_{in}(\omega) = e^{-(\omega-\omega_c)^2/2\sigma^2} \tag{3.5}$$

where, σ is the spectrum width with $\sigma = 1/\tau$. After propagating a distance L in a homogeneous medium, the electric field is

$$\hat{E}_{out}(\omega) = \hat{E}_{in}(\omega) e^{-\alpha(\omega)L} e^{-ik(\omega)L} \tag{3.6}$$

where, $\alpha(\omega)$ is the absorption coefficient at angular frequency ω and $k(\omega)$ is the wave number. We can expand the k vector into its Taylor series around the central frequency,

$$k(\omega) = k^{(0)}(\omega_c) + k^{(1)}(\omega_c)(\omega-\omega_c) + \frac{1}{2!}k^{(2)}(\omega_c)(\omega-\omega_c)^2 + \frac{1}{3!}k^{(3)}(\omega_c)(\omega-\omega_c)^3 + \cdots \tag{3.7}$$

where

$$k^{(1)}(\omega_c) = \frac{dk}{d\omega}|_{\omega_c} \quad k^{(2)}(\omega_c) = \frac{d^2k}{d\omega^2}|_{\omega_c} \quad k^{(3)}(\omega_c) = \frac{d^3k}{d\omega^3}|_{\omega_c} \tag{3.8}$$

The zero-th item is the propagation of the carrier frequency,

$$k^{(0)}(\omega_c) = n(\omega_c)\cdot\omega_c/c \tag{3.9}$$

where the phase velocity of the carrier frequency is,

$$v_p = \omega_c/k^{(0)}(\omega_c) = c/n(\omega_c) \tag{3.10}$$

Now let us see the effect of the term that depends linearly on the frequency, *i.e* the term $k^{(1)}(\omega)(\omega-\omega_c)$. By substituting $k(\omega) = k^{(0)}(\omega_c) + k^{(1)}(\omega_c)(\omega-\omega_c)$ into Eq. 3.6. We obtain,

$$\hat{E}_{out} = e^{-(\omega-\omega_c)^2/2\sigma^2} e^{-i[k^{(0)}+k^{(1)}(\omega-\omega_c)]L} \tag{3.11}$$

and the inverse Fourier transform of Eq. 3.11 is,

$$E_{out} = e^{\left(t-k^{(1)}L\right)^2/2\tau_{HW}^2} e^{-i\omega_c\left(t-k^{(0)}L\right)} \tag{3.12}$$

Let $v_g = 1/k^{(1)}(\omega_c)$, then Eq. 3.12 becomes,

$$E_{out} = e^{\left(t-\frac{L}{v_g}\right)^2/2\tau_{HW}^2} e^{-i\omega_c\left(t-\frac{L}{v_p}\right)} \tag{3.13}$$

It is clear that the envelope and the carrier phase propagate with different speeds, when L is equal to one cavity length L_{pp}, the difference, $L_{pp}/v_g - L_{pp}/v_p$ is called carrier-envelope offset, which has been discussed in last section.

Now we consider also the term in Eq. 3.7 that depends quadratically on $\omega-\omega_c$. If we substitute $k(\omega) = k^{(0)}(\omega_c) + k^{(1)}(\omega_c)(\omega-\omega_c) + \frac{1}{2!}k^{(2)}(\omega_c)(\omega-\omega_c)^2$ into Eq. 3.6, we get,

$$\hat{E}_{out} = e^{(\omega-\omega_c)^2/2\sigma^2} e^{-i[k^{(0)}+k^{(1)}(\omega-\omega_c)+k^{(2)}(\omega_c)(\omega-\omega_c)^2/2]L} \tag{3.14}$$

Please notice that Eq. 3.14 is a complex Gaussian function and that its inverse Fourier transform is,

$$E_{out} = e^{\frac{1}{4}\frac{\alpha}{\alpha^2+\beta^2}\left(t-\frac{L}{v_g}\right)^2} e^{-\frac{1}{4}\frac{\beta i}{\alpha^2+\beta^2}\left(t-\frac{L}{v_g}\right)^2} e^{-i\omega_c\left(t-\frac{L}{v_p}\right)} \tag{3.15}$$

where

$$\alpha = -\frac{1}{4}\tau_{HW}^2 \quad \beta = \frac{1}{2}\frac{d^2}{d\omega^2}k(\omega)|_{\omega_c}L \tag{3.16}$$

The first factor at the right of Eq. 3.15 is the broadened Gaussian amplitude and the third factor is the carrier wave. The second factor is called the phase chirp because different frequencies propagate at different speeds. For this reason the quadratic term in Eq. 3.7 is also called group velocity dispersion(GVD). The GVD determines the width of the output pulses. Inside the Ti:Sapphire cavity, the GVD introduced by air must be compensated by the special chirped high reflection mirrors.

$k^{(1)}(\omega_c)$	Envelope width is unchanged. Carrier-Envelope offset appears $L/v_p - L/v_g$. Maximum fringe propagates at v_g.
$k^{(2)}(\omega_c)$	Envelope width is broadened. Carrier phase is linear chirped. Maximum fringe propagates at v_g.
$k^{(3)}(\omega_c)$	Envelope shape is changed. Carrier phase is nonlinear chirped. Maximum fringe propagates NOT at v_g.

Table 3.1: Comparison of the first, second and third orders of the expansion of the k vector in a dispersive medium.

For the higher orders of $k(\omega)$, we presently do not have an analytic solution. But from simulations it can shown that the envelope function will change from a Gaussian to much complicated form. At the same time, the carrier is nonlinearly chirped and the definition of the group velocity of the envelope does not work [47]. The peak of the pulse intensity does not propagate with the group velocity defined as $v_g = \frac{dk}{d\omega}(\omega_c)$. In Table.3.1 we give a summary of the effect of the first three orders in Eq. 3.7. Let us give an example by considering a well-known dispersive medium: air. At a center wavelength of 800 nm, $k^{(0)} = 7.86 \times 10^6$, $k^{(1)} = 3.34 \times 10^{-9}$, $k^{(2)} = 2.13 \times 10^{-29}$ and $k^{(3)} = 1 \times 10^{-44}$. Now we simulate a Gaussian spectrum, centered at 3.7474×10^{14} Hz (800 nm) with a bandwidth (Full width half maximum) of 1×10^{14} Hz (217 nm) as shown in Fig. 3.4-(a). The pulse shape is also taken to be a Gaussian function with the pulse width of around 10 fs, as shown in Fig. 3.4-(b). In Fig. 3.5-(a),(b),(c) shows this pulse propagating 1 m in air (calculated by using the group refractive index of 800 nm at 1 atm $n_g = 1.000279955$) by considering the first, second and third order expansion of the wavenumber k respectively. The refractive index of air is calcualted by the updated Edlén's Equation [39].

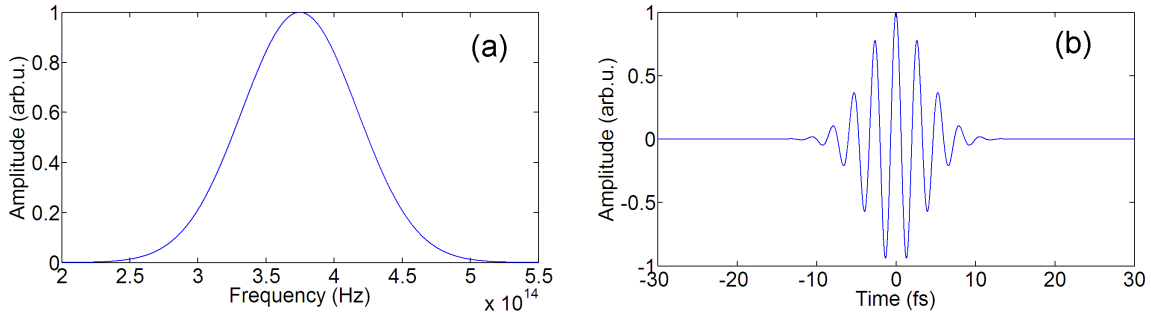

Figure 3.4: (a) Simulated Gaussian shaped spectral amplitude, centered at 3.7474×10^{14} Hz (800 nm) with a bandwidth (Full width half maximum) of 1×10^{14} Hz (217 nm). (b) The Gaussian shape pulse corresponding to the spectrum shown in (a)

In this section we used the slowly varying envelope approximation, originally introduced by Born and Wolf [32]. The temporal field behavior is separated into the product of a slowly varying envelope function and an exponential phase term, whose angular frequency is centered about some characteristic frequency ω_c of the pulse. Hong Xiao and Kurt E. Oughstun showed that, for pulses less than 10 fs, this approximation is not valid [48, 49]. A more complicated asymptotic description has to be used.

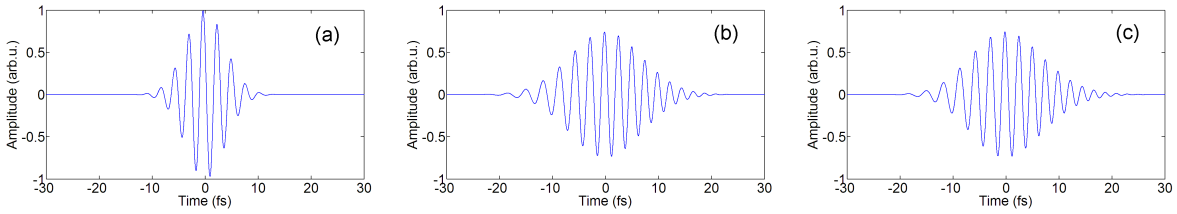

Figure 3.5: Group delay dispersion of a 10 fs pulse propagation in air. The original pulse is Gaussian shaped shown in Fig. 3.4-(b). (a) The pulse after propagating 1 m in air by considering the first order expansion of the k vector only. (b) The pulse after propagating 1 m in air by considering the first and second order expansion of the k vector. (c) The pulse after propagating 1 m in air by considering the first, second and third order expansion of the k vector.

3.3.2 Self-phase modulation

The self-phase modulation (SPM) is another effect when strong pulses pass through a dispersive medium, for example a fiber. The pulse will induce a varying refractive index of the medium due to the optical Kerr effect.

$$n(I) = n_0 + n_2 \cdot I \tag{3.17}$$

Here, I is the pulse intensity. n_0 is the linear refractive index and n_2 is the second order nonlinear refractive index of the medium. This variation of refractive index will produce a phase shift in the pulse, leading to a change of the pulse's frequency spectrum. For the work performed as a part of this thesis, the pulses mainly propagate in air where SPM can be ignored.

3.4 Femtosecond pulse characterization

3.4.1 Field autocorrelation

The ultrashort pulse measurements can be mainly categorized as either test-pulse-referencing or as self-referencing. Test-pulse-referencing measurement means the unknown pulse is characterized against a well-known reference pulse, normally by building an interferometer. In the self-referencing measurement the reference pulse is a spectrally or temporally shifted replica of the pulse itself. In this section, we only consider the self-referencing measurements.

The most simple pulse measurement technique is the Fourier transform spectrometer. This setup is directly derived from a Michelson interferometer, except one arm is periodically displaced. In this case, the electric field transmitted through the device is a sequence of two pulses. The signal recorded as function of the time delay τ between the two arms and is well known to be the first-order autocorrelation of the incident electric field,

$$I(\tau) = \Re \int_{-\infty}^{\infty} E(t)E^*(t-\tau)dt \tag{3.18}$$

This quantity is also called the field autocorrelation or the field interferogram. In Fig. 3.6 the schematic of the experimental setup of the Fourier transform spectrometer and the field autocorrelation are shown. The field autocorrelation is simulated from a 10 fs Gaussian shaped pulse as shown in Fig. 3.4-(b). The x-axis is the separation between the two interfering pulses, which is equivalent to twice the displacement of the reference arm. To measure a pulse, it is sufficient to measure its

intensity and phase in either the time or frequency domains. Unfortunately, the field autocorrelation gives no information on the spectral phase. The Fourier transform of the field autocorrelation is simply the power spectral density (PSD), a result known as the Wiener-Khinchin theorem. Besides the power spectral density, the field autocorrelation does not give us more information. The number of ambiguities associated with the measurement of only the pulse spectrum is downright humorous because we lack all knowledge of the spectral phase. This class of problems is called the one-dimensional phase-retrieval problem and it is unsolvable. The Fourier transform spectrometer is a linear measurement technique. Here, 'linear' refers to measurements with linear optics and slow detectors, such as photo diodes, photo diode arrays, and CCD panels. Measurements are also possible with "'non-linear optics"' such as second harmonic generation. The linear techniques, especially the test-pulse-referencing linear techniques, play an important role in this thesis and we will consider it in more detail it in Chapter 4.

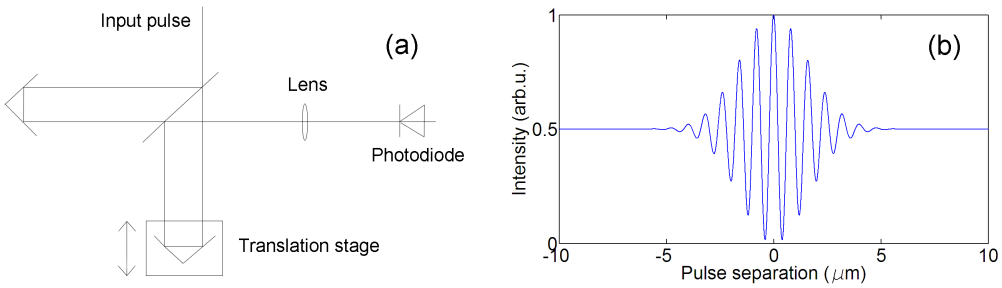

Figure 3.6: (a) Schematic of the experimental setup for measuring the field autocorrelation (b) A typical field autocorrelation.

3.4.2 Intensity autocorrelation

If the reflected beams from both arms of the Fourier transform spectrometer are spatially overlapped into a nonlinear-optical medium, such as a second-harmonic generation crystal, the generated second harmonic field has intensity proportional to the product of the intensities of the two input pulses,

$$A(\tau) = \int_{-\infty}^{\infty} I(t)I(t-\tau)dt \tag{3.19}$$

The quantity is called the second-order autocorrelation or the intensity autocorrelation, or sometimes the background free autocorrelation [50]. The intensity correlation and a schematic of a typical measurement setup is shown in Fig. 3.7. It is clear that an intensity autocorrelation yields some measurement of the pulse length, for example, the RMS (root mean square) length of the pulse will be the square root of two times the width of the intensity autocorrelation. But generally, if we need both the intensity and the phase, either in time or frequency domain, we need at least two independent measurements: The intensity autocorrelation is only one measurement. This is another one-dimensional phase retrieval problem and ambiguities always remains. To obtain the full width half maximum of the pulse, a guess must be made as to the pulse shape. For example, a Gaussian intensity yields an intensity autocorrelation that is $\sqrt{2} = 1.41$ times wider.

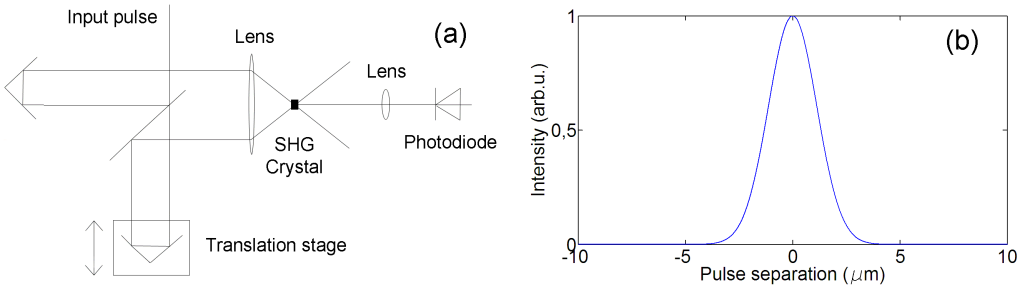

Figure 3.7: (a) Schematic of the experimental setup for measuring the intensity autocorrelation (b) A typical intensity autocorrelation.

3.4.3 Fringe resolved autocorrelation

In Fig. 3.7, the reflected beams from the two arms of the interferometer are not co-linear. If the autocorrelation is measured with collinear beams, then, combined quantities related to the intensity autocorrelation and the field autocorrelation are measured in a single data trace, as shown in Fig. 3.8. This kind of autocorrelation is called the interferometric autocorrelation or fringe-resolved autocorrelation (FRAC), or sometimes phase-sensitive autocorrelation [51].

$$I_{FRAC}(\tau) = \int_{-\infty}^{\infty} \left| [E(t) - E(t-\tau)]^2 \right|^2 dt \tag{3.20}$$
$$= \int_{-\infty}^{\infty} \left[I(t)^2 + I(t-\tau)^2 \right] dt - 2\int_{-\infty}^{\infty} [I(t) + I(t-\tau)]\, \Re\left[E(t)E^*(t-\tau) \right] dt$$
$$+ \int_{-\infty}^{\infty} \Re\left[E(t)^2 E^*(t-\tau)^2 \right] dt + 4\int_{-\infty}^{\infty} I(t)I(t-\tau)dt$$

The FRAC contains four items: a constant which is the intensity of both pulses; the "modified interferogram" with an additional factor, $I(t) + I(t-\tau)$; the interferogram of the pulse second harmonic and the intensity autocorrelation;. The FRAC is always symmetrical and the ideal peak-to-background ratio in a FRAC trace is 8. Similarly as the background free autocorrelation, the FRAC itself is not enough to characterize a pulse because it is again a one-dimensional phase retrieval problem. Also, there is no direct links between the pulse width and the width of the interferometic autocorrelation in general.

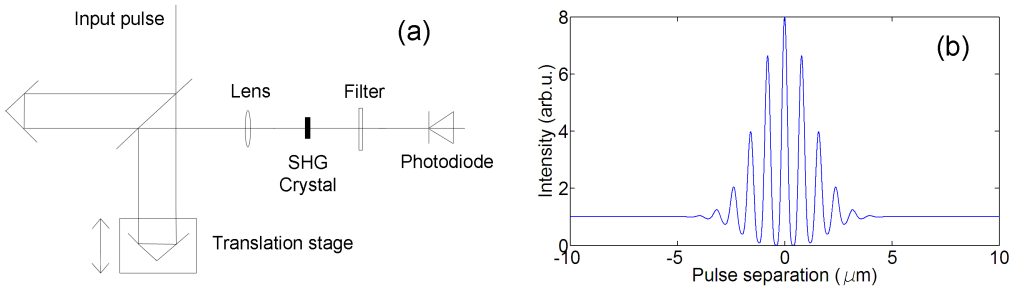

Figure 3.8: (a) Schematic of the experimental setup for measuring the interferometric autocorrelation (b) A typical interferometric autocorrelation.

3.4.4 SPIDER

As square law detectors are not sensitive to the phase, the measurement of the intensity (whether it is spatial or spectral) is an easy task but the measurement of the phase needs indirect solutions. SPIDER (spectral phase interferometry for direct electric-field reconstruction) is a technique which characterizes the spectral phase of ultrashort optical pulses, based on shearing interferometry in the optical frequency domain [52, 53]. The SPIDER only gives you the spectral phase. To characterize a pulse, the power spectral density (PSD) need to be measured independently.

3.4.5 FROG

In the most common configuration, FROG (Frequency-resolved optical gating) is simply a background-free autocorrelator followed by a spectrometer [54, 55]. The two-dimensional nature of the FROG trace allows the extraction of the uniquely determined waveform intensity and phase. Compared to SPIDER, the FROG technique measures a two-dimensional representation of the one-dimensional field and consequently requires the collection of a relatively large amount of data. The algorithm needed to invert the data and reconstruct the field is thereby more sophisticated. The advantage of FROG is of practical nature as it does not require a new apparatus since in most cases an autocorrelator and spectrometer are readily available in general optical laboratories.

3.5 Using the femtosecond frequency comb for distance interferometry

In the recent past, there have been many proposals to implement the femtosecond frequency comb laser source for distance measurement. In 2004, Ye published the first scheme to measure an absolute distance using this laser [17]. Similar schemes were also proposed by other groups. This method relies not only on the stability of the pulse repetition frequency, but also on the stability of the optical phase with respect to the pulse train. The idea is simply to use the frequency comb laser as the source for a Michelson interferometer. If the path length difference of the two arms of the interferometer is an integer multiple of the cavity length of the laser, the local and the delayed pulse will interfere and form a so called cross-correlation trace. In theory, this would allow determining a distance to within one optical fringe over distances as large as the coherence length of the laser.

Another scheme for using the femtosecond frequency comb laser as a tool of distance measurement based on white light interferometers was proposed in 2006 by Joo and coworkers [56, 57]. The inspiration comes from the white light channeled interferometrical techniques. Instead of the cross correlation functions, the beams from both arms of the interferometer combined onto a spectral interferometer. The modulated spectrum are recorded and path-length difference between the two arms is obtained by using Eq. 2.24.

A scheme based on multiple wavelength interferometry using the frequency comb laser was published in 2008 by Salvade and colleagues [58]. His group selected two individual frequencies from the comb in order to accurately lock two independent continuous lasers, forming the source of a two wavelength interferometer. The continuous lasers are necessary because the energy of each frequency line of the femtosecond laser is very weak. For a typical output power of a Ti:Sapphire laser of 1 W, there are 10^5 individual frequencies and each of these has only a power of around 10 μW.

In 2009, S.Hyun and co-authors published a fourth technique based on frequency sweeping using

the frequency comb [59]. They used a tunable laser to make a frequency sweeping interferometer. Instead of the Fabry-Perot cavity, they locked the output frequencies of the tunable laser to the repetition frequencies of a femtosecond laser. Then the sweeping range can be accurately known by counting the modes of the repetition frequencies of the femtosecond laser.

Another distance measurement using frequency comb has been reported in 2009 by Coddington and coworkers [60]. This work used two frequency comb lasers and was based on the laser radar (LIDAR) principle. Distances were measured by pulse propagation in 1.14 km of fiber. The authors report that their data mimic those needed to make remote measurements of the pointing of a satellite, or the angle of a machined surface.

Most of these publications were proposals or measurements of distances less than 1 m or in fiber [61, 62]. Very few experiments had been done for long distances in air [63]. During this thesis, we will give the first experimental demonstration for a measurement of distances by free propagation of upto 50 m in air.

Chapter 4

Linear Technology of ultrashort pulse detection

4.1 General introduction to linear measurement techniques

In this chapter, linear techniques for short pulse characterization is discussed [64]. The conclusions in this chapter will be very important in understanding the experiments in Chapter 5 and 6. Figure.4.1 is a schematic for a general setup for linear experiments. The incident beam is sent into a linear device, which is characterized by its response function, $R(t)$ in the time domain or $\hat{R}(\omega)$ in the frequency domain. The transmitted pulses are then sent into a time-integrating detector. Let us call $E(t)$ the electric field of the incident light beam and $\hat{E}(\omega)$ its Fourier transform.

$$\hat{E}(\omega) = \int_{-\infty}^{\infty} E(t) e^{-i\omega t} dt \tag{4.1}$$

and

$$E(t) = \int_{-\infty}^{\infty} \hat{E}(\omega) e^{-i\omega t} d\omega \tag{4.2}$$

Here the factor $1/2\pi$ before the integral has been ignored. The electric field transmitted through the linear device is,

$$E^{'}(t) = \int E(t^{'}) R(t - t^{'}) dt^{'} \tag{4.3}$$

or

$$\hat{E}^{'}(\omega) = \hat{E}(\omega)\hat{R}(\omega) \tag{4.4}$$

Here, $E^{'}(t)$ and $\hat{E}^{'}(\omega)$ is the electric field of the transmitted pulses in the time and frequency domain. From the assumption of time-integrated detection, it follows that the detected signal is simply the pulse energy, which is also the frequency-integrated power spectrum,

$$I = \int |E^{'}(t)|^2 dt = \int |\hat{E}^{'}(\omega)|^2 d\omega \tag{4.5}$$

A good example of linear measurement is the dispersive spectrometer. The dispersive spectrometer simply measures the spectrum by using a prism or a grating and a line CCD. The Fourier transform spectrometer introduced in chapter 3 is another example of a linear device. In both spectrometers, only the power spectrum density (PSD) is measured. The spectral phase is lost. To see this, consider an example of how the spectral phase determines a pulse shape. Let us use the symmetric Gaussian shape PSD introduced in Chapter 3 section 3.1. The center of the PSD is 3.7474×10^{14} Hz (800 nm).

Figure 4.1: General Linear measurement setup

The width (Full width half maximum) of the PSD is 0.7×10^{14} Hz. The repetition frequency is 30 GHz, corresponding to 1 cm inter-pulse distance in vacuum. The offset frequency, f_0 is ignored because it only gives a constant phase shift, as will be shown in chapter 4 section 3.1. The PSD is plotted with respect to f in Fig. 4.2-(a) and the autocorrelation is plotted in Fig. 4.2-(b). The autocorrelation and the PSD are related by the Wiener-Khinchin theorem. Figure.4.3-(a) shows the corresponding Gaussian shape pulse of the PSD in Fig. 4.2. We observe that Gaussian PSD does not guarantee a Gaussian pulse shape, because the pulse shape is also determined by the spectral phase. For example, after 2 m propagation in air, the pulse shape changes to Fig. 4.3-(b), but the PSD does not change if the absorption of air is ignored. Similarly, Fig. 4.3-(c) shows the pulse shape after 1 cm propagation in BK7. Although the pulse shape can change dramatically due to dispersion, if there is no absorption and the PSD remains unaltered, the autocorrelation also remains the same, as shown as in Fig. 4.3-(b).

Although the linear devices are never sufficient to fully characterize a pulse, but this does not mean

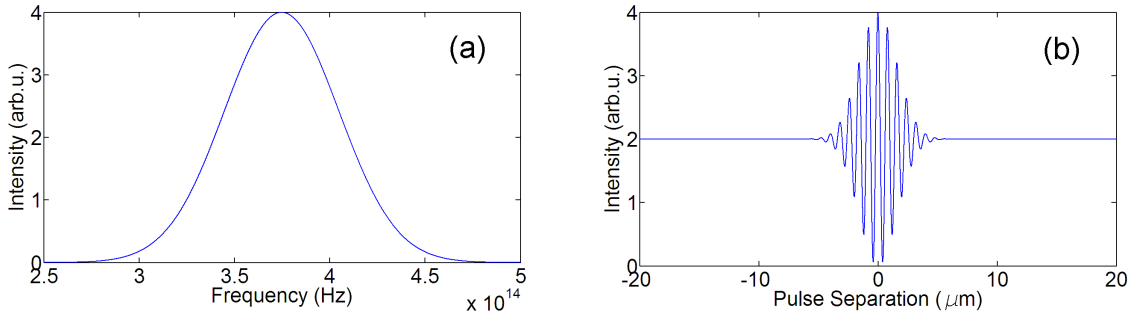

Figure 4.2: (a) A symmetric Gaussian shaped PSD (b) The corresponding autocorrelation function

that linear techniques are not useful for femtosecond pulse applications. Consider an interferometer with incident beam $2E(t)$, we divide this into two beams and then recombine the two light beams associated with two different electric fields, $E_r(t)$ and $E_m(t)$, corresponding to the reference and measurement arm respectively. Ignoring the absorption, we have,

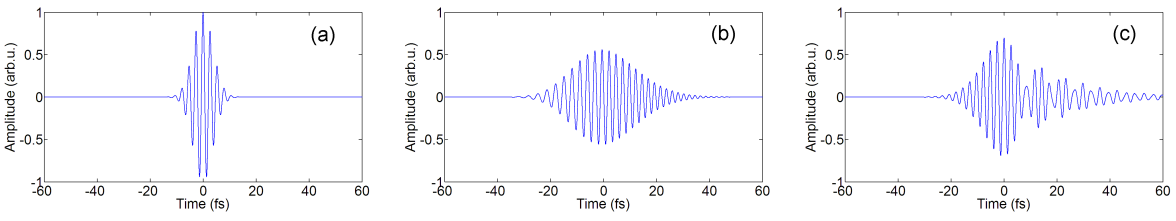

Figure 4.3: Three different pulse shapes corresponding to the autocorrelation shown in Fig. 4.2-(b). (a) Gaussian shaped pulse (b) Pulse from Fig. 4.3-(a) after 2 m propagation in air (c) Pulse from Fig.4.3-(a) after 1 cm propagation in BK7.

$$\hat{E}_r(\omega) = |\hat{E}(\omega)|e^{i(\varphi_0+\varphi_r)} \tag{4.6}$$

and

$$\hat{E}_m(\omega) = |\hat{E}(\omega)|e^{i(\varphi_0+\varphi_m)} \tag{4.7}$$

A time-integrating detector will be sensitive to only the power spectrum of the sum of the two electric fields,

$$S(\omega) = |\hat{E}_r(\omega) + \hat{E}_m(\omega)|^2 \tag{4.8}$$

which includes a crossed term $\hat{E}_r^*(\omega)\hat{E}_m(\omega)$. Therefore the signal will be sensitive to the phase difference, $\varphi_r(\omega) - \varphi_m(\omega)$. If $\hat{E}_r$ and $\hat{E}_m$ were derived from an incident pulse through linear devices, the phase of the incident pulse would appear as an additive factor in both φ_r and φ_m, so that it would cancel out and only the difference between the two arms is left.

Another unique advantage of linear interferometry is sensitivity. If we were to use a standard nonlinear technique, the detected signal would be proportional to E^4 for second-order techniques. In contrast, linear interferometry yields a signal proportional to E^2.

4.2 First order cross correlations: linear detection in time

One example of linear measurement device is the unbalanced Fourier transform spectrometer, as shown in Fig. 4.4, with the sample located inside one of the arms. This "sample" could be any linear phase object, such as a piece of glass, mirrors or in general some cause of a path-length differences. The imprint of the sample will be seen on the cross correlation function. Let us use the PSD of Fig. 4.2 and show how the cross correlation function changes due to the difference between the two arms. Figure. 4.5-(a) is the autocorrelation, which is uniquely determined by the PSD. We would like to refer to the three different pulse shapes in Fig. 4.3. Figure. 4.5-(b) shows the cross correlation function between Fig. 4.3-(a) and Fig. 4.3-(b), where one pulse is unchirped, and the other has propagated 2 m in air. The cross correlations between Fig. 4.3-(a) and Fig. 4.3-(c) is given in Fig. 4.5-(c). This time, the "sample" is 1 cm of BK7. The respective dispersion relations have been explained earlier in chapter 2.

4.2.1 Mathematical analysis of the cross correlation

In this section, we study how to use the unbalanced Fourier transform interferometer for distance measurement. We take each comb frequency into account, and give a mathematical relation between cross correlations and the path length difference in air. In an unbalanced Michelson interferomter, only when the path length difference between the two arms is very close to a multiple of the inter-pulse distance can we see a correlation. Hence for non-zero correlations we should have, in good approximation,

$$l_m = l_r + m \cdot l_{pp/2}, \tag{4.9}$$

where, l_m and l_r represent the distances of the long measurement arm and the short reference arm respectively. Here m is a non-negative integer number. In this thesis, the inter-pulse distance, or the cavity length, is denoted to L_{pp}, and we use another symbole $l_{pp/2}$ to denote the half of the inter-pulse distance, or equivalently, half cavity length. The inter-pulse distance is in a dispersive medium a somewhat arbitrary notion. We explicitly define it by,

$$L_{pp} = c/(n_g \cdot f_r), \tag{4.10}$$

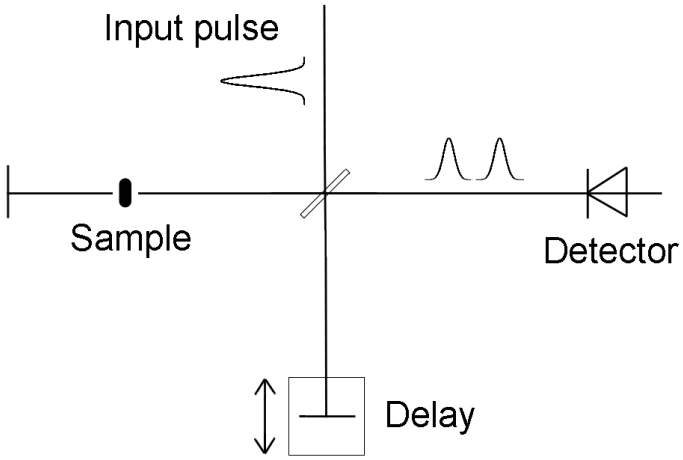

Figure 4.4: Schematic of the experimental setup of an unbalanced Fourier transform spectrometer

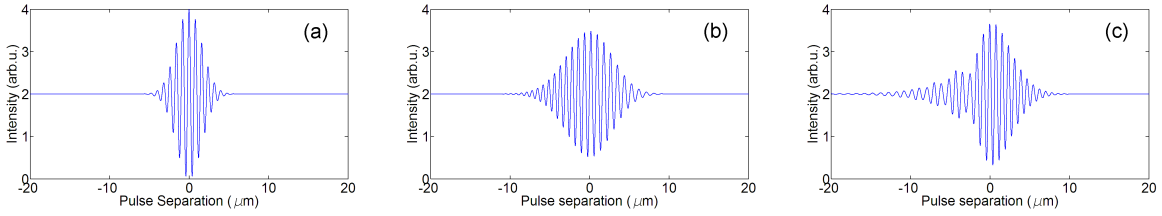

Figure 4.5: Crosscorrelations arising from the pulses shown in Fig. 4.3. (a) The autocorrelation of pulse shown in Fig.4.3-(a). (b) The cross correlation function between the pulses shown in Fig. 4.3-(a) and Fig. 4.3-(b), where one pulse is unchirped, and the other has propagated 2 m in air. (c) The cross correlations between the pulses shown in Fig. 4.3-(a) and Fig. 4.3-(c), where one pulse is unchirped, and the other has propagated 1 cm in BK7.

where n_g is the group refractive index at the central wavelength of the spectrum and f_r is the repetition frequency. Here, the "center wavelength" is obviously defined as the wavelength at which the Gaussian PSD is maximum, but this definition is only valid for a spectrum which is symmetric.

For the most simple case where the two pulse trains after the beam splitter are equal and can be written as:

$$\Re E(t) = \Re\left\{\sum_{n=1}^{N} |E_n| e^{i\phi_n} e^{i\omega_n t}\right\} \tag{4.11}$$

where $\hat{E}_n$ is the spectral amplitude and ϕ_n is the spectral phase. $ReE(t)$ means the real part of $E(t)$ and the angular frequencies of the comb are represented by,

$$\omega_n = \omega_0 + n\omega_r, \tag{4.12}$$

where ω_0 is the offset angular frequency. If the refractive index in both arms are equal, after propagating two different arms in air, whose length are labeled as l_r and l_m respectively, we have

$$\begin{aligned} \Re E_r(t, l_r) &= \Re\left\{\sum_{n=1}^{N} |E_n| e^{i\phi_n} e^{i(\omega_n t - 2k_n l_r)}\right\} \\ \Re E_m(t, l_m) &= \Re\left\{\sum_{n=1}^{N} |E_n| e^{i\phi_n} e^{i(\omega_n t - 2k_n l_m)}\right\}. \end{aligned} \tag{4.13}$$

Here k_n is a real function of ω_n, determined by the Edlï£¡n's equation [35]. The absorption of the air has been ignored.

The instantaneous intensity for the field cross correlation is,

$$I_\omega(t, l_r, l_m) = (\Re E_r + \Re E_m)^2 \tag{4.14}$$

The intensity that is measured by a slow detector, after time averaging, is equal to,

$$\langle I_\omega(t, l_r, l_m)\rangle = \left\langle (E_r + E_m)(E_r + E_m)^* \right\rangle \tag{4.15}$$

By substituting Eq. 4.14 into Eq. 3.17, we get,

$$\langle I(L)\rangle = 2\sum_{n=1}^{N} |E_n|^2 \{1 + \cos[\omega_n n(\omega) L/c]\} \tag{4.16}$$

where $L = 2(l_r - l_m)$ is the path length difference. Now, compare Eq. 4.16 to Eq. 3.17, we recognize that the cross correlation function is only the heterodyne signal of all the repetition frequencies, when the fs laser is considered as a multiple wavelength source. We have shown here that, the field cross correlation is determined by the PSD and the path length difference between the two arms.

4.2.2 The cross correlation functions of a symmetric power spectral density

Using the PSD shown in Fig. 4.2-(a), we calculate the cross correlation functions at different path-length differences in air, as shown in Fig. 4.6. We observe that, because of the dispersion, the widths of the cross correlations increase with increasing path length difference. The chirp acquired by the pulse is clearly seen after 10 m propagation. Figure. 4.7-(a) shows the relation between the propagation distance and the widths. It is interesting to see that, even if we start from a Gaussian shape

PSD and a Gaussian shaped pulse, the shape of the cross correlation functions can vary a lot after propagating a long distance. To demonstrate this effect, let us consider R_{HW} to be the half-width on the right of the full-width at half maximum and L_{HW} to be the left half width at the full width at half maximum. We define the chirp ratio as R_{HW}/L_{HW}. In Fig. 4.7-(b), we show the chirp ratio as a function of path length differences.

If we define the "inter-pulse distance" by Eq. 4.10, then, the position of the maximum of the cross

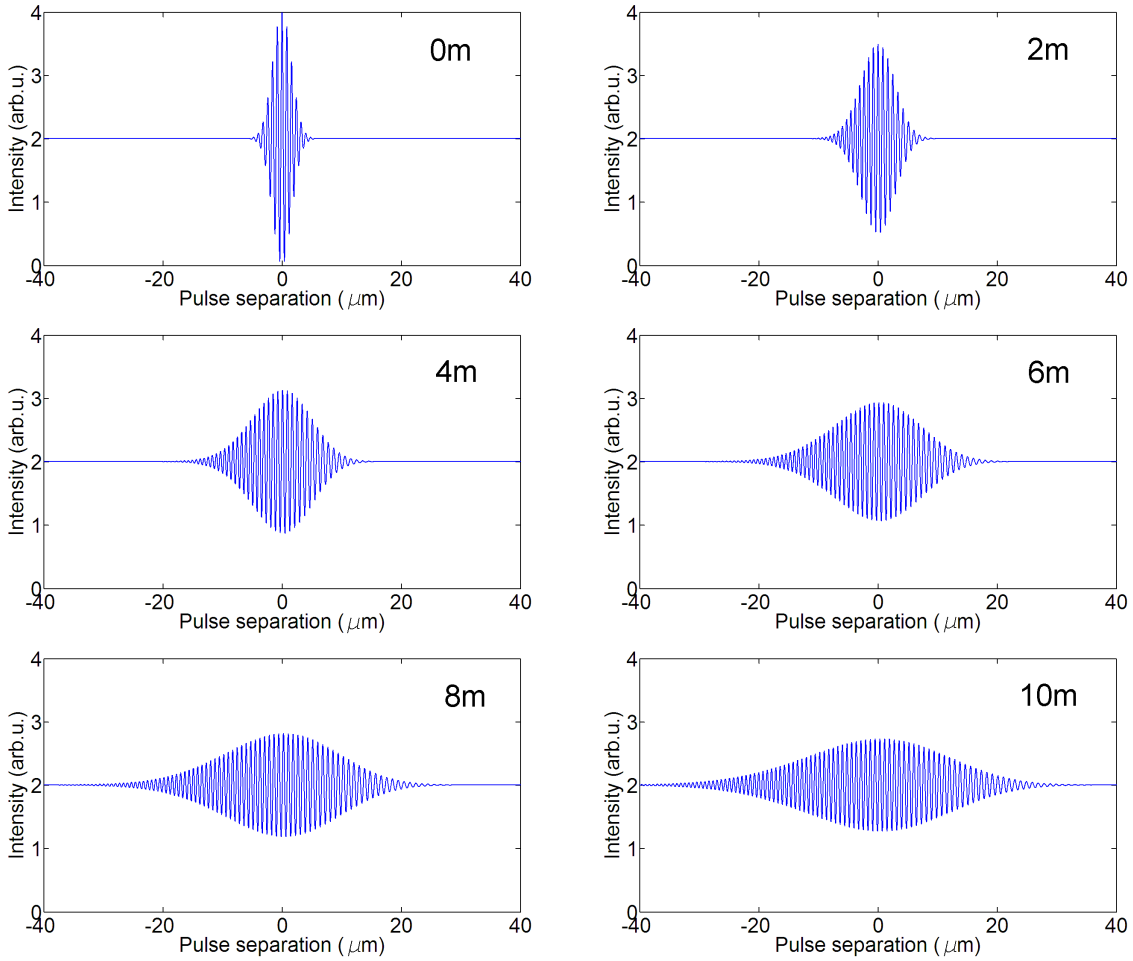

Figure 4.6: Simulated cross correlations of a pulse propagating in air, in an unbalanced Michelson interferometer. We have used the symmetric power spectral density for the pulse. The path length difference are indicated with each cross correlation.

correlation function does not overlap with the distance of a multiple of cavity length. The difference is caused by the nonlinear property of the refractive index of air, as introduced in Chapter.3.3.1. This difference is very small, and is plotted in Fig. 4.8. as the function of the path length difference. This has consequences when we extract the distance from cross correlation functions. We will discuss this further in the following chapters.

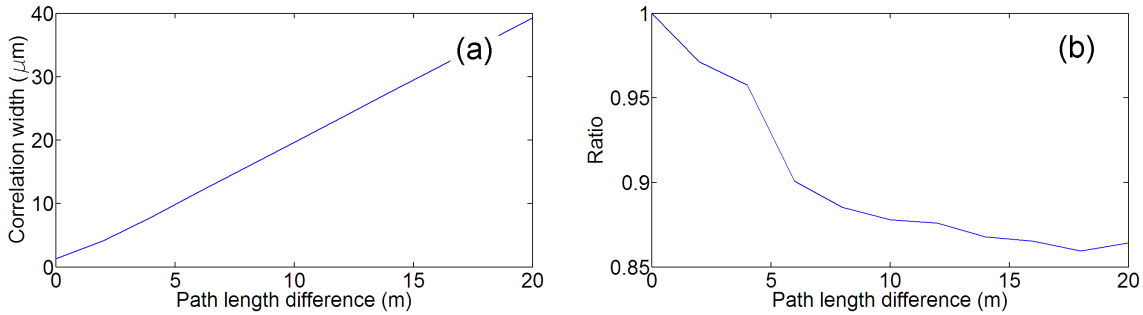

Figure 4.7: The relation between the path length difference and the properties of the cross correlation for a pulse having a symmetric PSD. (a) The widths of the cross correlations as a function of the path length difference. (b) The chirp ratio of the cross correlations as a function of the path length difference.

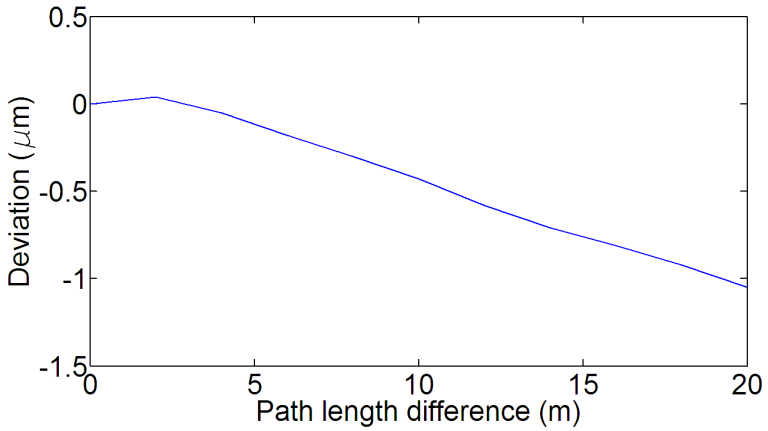

Figure 4.8: The difference between the position of the maximum of the cross correlation function and the multiple of the inter-pulse distance, as a function of the path length difference. Here we have used a pulse having a symmetric PSD.

4.2.3 The cross correlation functions from an asymmetric power spectral density

When the PSD is asymmetric, the situation is more complex. Now, not only the nonlinear behavior of the refractive index, but also the asymmetry of the spectrum influences the shape of the cross correlation function. Let us now simulate an asymmetric spectrum. The center of the PSD is still at 3.7474×10^{14} Hz (800 nm). But this time, the PSD consists two Gaussians. The left side of the Gaussian PSD has a half width at half maximum of 0.52×10^{14} Hz, and the right side of the Gaussian PSD has a half width at half maximum of 0.18×10^{14} Hz. The repetition frequency is again 30 GHz, corresponding to 1 cm inter-pulse distance in vacuum. The PSD is plotted with respect to frequency f in Fig. 4.9-(a) and the autocorrelation is plotted in Fig. 4.9-(b). The autocorrelation and the PSD is related by the Wiener-Khinchin theorem.

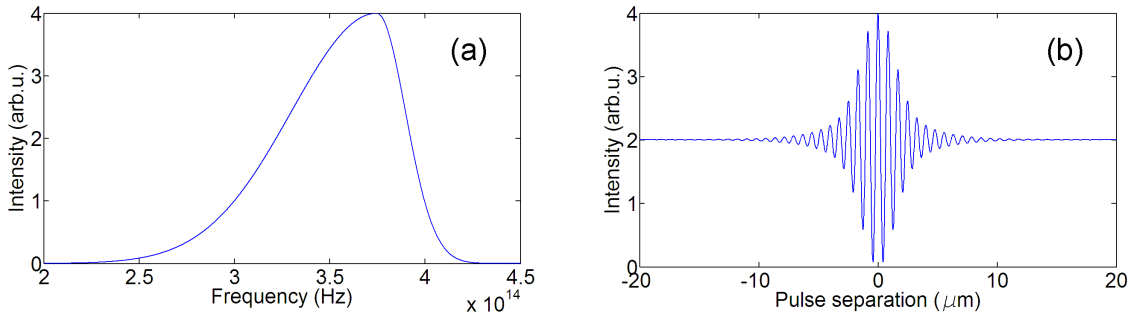

Figure 4.9: (a) A asymmetric Gaussian shaped PSD, described in section 4.2.3. (b) The corresponding autocorrelation function

Figure. 4.10 shows the cross correlation functions at different distances (back and forth). We can also check the width and symmetry of the cross correlation functions and show them in Fig. 4.11. In this case there is no reason that the chirp could change in a single way. The chirp could go to the negative and later change to the positive side.

Now the difference between the position of the maximum of the cross correlation function and a multiple of the inter-pulse distance still exists and is even more than the symmetric case. This is reasonable because now, this difference is due to two reasons: the non-linear property of the refractive index of air and the asymmetry of the power spectral density. This difference is plotted in Fig. 4.12. as the function of path length difference. As mentioned before, this has consequences when we extract the distance from cross correlation functions. We will discuss this further in the following chapters.

4.3 Spectral interferogram: linear detection in frequency

The Fourier transform spectrometer is not the only way to measure the correct PSD. Another commonly used linear measurement technique in determining the spectrum is a grating spectrometer [65]. Instead of the cross correlation function, we simply measure the spectrum by using a prism or a grating. If a grating spectrometer is used as a detector after a Michelson interferometer, we call this setup a dispersive interferometer. When the Michelson interferometer is unbalanced, an additional interference term appears. In this case, no variation in either arm is needed, but a line camera is required to observe the combined spectrum, as shown in Fig. 4.13. Again, the sample

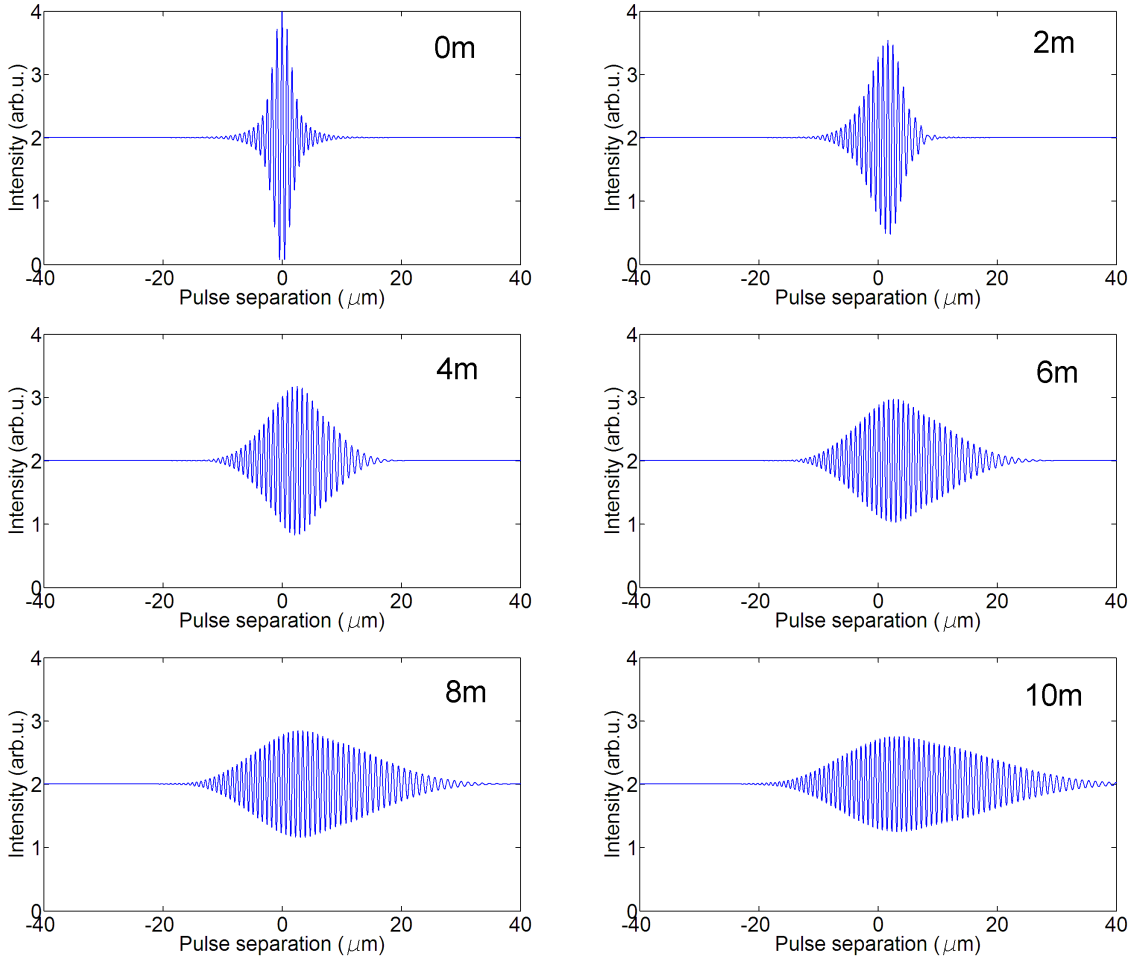

Figure 4.10: Simulated cross correlations of a pulse propagating in air, in an unbalanced Michelson interferometer. We have used the asymmetric power spectral density described in section 4.2.3 for the pulse. The path length difference are indicated with each cross correlation.

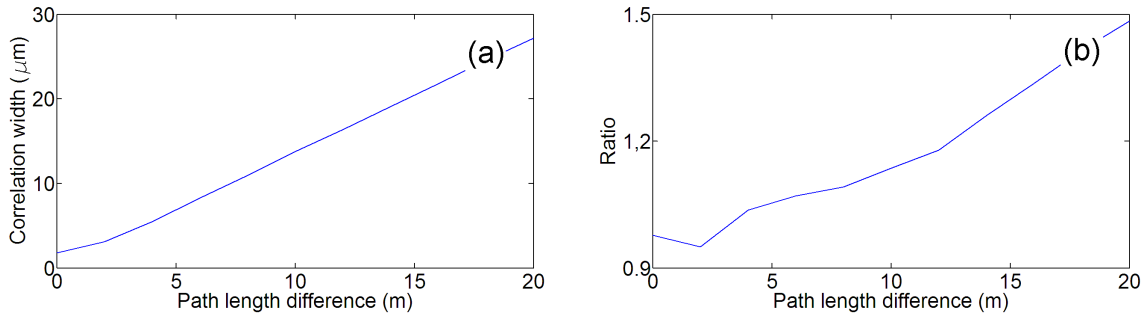

Figure 4.11: The relation between the path length difference and the properties of the cross correlation for a pulse having an asymmetric PSD as discribed in section 4.2.3. (a) The widths of the cross correlations as a function of the path length difference. (b) The chirp ratio of the cross correlations as a function of the path length difference.

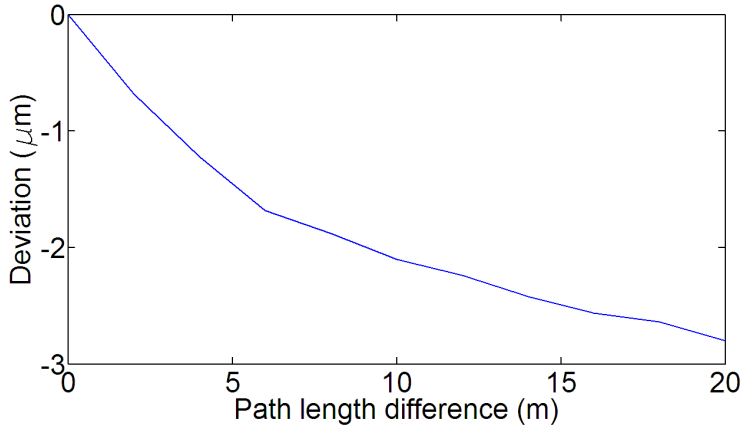

Figure 4.12: The difference between the position of the maximum of the cross correlation function and the multiple of the inter-pulse distance, as a function of the path length difference. Here we have used a pulse having an asymmetric PSD as discribed in section 4.2.3.

could be a path length difference in air, a piece of glass, or other dispersive medium [66]. We neglect absorption in this analysis. In the following chapters, this modulated spectrum is often refered to as a spectral interferogram, or briefly as interferogram.

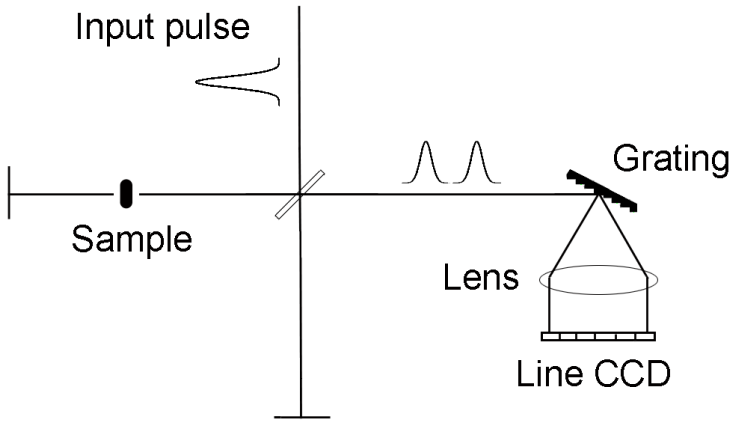

Figure 4.13: Schematic of the experimental setup of an unbalanced grating dispersive interferometer.

If the two arms of the interferometer are equal and there is no sample, what we measure should be the PSD itself, as shown in Fig. 4.14-(a). We would like to refer to the three different pulse shapes in Fig. 4.3. Figure. 4.14-(b) shows the spectral interferogram between Fig. 4.3-(a) and Fig. 4.3-(b), where one pulse is unchirped, and the other has propagated 2 m in air. The spectral interferogram between Fig. 4.3-(a) and Fig. 4.3-(c) is given in Fig. 4.14-(c). The imprint of the sample will be seen on the spectral interferogram.

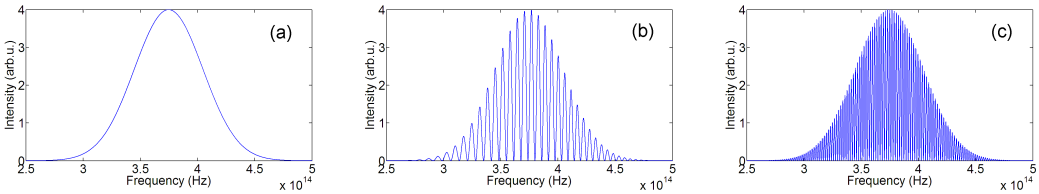

Figure 4.14: Spectral interferograms arising from the pulses shown in Fig. 4.3. (a) The spectral interferogram of the pulse shown in Fig.4.3-(a) with itself, which is the PSD. (b) The spectral interferogram between the pulses shown in Fig. 4.3-(a) and Fig. 4.3-(b), where one pulse is unchirped, and the other has propagated 2 m in air. (c) The spectral interferogram between the pulses shown in Fig. 4.3-(a) and Fig. 4.3-(c), where one pulse is unchirped, and the other has propagated 1 cm in BK7.

4.3.1 Mathematical analysis of the spectral interferogram

If the sample in the interferometer is only a path length difference in air, then the spectrum that is measured by spectral interferometry is:

$$\begin{aligned} S(\omega) &= |\hat{E}_m(\omega) + \hat{E}_r(\omega)|^2 \\ &= |\hat{E}_m(\omega)|^2 + |\hat{E}_r(\omega)|^2 + 2|\hat{E}_m(\omega)\hat{E}_r(\omega)|\cos\left(\varphi_r(\omega) - \varphi_m(\omega)\right) \end{aligned} \tag{4.17}$$

If the absorption in the medium is ignored, we have $|\hat{E}_m(\omega)| = |\hat{E}_r(\omega)|$, implying

$$S(\omega) = 2|\hat{E}(\omega)|^2\left[1 + \cos\left(\varphi_r(\omega) - \varphi_m(\omega)\right)\right] \tag{4.18}$$

Where $|\hat{E}(\omega)|$ is the power spectral density of the pulses. The fundamental property of the interferogram is that it is an intensity measurement that contains the phase difference $\varphi_m - \varphi_r$. This allows the reconstruction of the path-length difference. For a distance propagation in air, the interference term can be written as,

$$\varphi(\omega) = \varphi_r(\omega) - \varphi_m(\omega) = 2n(\omega)\omega(l_m - l_r)/c \tag{4.19}$$

with n and c being the refractive index of air and the speed of light in vacuum, respectively. We use $L = 2(l_m - l_r)$ as the geometrical pulse separation from both arms. By inserting Eq. 4.16 into Eq. 4.15, we have,

$$S(\omega) = 2|\hat{E}(\omega)|^2\left[1 + \cos\left(n(\omega)\omega L/c\right)\right] \tag{4.20}$$

Comparing Eq. 4.20 and Eq. 4.16, we see that, the cross correlation at a certain distance is the integral of the spectral interferogram over the frequencies. $S(\omega)$ should reach its maximum when,

$$\varphi(\omega) = n(\omega)\omega L/c = m \cdot 2\pi, \tag{4.21}$$

for some integer m. The distance between two adjacent maxima is thus,

$$\Delta\omega = 2\pi c/n(\omega)L \tag{4.22}$$

This equation shows that, the distance between the adjacent peaks in the spectrum is proportional to the inverse of the pulse separation. If the two arms of the interferometer are equal, the spectral interferogram is identical to the PSD. In Fig. 4.15 we show the spectral interferograms at different distances, using the PSD from Fig. 4.2. The path-length difference from (a) to (e) is -40μm, -20μm, 0μm, 20μm and 40μm respectively. The spectral interferogram is symmetric to the zero-displacement. This is called the twin-image ambiguity.

Now Eq. 4.20 is written for a continuous spectrum. In our case we use the frequency comb, thus

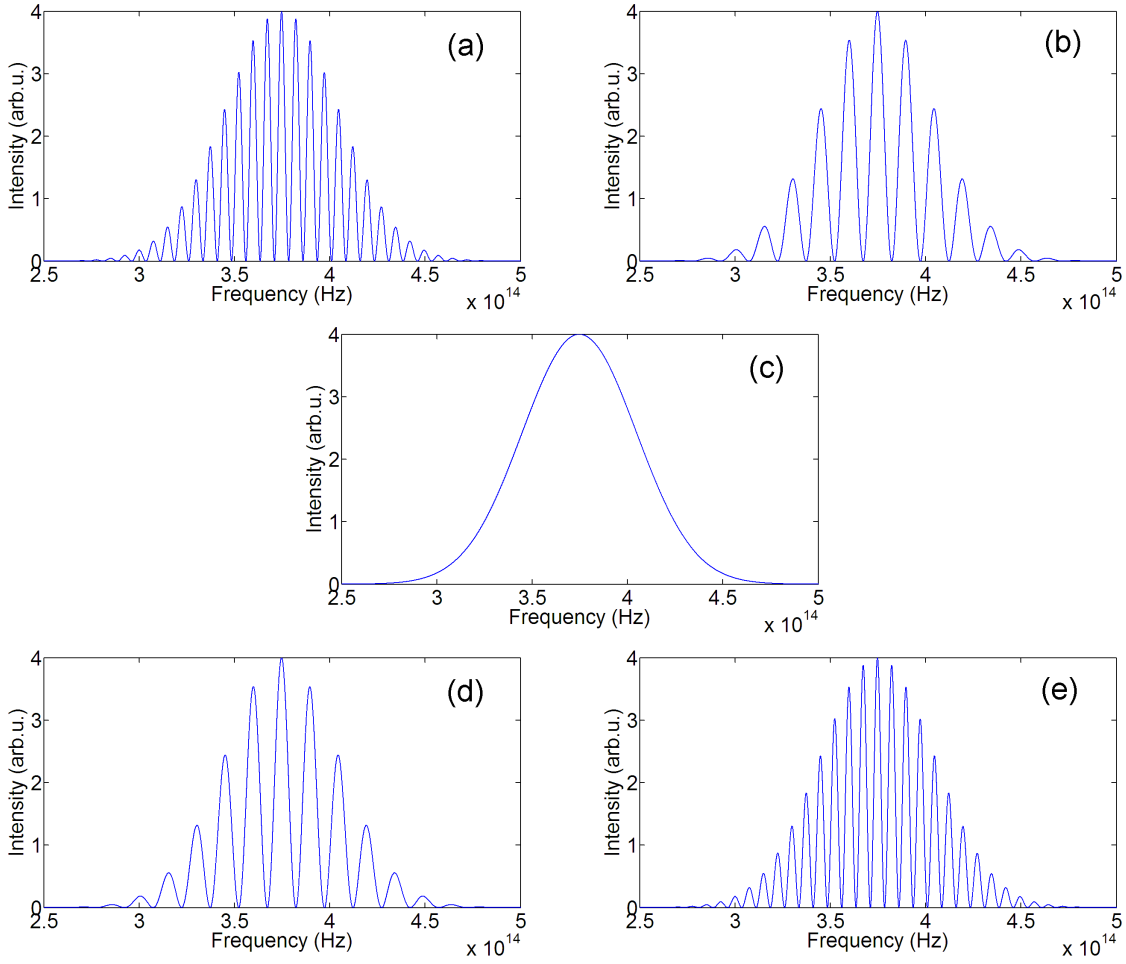

Figure 4.15: The spectral interferograms at around equal arms of the interferometer, using the symmetric PSD from Fig. 4.2. The path-length difference from (a) to (e) is -40 μm, -20 μm, 0 μm, 20 μm and 40 μm respectively.

Eq. 4.20 applies only to the frequencies of the comb *i.e.* to $\omega_n = n \cdot \omega_r + \omega_0$ where n is the mode number. We observe that the cosine term has a period of the inter-pulse distance L_{pp}. In order to show this, let us consider,

$$L = m \cdot L_{pp} + \Delta L \tag{4.23}$$

where the first term is a multiple of inter-pulse distance and the second is a short distance. Substitute Eq. 4.23 into Eq. 4.20, we have,

$$S(\omega) = 2|\hat{E}(\omega)|^2 \left[1 + \cos\left(n(\omega) n m \omega_r L_{pp}/c + n(\omega) n \omega_r \Delta L/c + n(\omega) m \omega_0 L_{pp}/c + n(\omega)\omega_0 \Delta L/c\right)\right] \tag{4.24}$$

The third and fourth terms inside the cosine are dependent only on ω_0 and cause only a shift of the phase. For the remaining analysis, the terms containing ω_0 are ignored, then, Eq. 4.24 can be written as,

$$S(\omega) = |\hat{E}(\omega)|^2 \left[1 + \cos\left(n(\omega) n m \omega_r L_{pp}/c + n(\omega) n \omega_r \Delta L/c\right)\right] \tag{4.25}$$

If the pulse propagates in vacuum, then $n(\omega)$ is one and the first term will be a multiple of 2π, which means that the modulated spectrum will exactly repeat after every multiple of the cavity length. For the pulse propagating in air, $n(\omega)$ is not one and the period is lost because of dispersion.

4.3.2 The spectral interferogram of a symmetric power spectral density

It is useful to see how the first term inside the cosine in Eq. 4.25 influences the interferogram when the path length difference is changed. To investigate this, we use the symmetric PSD from Fig. 4.2. The measurement arm is $500 \times l_{pp/2}$ (2.5 m, single way) longer than the reference arm. In Fig. 4.16 we show the interferograms at $500 \times L_{pp} - 40\mu m$, $500 \times L_{pp} - 20\mu m$, $500 \times L_{pp}$, $500 \times L_{pp} + 20\mu m$, $500 \times L_{pp} + 40\mu m$ path length difference respectively. Now, even at exactly $500 \times L_{pp}$, we see some modulations because the group velocity used to calculate L_{pp} is only correct for the central frequency of the PSD. This arises because unlike the center frequency, each frequency component of the PSD encounters a different refractive index and propagates a different distance, which is not exactly a multiple of the L_{pp}. The figures at $500 \times L_{pp} - 40\mu m$ and $500 \times L_{pp} - 40\mu m$ are symmetric. Denser fringes mean a longer distance between the interfering pulses. Since the refractive index of air is not a linear function, the chirp of the interferogram is also not linear.

Although at the path length difference of $500 \times L_{pp}$ the interferogram shows chirp, we can compare Fig. 4.16-(a) and Fig. 4.16-(e) with Fig. 4.15-(a) and Fig. 4.15-(e), which are identical. We make the following important observation, that the density of the maxima, at the regions close to the central frequency are the same. This is shown in Fig. 4.17-(a), (b) and (c). If we concentrate only on a small region around the central frequency, marked by the darker rectangle in Fig. 4.17, the distance between adjacent peaks is the same. We will use this in chapter 6, where we reconstruct the distance information from these spectral interferograms.

Figure. 4.18 shows the spectral interferomgrams when the path length difference is exactly a multiple of inter-pulse distance. The simulation ranges from $0 \times L_{pp}$ to $1000 \times L_{pp}$ (10 m, back and forth). The central frequency, which is propagated with the group velocity, v_g, forms always a minimum or a maximum. These figures look symmetric, but we know that they deviate from symmetric because of the nonlinearity of the refractive index of air in this frequency range.

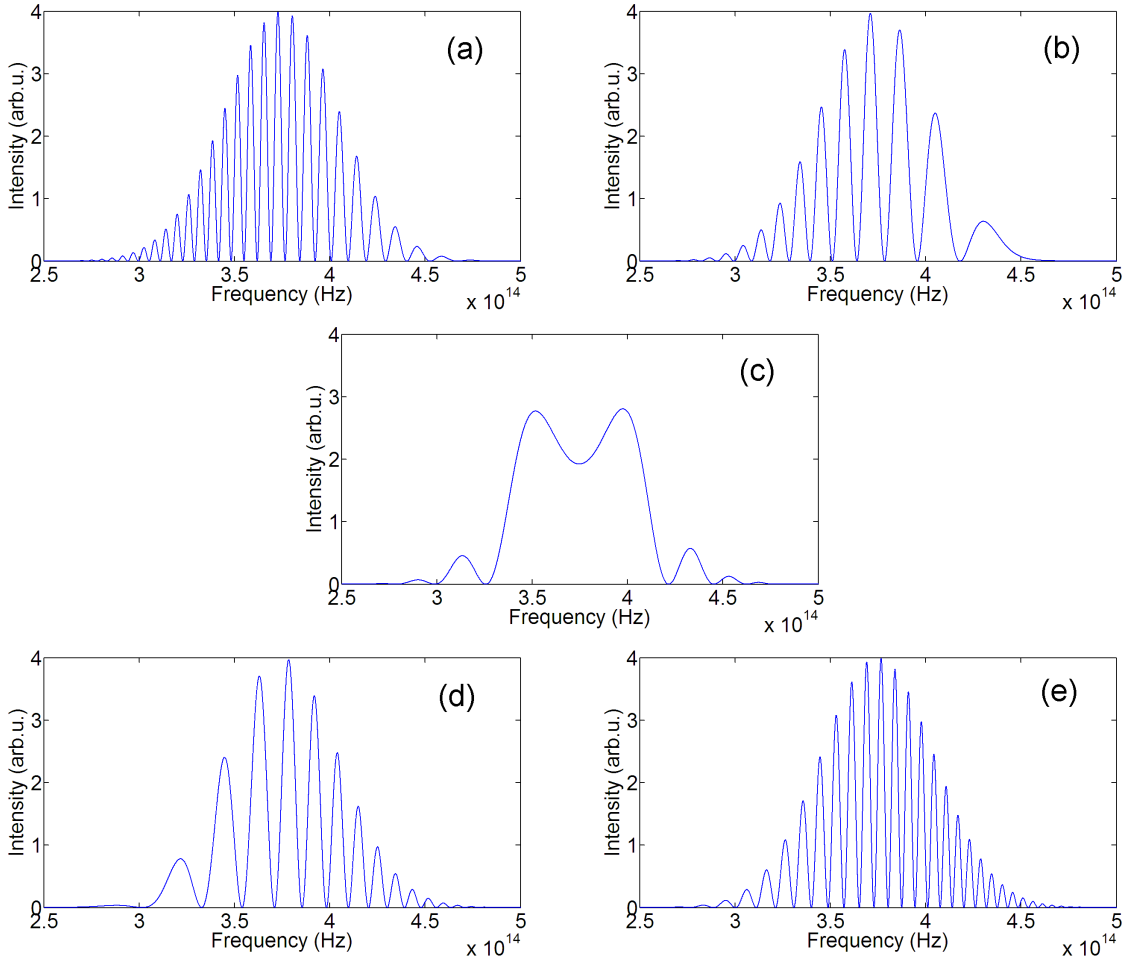

Figure 4.16: The spectral interferograms around $500 \times L_{pp}$, using the symmetric PSD from Fig. 4.2. The path-length difference from (a) to (e) is $500 \times L_{pp} - 40\mu m$, $500 \times L_{pp} - 20\mu m$, $500 \times L_{pp}$, $500 \times L_{pp} + 20\mu m$, $500 \times L_{pp} + 40\mu m$ respectively.

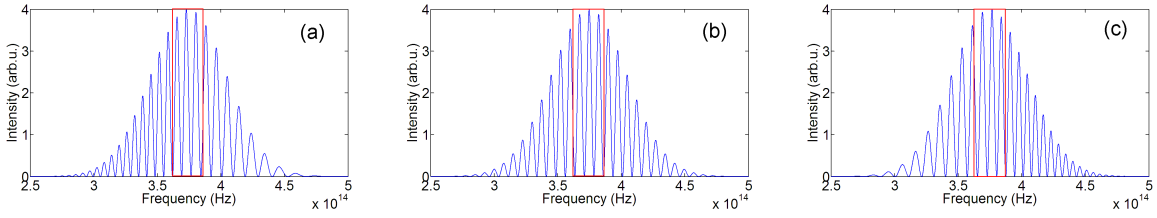

Figure 4.17: Comparison between spectral interferograms shown in Fig. 4.16-(a) and Fig. 4.16-(e) with Fig. 4.15-(a) and Fig. 4.15-(e), which are identical. (a) $500 \times L_{pp} - 40\mu m$ as shown in Fig. 4.16-(a). (b) $0 \times L_{pp} \pm 40\mu m$ as shown in Fig. 4.15-(a) and Fig. 4.15-(e). (c) $500 \times L_{pp} + 40\mu m$ as shown in Fig. 4.16-(e). The density of the maxima, at the regions close to the central frequency are the same, as marked by the dark rectangle in each case.

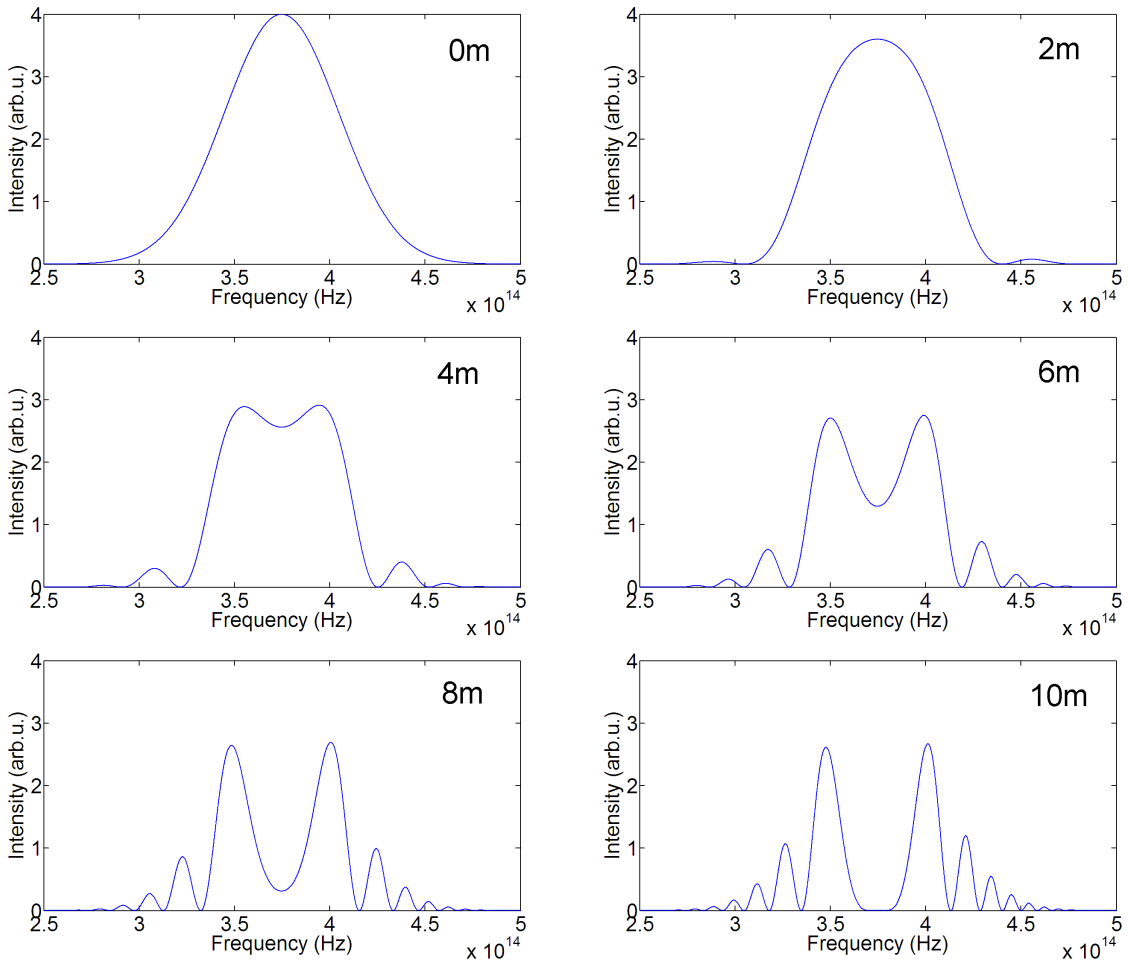

Figure 4.18: The spectral interferomgrams when the path length difference is exactly a multiple of inter-pulse distance. The simulation ranges from $0 \times L_{pp}$ (0 m) to $1000 \times L_{pp}$ (10 m, back and forth).

4.3.3 The spectral interferogram of an asymmetric power spectral density

To study the effects of an asymmetric PSD on the spectral interferogram, we use the asymmetric PSD in Fig. 4.9 to generate the interferograms. When the two arms of the interferometer are approximately equal, the modulated spectra are shown in Fig. 4.19. The path-length differences from (a) to (e) are -40μm, -20μm, 0μm, 20μm and 40μm respectively. Just like a symmetric PSD, the spectral interferogram is symmetric to the zero-displacement.

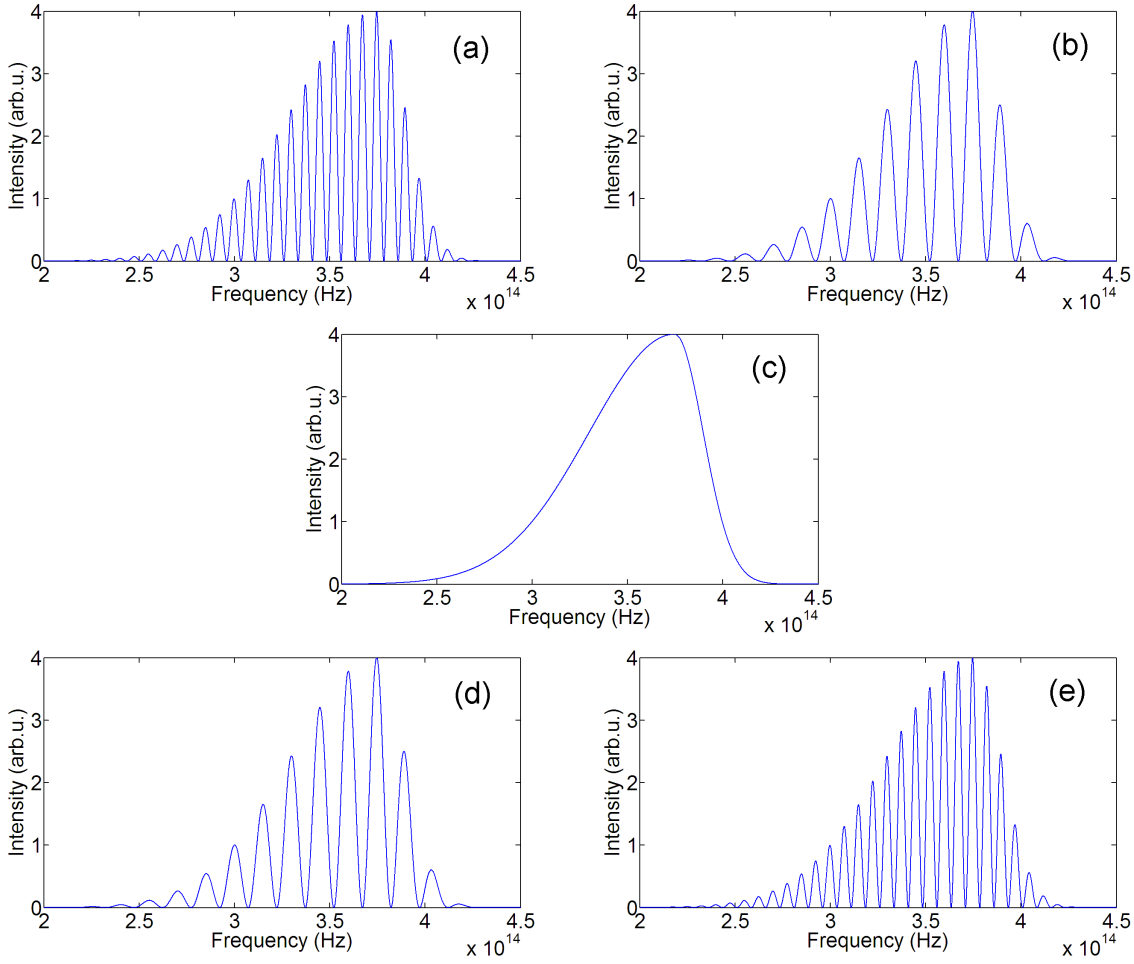

Figure 4.19: The spectral interferograms at around equal arms of the interferometer, using the asymmetric PSD from Fig. 4.9. The path-length difference from (a) to (e) is -40 μm, -20 μm, 0 μm, 20 μm and 40 μm respectively.

If the two arms are unbalanced, the interferogram will be chirped. In Fig. 4.20 we show the interferograms at $500 \times L_{pp} - 40\mu m$, $500 \times L_{pp} - 20\mu m$, $500 \times L_{pp}$, $500 \times L_{pp} + 20\mu m$, $500 \times L_{pp} + 40\mu m$ respectively. We observe that most of the properties of these spectrograms are similar to those generated using a symmetric PSD. For example, again at exactly $500 \times L_{pp}$, we see some modulations because the group velocity used to calculate L_{pp} is only correct for the frequency at the maximum of the PSD.

Here again, we make the following important observation, that the density of the maxima, at the regions close to the frequency at the maximum of the PSD are the same. This is shown in Fig. 4.21-(a), (b) and (c). If we concentrate only on a small region around the frequency at the maximum

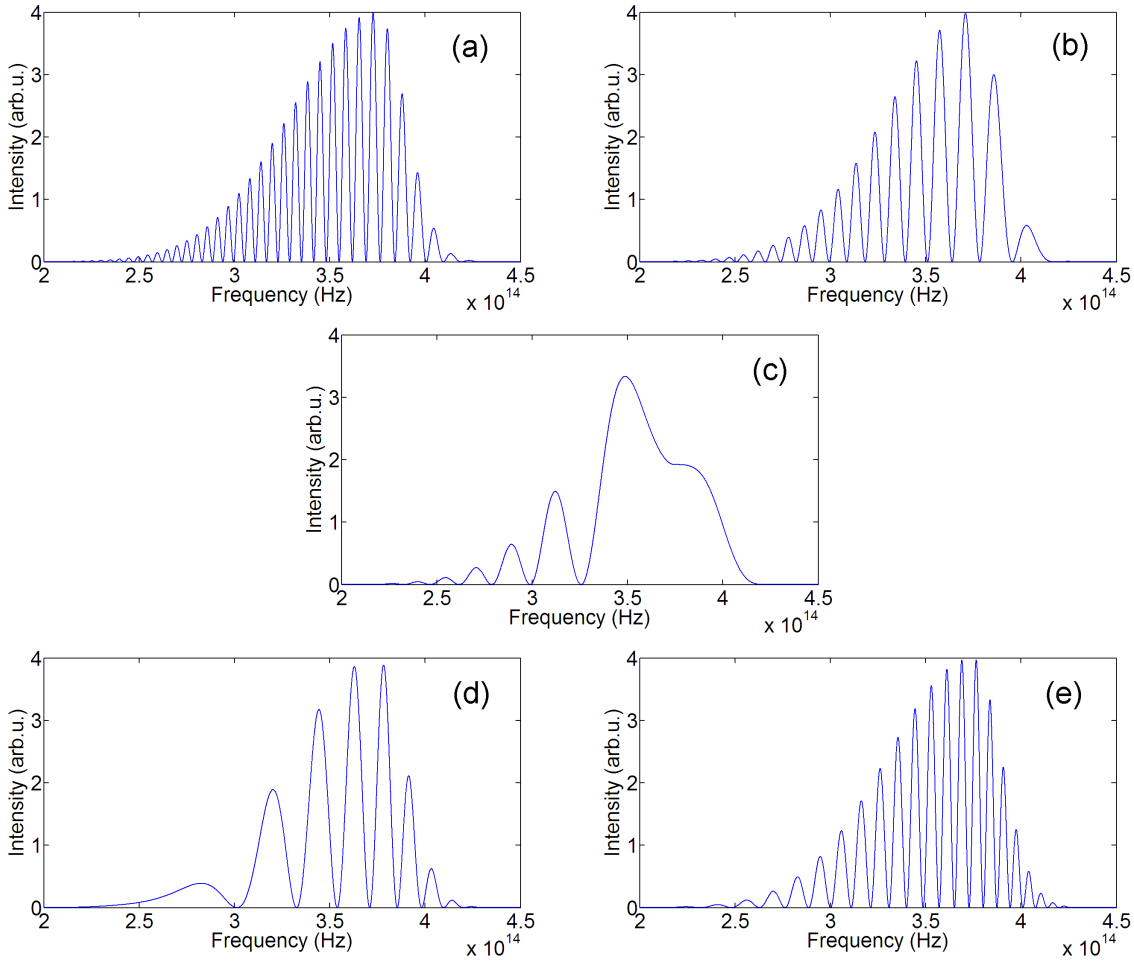

Figure 4.20: The spectral interferograms around $500 \times l_{pp}$, using the asymmetric PSD from Fig. 4.9. The path-length difference from (a) to (e) is $500 \times L_{pp} - 40\mu m$, $500 \times L_{pp} - 20\mu m$, $500 \times L_{pp}$, $500 \times L_{pp} + 20\mu m$, $500 \times L_{pp} + 40\mu m$ respectively.

of the PSD, marked by the darker rectangle in Fig. 4.21, the distance between adjacent peaks is the same. Why the peak densities are the same, only close to the maximum of the PSD. The key is, this is not because this region is close to the peak or not, but because this region is around the frequency which has been used to calculate L_{pp}. Each frequency in the PSD propagates at its own speed, but L_{pp} is calculated by the group velocity at one perticular frequency. We will use this idea in chapter 6, where we reconstruct the distance information from these spectral interferograms.

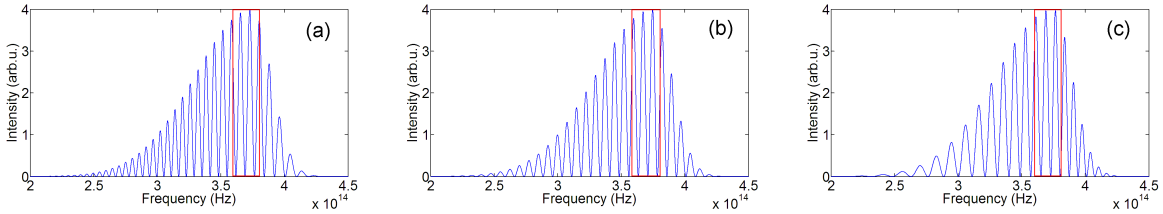

Figure 4.21: Comparison between spectral interferograms shown in Fig. 4.20-(a) and Fig. 4.20-(e) with Fig. 4.19-(a) and Fig. 4.19-(e), which are identical. (a) $500 \times L_{pp} - 40\mu m$ as shown in Fig. 4.20-(a). (b) $0 \times L_{pp} \pm 40\mu m$ as shown in Fig. 4.19-(a) and Fig. 4.19-(e). (c) $500 \times L_{pp} + 40\mu m$ as shown in Fig. 4.20-(e). The density of the maxima, at the regions close to the frequency at the maximum of the PSD are the same, as marked by the dark rectangle in each case.

In Fig. 4.22 we show the spectral interferomgrams when the path length difference is exactly a multiple of inter-pulse distance. The simulation ranges from $0 \times L_{pp}$ to $1000 \times L_{pp}$ (10 m, back and forth). The maximum frequency, which is propagated with the group velocity v_g, is not necessarily a minimum or a maximum, but the derivative of the modulated spectrum at this frequency is always zero.

4.4 Relation between the cross correlation and the spectral interferogram

4.4.1 The difference between the position of the maximum of the cross correlation function and the multiple of the inter-pulse distance

We would like to study the origin of the difference between the position of the maximum of the cross correlation function and the multiple of the inter-pulse distance. Initailly we consider the case of the pulses with symmetric PSD. For this, we compare Eq. 4.16 to Eq. 4.19, we observe that the intensity at a certain point of the cross correlation is only the weighted sum of the spectral interferogram. We consider the spectral interferogram of a symmetric spectrum, for example, Fig. 4.16-(a) where we calculated the spectral interferogram for $500 \times L_{pp} - 40\mu m$. The spectral interferogram is chirped, because of the group delay dispersion of air. If we integrate this spectral interferogram, the fast oscillating part from the left should be compensated by the slow oscillating part from the right. The integral should be the same as when the spectral interferogram in Fig. 4.15-(a), which corresponds to the case of $0 \times L_{pp} - 40\mu m$, is integrated. This cancellation of the integral of the two sides of the spectral interferogram is zero only if the chirp is linear. But this is not the case for pulse propagation in air. When the quadratic behavior of the refractive index is considered, the integral of the spectral interferogram shown in Fig. 4.16-(a) will deviate from that of Fig. 4.15-(a). Therefore the position of the maximum of the correlation patterns, which are formed by the weighted sums of chirped spectral interferograms, differ from the position of a multiple of cavity length.

When we consider the case where the PSD is asymmetric, more deviations are introduced. This is mainly because the spectral interferogram is even more asymmetric to the maximum of the PSD,

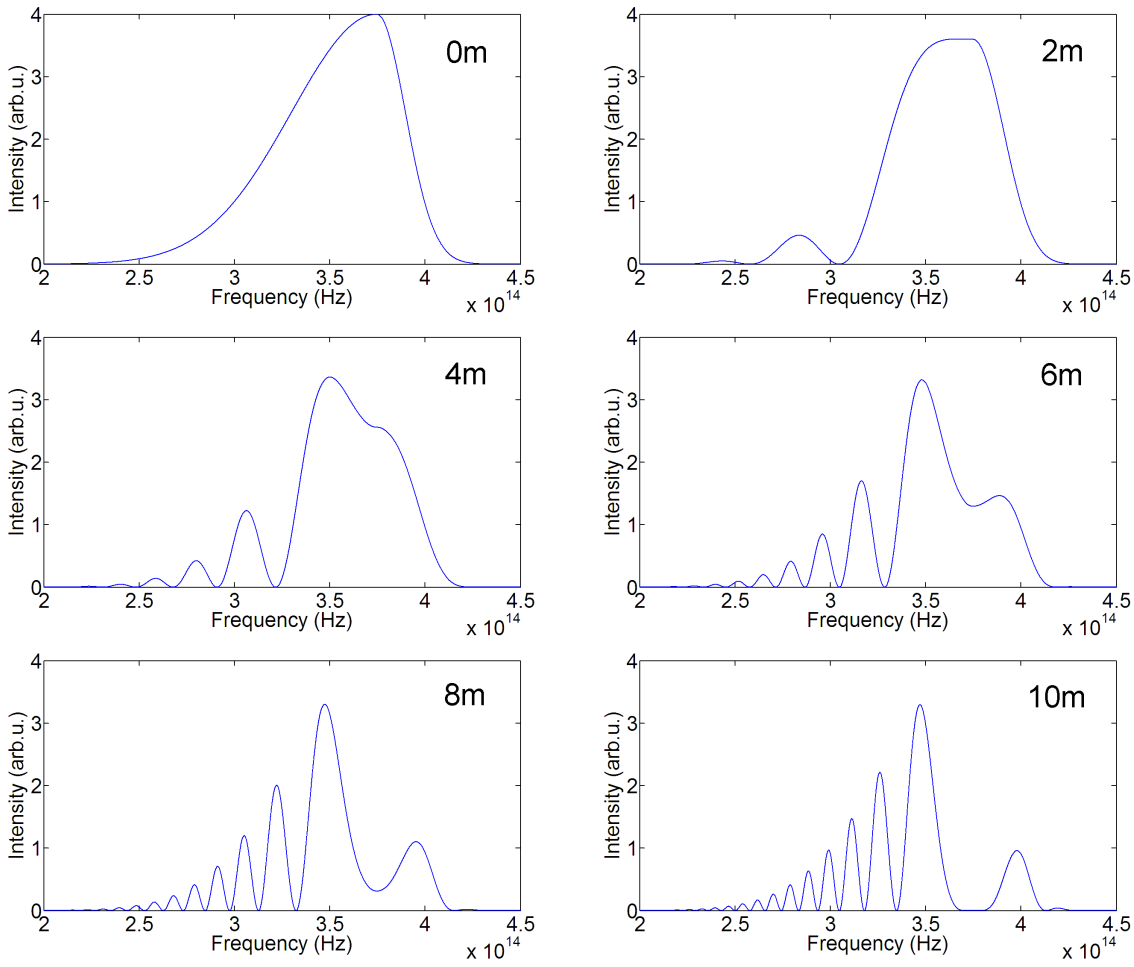

Figure 4.22: The spectral interferomgrams when the path length difference is exactly a multiple of inter-pulse distance. The simulation ranges from $0 \times L_{pp}$ (0 m) to $1000 \times L_{pp}$ (10 m, back and forth).

caused not only by the non-linearity of the refractive index of air, but also the asymmetry of the PSD itself. For this we refer to Fig. 4.20-(a), where we calculated the spectral interferogram for $500 \times L_{pp} - 40\mu m$. The integral of the slowly oscillating part in the right of the spectral interferogram does not compensate the fast oscillating part in the left. This is the reason for an asymmetric PSD, the cross correlation function is more chirped than the one of a symmetric PSD [67].

In both symmetric and asymmetric PSD, the position of the brightest fringe of the cross correlation, does not necessarily coincide with the position of the fringe which is a multiple of L_{pp}. This is shown in Fig. 4.23. The cross correlation, shown in Fig. 4.23-(a), is calculated from an asymmetric PSD at 10 m path length difference. The brightest fringe is the integral of the spectral interferogram shown in Fig. 4.20-(b), but not from the spectral interferogram at a multiple of L_{pp}, as shown in Fig. 4.20-(c).

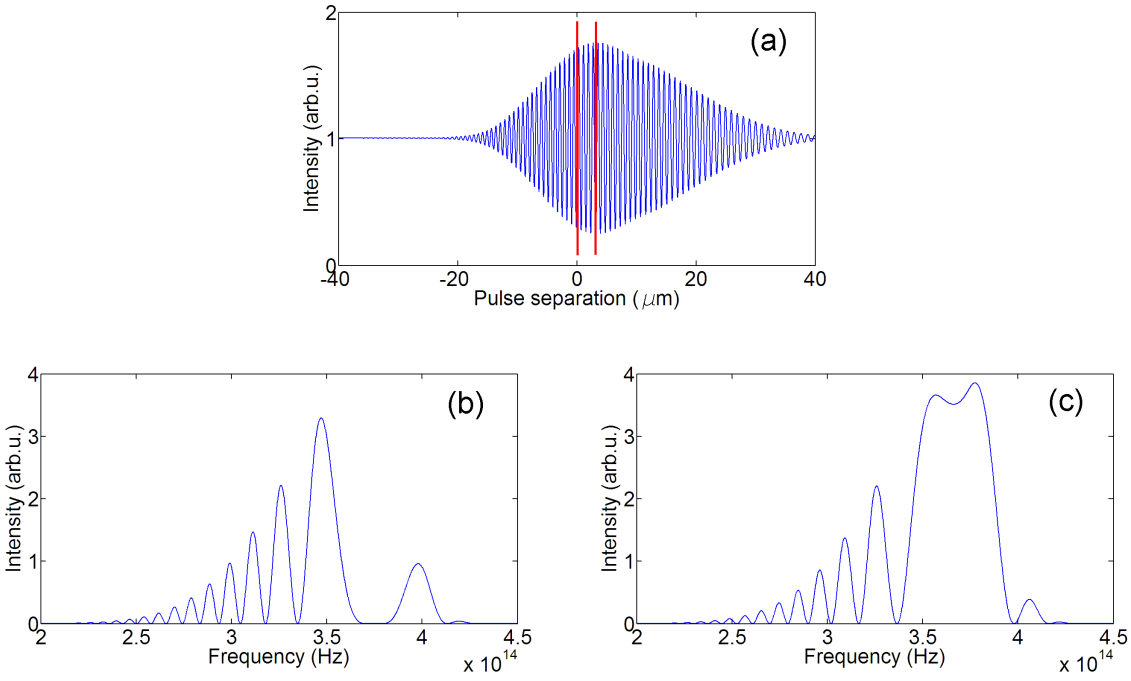

Figure 4.23: (a) The cross correlation calculated from an asymmetric PSD at $1000 \times L_{pp}$. (b) Spectral interferogram which made the brightest fringe of the cross correlation. (c) Spectral interferogram at $1000 \times L_{pp}$

4.4.2 The spectrogram

Combine the Fourier transform spectrometer and dispersive grating interferometry, we can generate a two dimensional image. This kind of image is often called a spectrogram. In Fig. 4.24 we show the spectrogram using the symmetric PSD from Fig. 4.2-(a) at around equal arms. Here the x-axis is the displacement and the y-axis is the frequency. A spectrogram contains both the cross correlation and the spectral interferograms. If we integrate the spectrogram column by column, we will obtain the cross correlation function. Also if the spectrogram is integrated row by row, we get the PSD. Although a two-dimensional image looks more impressive than a cross correlation or the spectral interferogram, it doesn't yield more information than the PSD and the unbalanced phase difference. In Fig. 4.25, we show a spectrogram for a pulse having a symmetric PSD, for a path-length difference of $1000 \times L_{pp}$ (10 m, back and forth). We can clearly observe the chirp in the spectrogram.

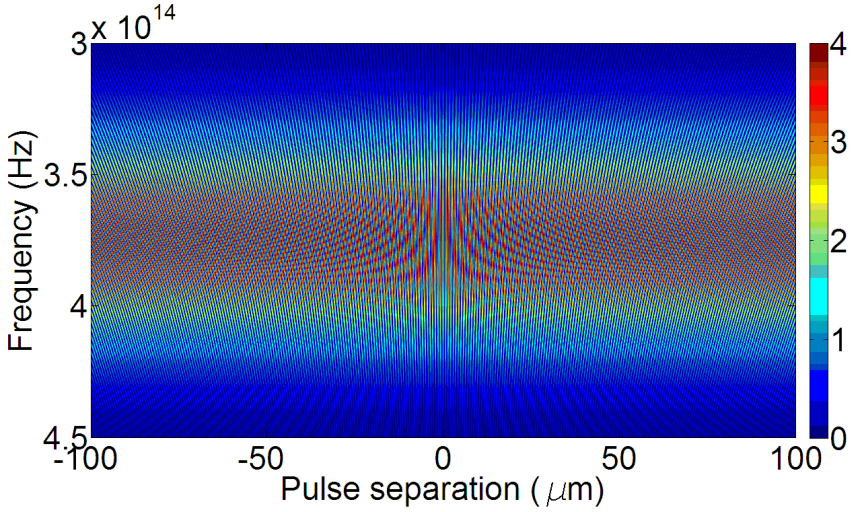

Figure 4.24: The spectrogram using the symmetric PSD from Fig. 4.2-(a) at around equal arms.

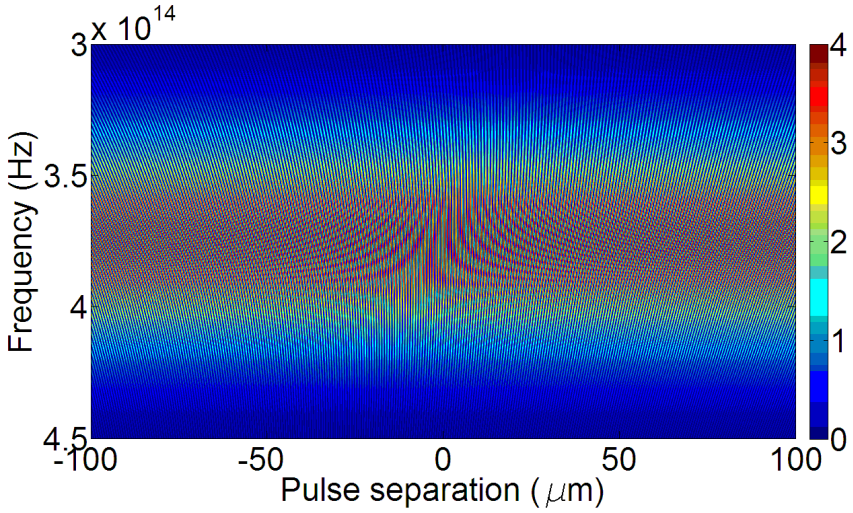

Figure 4.25: The spectrogram for a pulse having a symmetric PSD from Fig. 4.2-(a), for a path-length difference of $1000 \times L_{pp}$ (10 m, back and forth)

Chapter 5

Distance measurement using correlations

5.1 Cross correlations in an unbalanced Michelson interferometer

In 2004, The first schemes, for absolute length metrology by using a phase-stabilized optical frequency comb, were proposed [17]. The main idea was to measure cross correlations in an unbalanced Michelson interferometer. In Fig. 5.1 we show the schematic of a typical experimental setup. After the beam splitter, the beam divides into two. One part of the beam is reflected by a hollow corner cube mounted on a piezo-electric transducer (PZT). We call this the short reference arm. The other part of the beam propagates along the long measurement arm and is reflected by another hollow corner cube. The returning beams are overlapped and focused onto a slow detector. A cross correlation function will be observed whenever the path length difference between the two arms is a multiple of the half laser cavity length $l_{pp/2}$. We scan the reference arm and observe the first correlation when the two arms of the interferometer are equal. Subsequently the hollow corner cube mounted on a mechanical car is moved over an arbitrary long distance. The reference arm is then scanned again to search for another cross correlation function. The path length difference now is close to a multiple of the inter-pulse distance L_{pp}, or in other words, the laser cavity length. Now if we label the displacement of the measurement arm as $|AB| = \Delta l_m$, the displacement of the reference arm as $|ab| = \Delta l_r$, the length difference between the two displacements should be related by,

$$\Delta l_m = m \cdot l_{pp/2} \pm \Delta l_r \tag{5.1}$$

Here, m is an integer number and Δl_r is the displacement of the reference arm which is less than half of the cavity length and can be measured with high accuracy. The half of the laser cavity length, or, the half of the inter-pulse distance, is $l_{pp/2}$ which can be calculated by,

$$l_{pp/2} = c/\left(2 v_g f_r\right). \tag{5.2}$$

Here c is the speed of light in vacuum and v_g is the group velocity of pulse calculated at the central frequency of the PSD, *i.e.*

$$v_g = c\left(n_0 - \lambda_0 \frac{dn(\lambda)}{d\lambda}|_{\lambda_0}\right)^{-1}. \tag{5.3}$$

The central wavelength of the pulse is λ_0 and n_0 is the refractive index of air at λ_0. This definition is only valid for a symmetric power spectral density (PSD) and for short distances where the group delay dispersion (GDD) of air can be ignored. The case of an asymmetric PSD or where the GDD of air is not neglectable will be discussed later in the chapter.
The integer number m can be determined with an ambiguity range of half the inter-pulse distance, which is around tens of centimeters for a typical femtosecond laser. In Jun Ye's paper [17] in 2004, it

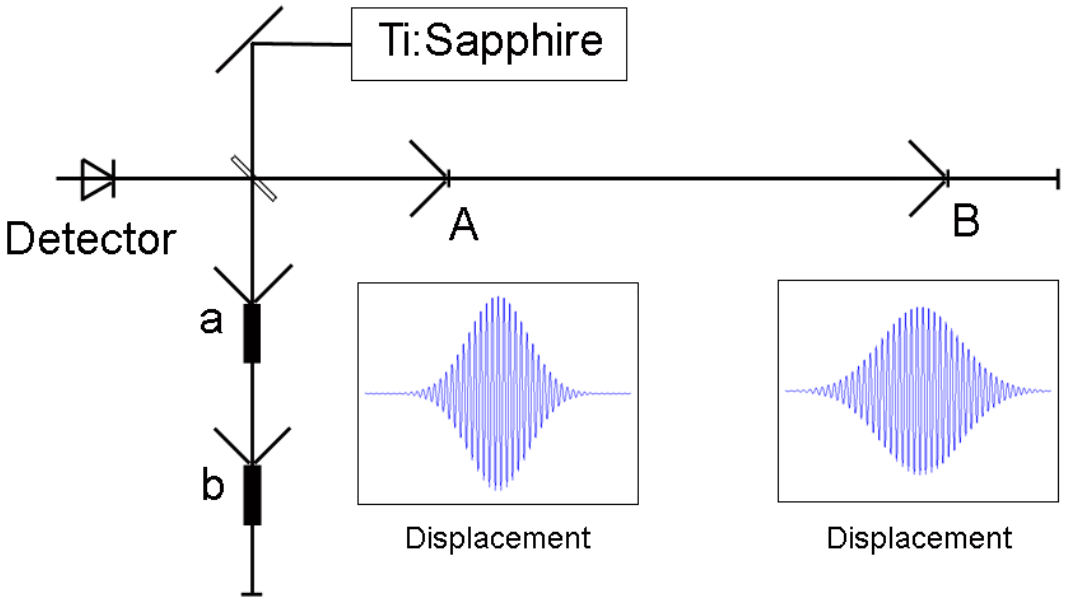

Figure 5.1: The schematic of a typical experimental setup for distance measurement using correlations

is suggested that m is measured, by shifting the repetition frequency f_r. It is also possible to measure m by other ways such as a time-of-flight measurement. Jun Ye originally suggested that the combined beams are focused onto a second harmonic crystal and the fringe resolved cross correlations are observed by an APD. In our experiment, we discovered that this is not really necessary, mainly because of the power requirements for really long propagation lengths. Also, Ye's paper was for an experiment to be done in vacuum and did not consider the dispersion introduced due to pulse propagation in air. In the previous chapter, chapter 4, we discuss how the group delay dispersion of the pulse in air makes the idea of group velocity invalid. Thus making the definition of v_g in Eq. 5.2 inapplicable.

5.2 Measurement of short distances using cross correlations

Our first experiments in 2007 using this principle involved the measurement of a short displacement ($l_{pp/2}$) and comparison of the results with a counting laser interferometer [68]. For a short path length difference, in the order of a few cavity length, the group delay dispersion of air can be ignored. This is not the case when the path length differnce extends to tens of cavity length.

5.2.1 Experimental setup

A schematic of the experimental setup we used, in the VSL laboratory, is shown in Fig. 5.2. The measurements are carried out with a mode-locked Ti:Sapphire laser with a pulse duration of around 40 fs. Both the repetition frequency f_r and the carrier-envelope-offset frequency f_0 are locked and referenced to a cesium clock. The output wavelength of the pulse is centered at around 820 nm with a spectral bandwidth of 20 nm. The repetition frequency was approximately 1 GHz, corresponding to a cavity length of the laser of about 30 cm, for most of our experiments. The pulses from the laser are split into two at the beam splitter. One part of the pulse goes into the non-varying reference arm of the interferometer with length l_r and is reflected by a hollow gold coated retro-reflector.

The other part of the pulse goes into the measurement arm with length l_m. The length of this arm can be varied with a translation stage (PI M series 15 cm translation range). Another gold coated retro-reflector was mounted on a piezo-electric transducer (PZT) on top of the translation stage. During the measurement, the retro-reflector is scanned using the PZT with a frequency of 1 Hz using a saw-tooth voltage. The PZT can scan a maximum of around 40 microns. The two reflected beams coincide with each other and are focused inside a Barium Borate Crystal (BBO) for second harmonic generation. A filter was used to block the original infrared light. The second harmonic signal generated in the crystal was focused onto an avalanche photo diode (APD). The intensity of the second harmonic signal was measured with an oscilloscope.

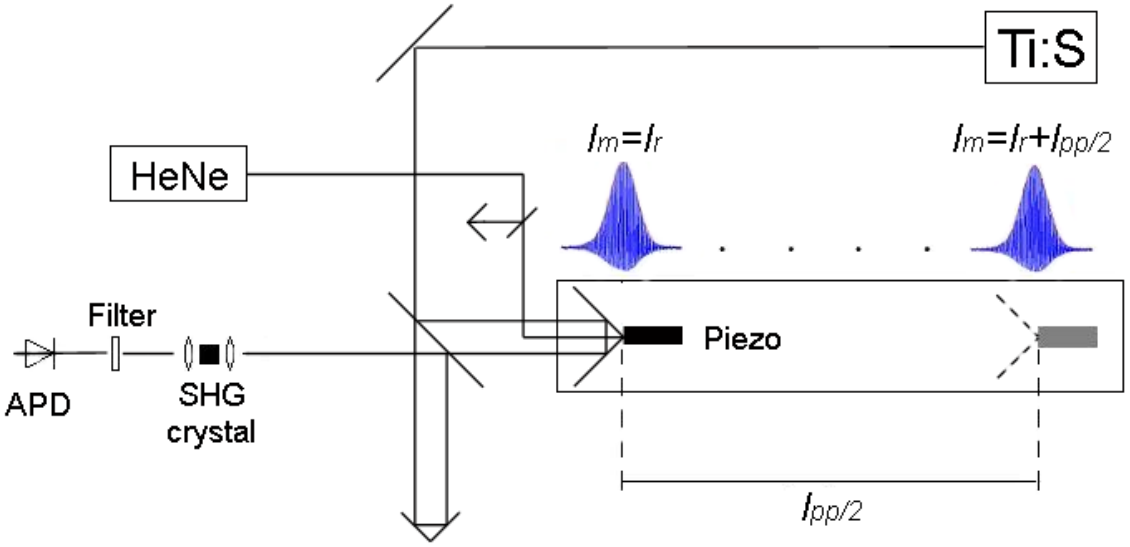

Figure 5.2: Schematic of the experimental setup used to measure a short distance using cross correlations. A pulse train is sent into an interferometer and cross-correlation functions are measured at two positions of the translation stage, separated by a distance $l_{pp/2}$. Simultaneously, the displacement is measured with a Zeeman-stabilized HeNe fringe counting laser interferometer.

5.2.2 Measurement procedure

The experiment is done as follows. First the translation stage is positioned at A where l_r and l_m are equal. Here an auto-correlation function was measured using the oscilloscope. Then the stage was translated to position B such that l_m was approximately equal to $l_r + l_{pp/2}$. At this position a cross correlation function is measured. Since the translation stage has a finite step size, 300 nm, it was not always possible to position the stage such that the maximum value of the cross correlation function at position B occured at exactly the same piezo voltage, *i.e.* scan position, as at position A. Therefore, to determine the maximum of the pulse overlap, Gaussian functions were fit through the profiles of the two recorded correlation patterns. By comparing the extracted maximum of the cross-correlation with the auto-correlation, a correction term δ was obtained. This procedure is shown in Fig. 5.3. The real displacement Δl_m of the retro-reflector was,

$$\Delta l_m = l_{pp/2} + \delta/2 \tag{5.4}$$

The displacement Δl_m was measured independently using a calibrated He-Ne fringe counting laser

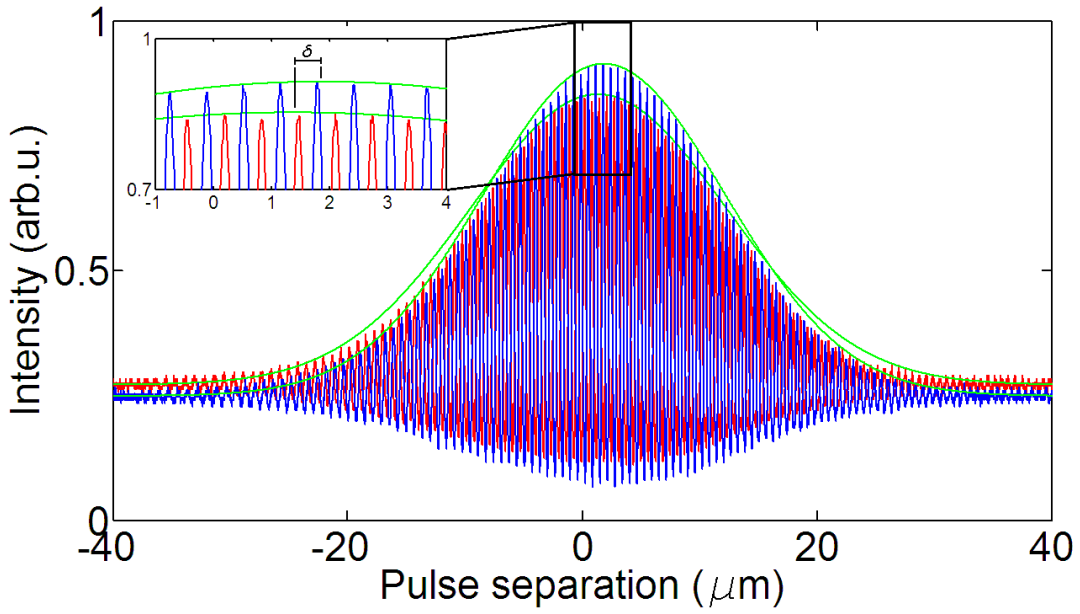

Figure 5.3: Comparison of the two cross-correlation functions at position A (higher) and B (lower). Note the small shift between these two. This shift is determined by Gaussian curve fitting of both measurements.

interferometer. The fluctuation of the temperature in the laboratory was controlled to be less than 0.1 °C, and also the air pressure change was measured to be within 1 hPa. the uncertainty on the He-Ne laser was dominated by the 40 cm dead path length and is estimated to be around 50 nm as specified in the manual. This value is much smaller than the fluctuations seen in the measurements done with the Ti:Saphire laser. A position sensitive detector is used for the alignment of the beams parallel to the translation direction of the stage, leading to a negligible alignment error.

5.2.3 Measurement results

The whole experiment including the control measurement was carried out for six independent values of the repetition frequency f_r. The first three were carried out with the temperature stabilized at 20.17 °C and air pressure at 1011.2 hPa. The last three measurements took place at modified environmental conditions given by T = 20.11 °C and p = 1025.2 hPa. The group velocities were calculated by using the updated Edlèn equation [35], and are 299710681 m/s and 299709555 m/s for the two sets of environmental conditions, respectively. Each of the measurements by the frequency comb is repeated ten times and the results are shown in Table.5.1. The distance measurements using the femtosecond laser agree with the reference measurement using the He-Ne laser within less than half of a wavelength, *i.e.* 316 nm [68]. The standard deviation of the measurements is attributed to the jitter in the detection system which causes the cross-correlation function to shift from time to time. For the time scales which play a role in this measurement the timing jitter of the frequency comb laser can be neglected in comparison to the other sources. The jitter has contribution arising from the vibration of the setup, fluctuations in the air and electrical drifts. The piezo-element was powered by a function generator and a high voltage power supply. We suspect that the main contribution was the drifts in the high voltage power supply and the resulting vibration of the piezo on the translation stage.

$l_{pp}/2$ (nm)	Displacement $\delta_c/2$ (nm)	Measured distance frequency comb(nm)	Reference distance He-Ne laser (nm)	Difference (nm)
147,765,420	+396	147,765,816 ± 112	147,765,593	+223
147,765,493	-571	147,764,922 ± 250	147,764,996	-74
147,765,566	-836	147,764,730 ± 339	147,764,815	-85
147,779,205	-261	147,778,944 ± 224	147,779,054	-110
147,779,278	-124	147,779,154 ± 276	147,779,464	-310
147,779,351	+128	147,779,479 ± 174	147,779,383	+96

Table 5.1: Measurement results using the two lasers. The average of ten measurements of the frequency comb is shown along with the standard deviation below it. The first three were carried out with the temperature stabilized at 20.17 °C and air pressure at 1011.2 hPa. The last three measurements took place at modified environmental conditions given by T = 20.11 °C and p = 1025.2 hPa. The group velocities were calculated by using the updated Edlèn equation, and are 299710681 m/s and 299709555 m/s for the two sets of environmental conditions, respectively.

5.3 Measurement of long distances with cross correlations

5.3.1 Experimental setup

After we sucessfully measured a short displacement in 2007, we moved the experimental setup to the 50 m long corridor in VSL laboratory. In 2008, our experimental setup was ready and is shown in Fig. 5.4. The new experiment was done in two adjacent rooms. The Ti:Sapphire laser based frequency comb was located in the room on the left, where we did the short distance measurement. Two achromatic lenses were used in order to minimize the divergence of the beam, before the collimated beam was transported through a hole on the wall to the interferometer in the long corridor. The reference arm consisted of a hollow corner cube mounted on a piezo-electric transducer (PZT) placed on the translation stage described before. The measurement arm consists of two dispersion compensated mirrors and a gold coated retroreflector mounted on a mechanical stage of the 50 m long measurement bench. One of the mirrors is coated for high reflectivity for 820 nm and high transmission at 633 nm. This was done so that the HeNe fringe counting laser interferometer could be used for a comparison measurement at the same time. A compensation window is used in the long arm to compensate the dispersion of the plate beam splitter, arising due to the different lengths in glass encountered by the two beams of the interferometer. The returning beams are overlapped and focused on a avalanche photo diode. When the total path length difference between both arms is a multiple of L_{pp} a coherence maximum appears. Field cross correlation functions are then obtained by modulating the PZT at 50 Hz with a sine modulation with a range of 80 μm. The beam of a helium-neon (He-Ne) laser interferometer co-propagates with the frequency comb and measures the displacement of the long arm independently. Figure. 5.5 shows some photographs of the hole on the wall and 50 m bench in the long corridor.

Figure 5.4: Schematic of the experimental setup used to measure distances in the 50 m corridor using cross correlations. We can see that the experiment was located in two adjacent rooms. The Ti:Sapphire laser based frequency comb was located in the room on the left. The beam was transported through a hole on the wall to the interferometer in the long corridor. The reference arm consists of a hollow corner cube mounted on a piezo-electric transducer (PZT) placed on the translation stage. The measurement arm consists of two dispersion compensated mirrors and a gold coated retroreflector mounted on a mechanical stage of the 50 m long measurement bench. The HeNe fringe counting laser interferometer was used for a simultaneous comparison measurement. The returning beams were overlapped and focused on a avalanche photo diode.

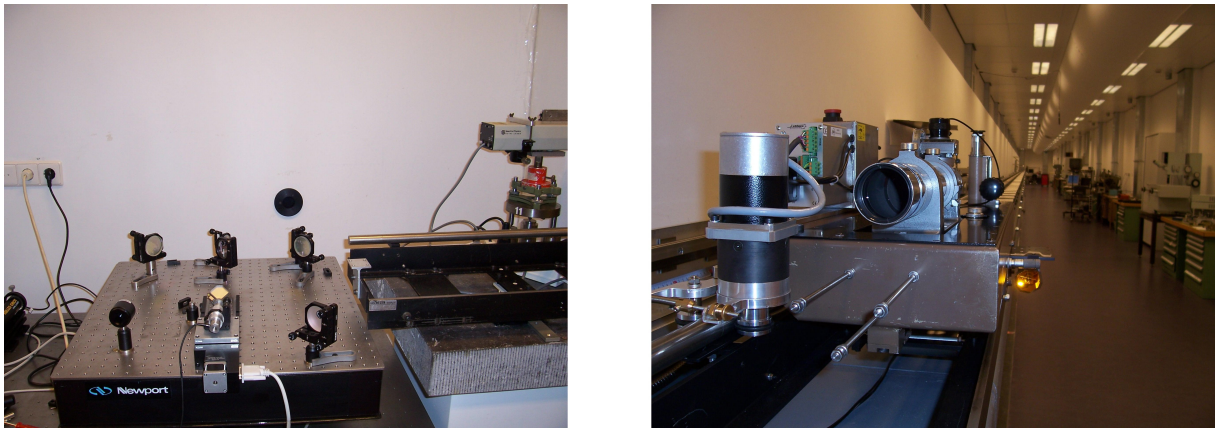

Figure 5.5: Photographs of experimental setup in the long corridor. (a) We can see the hole on the wall which transport the beam to the long corridor. (b) We can see the mechanical car carrying the retroreflector, which constitutes the long measurement arm of the interferometer.

5.3.2 Modifications implimented in the experimental setup

We made a lot of changes in our new experimental setup as compared to the setup for the short displacement measurement in Fig. 5.2.

- **Field cross correlations**. Although in our initial measurements we used the second order cross correlations, we observed that there was no advantage of doing this as compared to measuring field cross correlations. In fact there is an obvious advantage of using the linear measurement. This is that the requirements on beam power are lowered. To generate the second harmonic signal, at least 50 mW laser beam power has to be used, but only 0.5 mW is enough for the linear measurement. This also has considerable implications for laser safety during experimentation when the beam is transported along the long corridor. Therefore we decided to continue our measurement with field cross correlations.

- **Minimization of the beam divergence**. Beam transport from one room to the other and along the long corridor led to serious losses in intensity due to beam divergence. Therefore to optimize the power collected from the reflected beam from the long measurement arm, two achromatic lenses are used before the beam splitter to minimize the divergence. The reflected beam size is limited by the diffraction by,

$$D = \lambda \cdot L/d \tag{5.5}$$

  where, d is the initial diameter of the pulse and D is the diameter of the beam after propagation of a distance L. For our case where $d = 1$ cm and $L = 100$ m, we have $D = 3$ cm under optimum conditions.

- **Compensation window**. In Fig. 5.4, the beam splitter has a thickness of 1 cm. The group delay dispersion caused by the multiple reflections of the reference arm inside the beam splitter can not be ignored. A compensation window is inserted in the measurement arm to obtain a symmetric autocorrelation at equal arms.

- **Piezo scanning speed**. The piezo for short displacement measurement worked at a linear modulation of 1 Hz. When we use this to measure the length of the long arm, longer than 10 m, we observed that the fringes disintegrated. This is shown in Fig. 5.6. This arises due to the turbulance of air and inherent vibrations of the setup. To determine the source of

this problem, we fixed the mechanical car at 50 m and measured the interference fringes for this distance, for 60 seconds using the HeNe fringe counting laser interferometer. On Fourier transforming the measured fringes. We discovered that most of the turbulance and vibration contribution lie below 50 Hz. This measurement and Fourier transform are shown in Fig. 5.7. Therefore we decided to use a different piezo (Amplified Piezo Actuator APA120ML-PP) which could be scanned at 50 Hz with a sine modulation. Using this we could observe the fringes inside the cross correlations for longer length of the measurement arm.

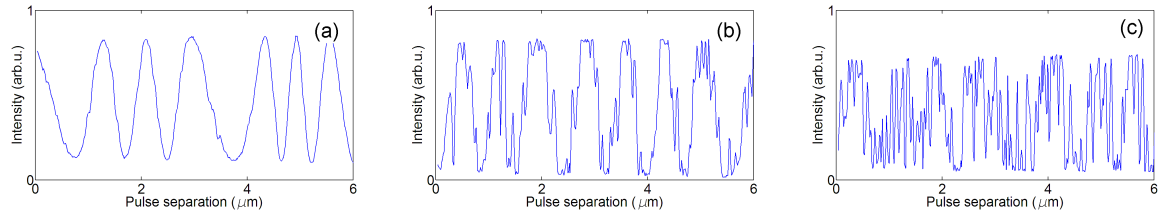

Figure 5.6: Fringes from cross correlations recorded using the old piezo with different path length differences. (a) $6 \times L_{pp}$, (b) $50 \times L_{pp}$, (c) $100 \times L_{pp}$. It can be seen that the fringes disintegrate due to air turbulance and vibration at low frequencies.

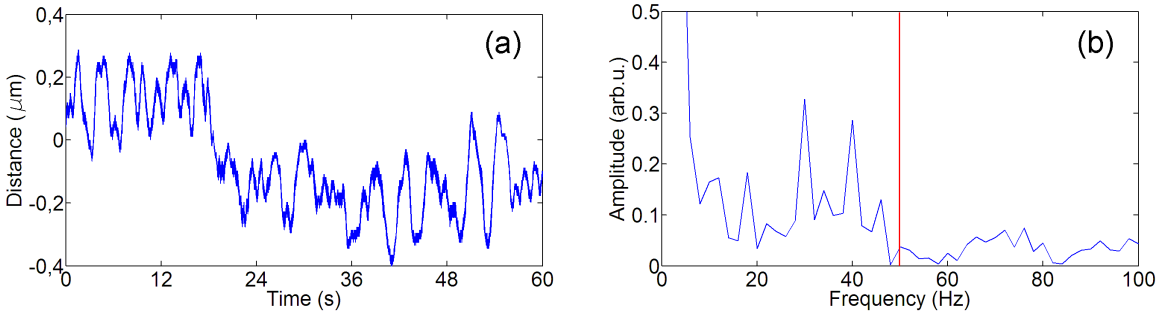

Figure 5.7: (a) Measured interference fringes using the HeNe fringe counting laser interferometer at the path length difference of 100 m. (b) The corresponding frequency analysis. We can see that, most of the turbulance and vibration contribution lie below 50 Hz.

- **New retro-reflector**. For the piezo element which could be scanned at 50 Hz, we needed a much lighter retro-reflector. Therefore we used a new gold coated retro-reflector with a diameter of 0.25 inch and weighing 8 g in total.

- **Piezo Scanning range**. For the short distance, a piezo range of 40 μm was used. For long distance measurements this was not enough since the correlations are broadened through the long propagation in air. The new piezo scan range is 80 μm. Figure. 5.8 shows the cross correlation functions at $L_m = 100$ m. The left one is a field cross correlation with 40 μm linear modulation at 1 Hz with the old piezo. The right is a cross correlation function with 80 μm sine modulation at 50 Hz with the new piezo.

5.3.3 Measurements procedure

The measurement is carried out by first placing the mechanical car with the retro reflector in the long arm at the closest possible position to the dichroic mirror. At this position the path length difference between both arms is 1.8 m, corresponding to 6 times the cavity length. The cross-correlation pattern is located by moving the translation stage in the reference arm and scanning

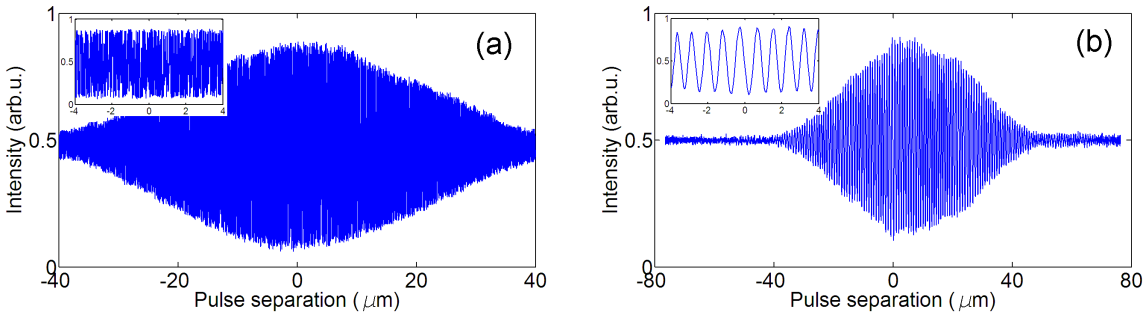

Figure 5.8: The cross correlation functions at L_m = 100 m observed by the old piezo and the new piezo. (a) Field cross correlation with 40 μm linear modulation at 1 Hz using the old piezo. (b) Field cross correlation with 80 μm sine modulation at 50 Hz using the new piezo.

the PZT. This cross correlation is then recorded. Subsequently the mechanical car is moved over a distance of tens of meters (corresponding to a path length change of several hundred L_{pp}), such that another cross correlation pattern is located and recorded. The measured distance ΔL_m has been extracted from the position of the maximum of the cross correlations, which is found by curve fitting the envelope with a Gaussian. Since the displacement can only approximately be set to a multiple of $l_{pp/2}$, the peaks do not appear at exactly the same PZT position. From the relative peak positions of the two cross correlations the correction term δ is obtained. The real displacement is retrieved from,

$$\Delta l_m = m \cdot l_{pp/2} + \delta/2 \tag{5.6}$$

Here to simplify the experiment, we moved the measurement arm in multiples of half cavity length, in order to make the Δl_r in Eq. 5.1 equal zero. This was done only to simplify the measurement procedure. In fact, to measure an arbitrary distance, the reference arm needs to be accurately calibrated. Also, the integer number m in our case is known very accurately using measuring tape, since the ambiguity range for this measurement is 15 cm.

5.3.4 Numerical model for analysis

In case of the measurement of distances larger than 10 m, considerable broadening and chirp is observed in the correlation patterns because of the dispersion of the pulse in air. This makes it quite challenge to determine the center of the cross correlation pattern and thus the distance from the measurements. In chapter 4, we already observed that no single group velocity can be used to determine the maximum of the cross correlation function and hence the path length difference. Group velocity simply defined by Eq. 5.3 is not valid for a pulse with asymmetric PSD propagating in a dispersive medium, in our case, air. Typical laser pulses used in an experiment have sufficient asymmetry for the old definition of v_g to be inapplicable. To calculate the correct distance marked from the maximum of the cross correlations we have to take all the frequencies in the PSD and their propagation using refractive indices which are nonlinear with frequency, into account. To accomplish this, we developed the numerical model described below.

The starting point of our model involved getting an accurate measurement of the PSD of our laser pulses. The spectral content of the pulse was extracted from an autocorrelation measurement at zero path length difference by the Wiener-Kinchine theorem. The autocorrelation is shown in Fig. 5.9-(a), with its Fourier transform the solid curve in Fig. 5.9-(b). This measured PSD has been compared to another independent measurement made with an Ocean Optics spectrometer shown as the dotted curve in Fig. 5.9-(b). The spectrum has a maximum at 815 nm.

	10m	20m	30m	40m	50m
$d_{chirp}(\mu m)$	1.122	1.458	1.512	1.534	1.492

Table 5.2: Different d_{chirp} from path length difference from 0 m to 100 m.

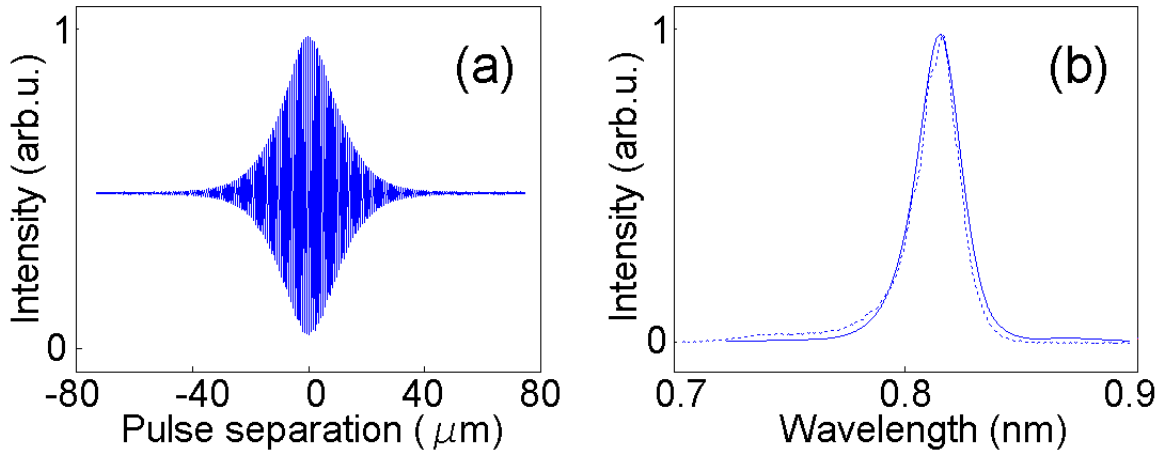

Figure 5.9: (a) Autocorrelation at equal arms. (b) Spectrum derived from the autocorrelation (solid) compared to the spectrum measured using an Ocean Optics spectrometer (dotted).

Using this PSD, the numerical model implemented plane wave propagation at 10^6 individual frequencies, separated by the repetition frequency, using Edlèn's equation. Cross correlations were then calculated using Eq. 4.16. The model takes into account only path length differences and thus, only differences in spectral phase acquired in air. The experimentally measured cross correlations compared to our numerical model are shown in Fig. 5.10. The amplitude of the cross correlation function drops to 30% after 50 m propagation in air in the case of experiments. We can explain this decrease in amplitude by taking into account the divergence of the beam and the fact that only some part of the returning beam is captured by the APD. The envelope of the measured cross correlation functions vary due the turbulance of the air column during the measurement. Overall the experimental and numerical cross correlation patterns show good agreement in width and shape, and will be further compared in the next section.

In chapter 4 section 2, we have seen that, the path length difference at the maximum coherence *i.e.* the peak of the correlation function at different positions, does not exactly overlap with a multiple of L_{pp}, which is calculated using Eq. 5.2 and Eq. 5.3. In this case the λ_0 used is the wavelength at the maximum of the PSD which is asymmetric. For path length differences up to 100 m the value varies from 1 μm to 1.6 μm as shown in Table.5.2. In order to take this deviation arising due to dispersion into account, a correction term d_{chirp} has to be added to Eq. 5.6 and the measured distance is given by,

$$\Delta l_m = m \cdot l_{pp/2} + d_{chirp}/2 + \delta/2 \tag{5.7}$$

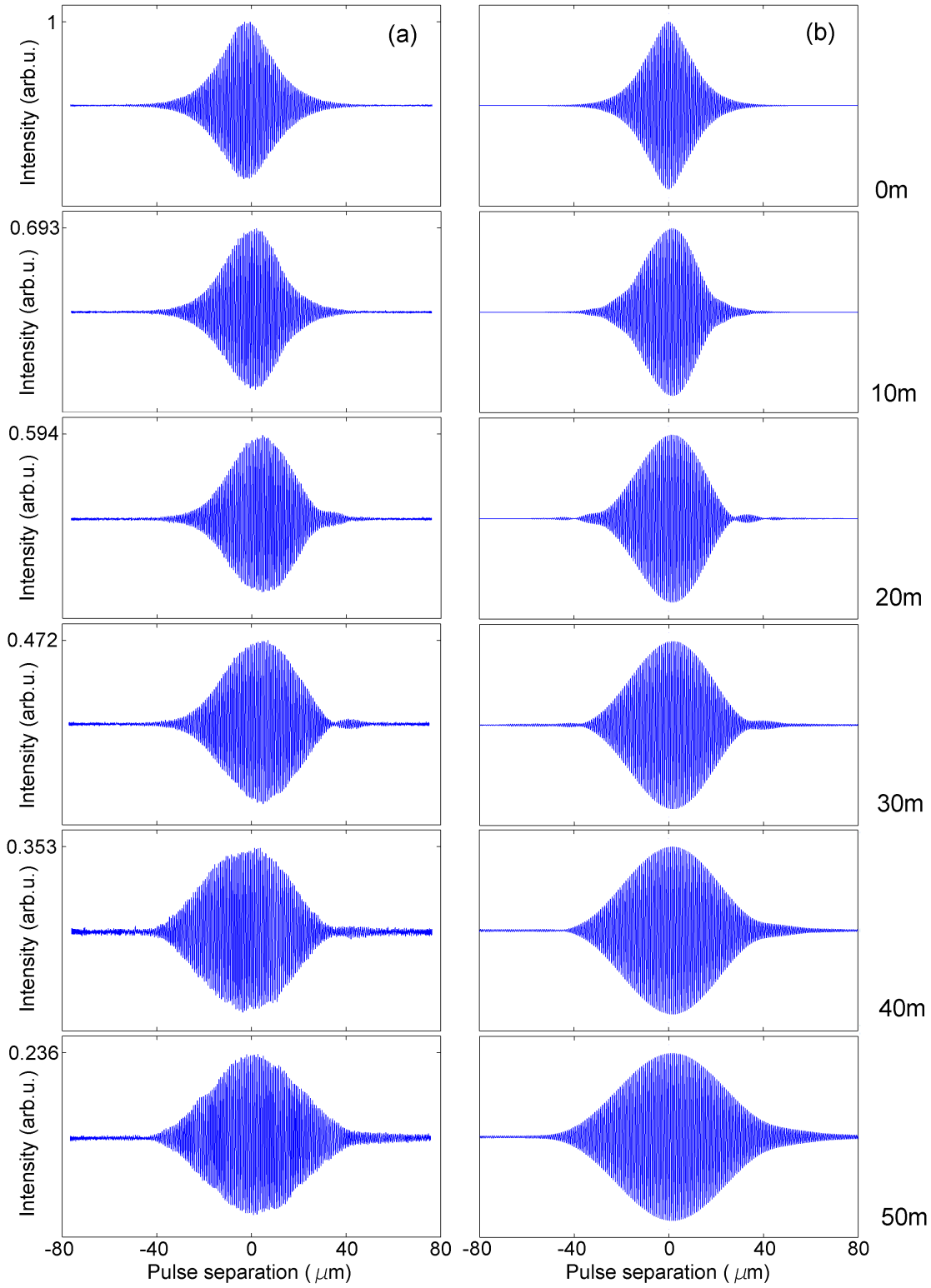

Figure 5.10: Cross correlations at different path length differences ranging from 0 m to 100 m. (a) Measured cross correlations. For each panel, the y-axis shows the maximum of the intensity, the scale begins at zero. (b) Corresponding normalized cross correlations calculated using the numerical model.

5.3.5 Cross correlations up to 200 m propagation in air

We recorded cross correlation patterns for a path length difference of 200 m by folding the beam using another retro-reflector. This was done to study the evolution of the cross correlation with distance for longer path length differences. In Fig. 5.11 we show the comparison between the experiment and the simulation results from path length differences ranging from 120 m to 200 m.

In general, the shapes of the cross correlations show good agreement with the simulated patterns. Simulated and measured patterns both show similar chirp and broadening. It can be seen that the numerical model can account for the effect of non-linear dispersion due to propagation in air for pulses which have an asymmetric PSD. To study the broadening, full width at half maximum of measured and simulated correlation patterns are given in Fig. 5.12-(a). The comparison is done for 0 up to 200 m propagation in air. The differences mainly arise due to the unpredictable effects of vibrations in the interferometer and air turbulence in the measurement room.

To study the chirp, we again compared measurements to simulations. For this, let us consider R_{HW} to be the half-width on the right of the full-width at half maximum and L_{HW} to be the left half width at the full width at half maximum. We define the chirp ratio as follows

$$\text{chirp ratio} = \frac{R_{HW}}{L_{HW}} \tag{5.8}$$

This chirp ration extracted from Eq. 5.8 using both the measured and simulated patterns are shown in Fig. 5.12-(b), for path length differences ranging from 0 m to 200 m in air. From our simulations we note that the chirp reaches its maximum at a path length difference of ~ 40 m. After 40 m, this ratio follows an exponential decay and tends asymptotically to a constant value for large delays ($> 150\ m$) [67]. Here again the differences mainly arise due to the unpredictable effects of vibrations in the interferometer and air turbulence in the measurement room.

5.3.6 Measurement results

The fluctuation of the temperature in the laboratory was controlled to be less than 0.1 °C. During the measurement, pressure and humidity have been monitored with an accuracy of 1 hPa and 1% respectively. Here again the uncertainty of the measurement done using the He-Ne laser was dominated by the 40 cm dead path length and is estimated to be around 50 nm as specified in the manual. Figure. 5.13 shows the results obtained as compared to the fringe counting wavelength calibrated He-Ne laser. Each data point has been averaged from 6 independent measurements for both lasers. For each of these measurement, we averaged over 5 correlation patterns. From the figure, it can be seen that the measurements using the frequency comb laser agree with the reference measurement done with the He-Ne laser within 2 μm [69].

As discussed earlier in chapter 2, the variation and uncertainty on the measurement of these environmental parameters, limits the accuracy in measuring the absolute distance. For example, a typical uncertainty of 0.2°C in temperature and 0.5 hPa in pressure already leads to an uncertainty of the refractive index of air of about 5×10^{-7}, which corresponds to 25 μm at 50 m. Moreover the updated Edlï£¡n's equation itself has an intrinsic uncertainty of 1×10^{-8}, implying 1 μm over a path length difference of 100 m. The influences of the environmental parameters on the refractive index at the wavelengths of both the He-Ne laser and the frequency comb cancel in first order. For this is the reason the agreement between the experimental results is much better than 25 μm. We attribute

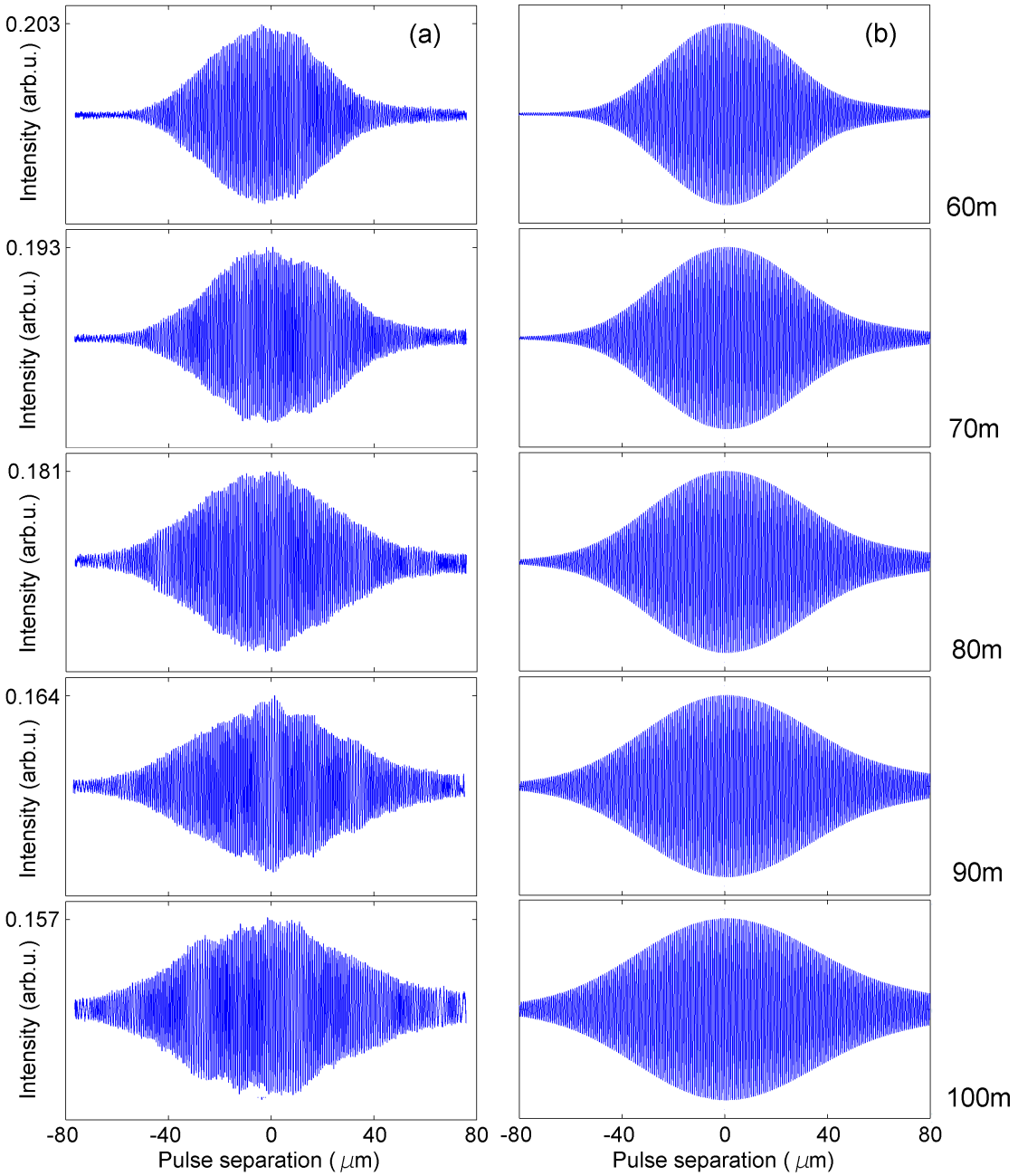

Figure 5.11: Cross correlations at different path length differences ranging from 120 m to 200 m. (a) Measured cross correlations. For each panel, the y-axis shows the maximum of the intensity, the scale begins at zero. (b) Corresponding normalized cross correlations calculated using the numerical model.

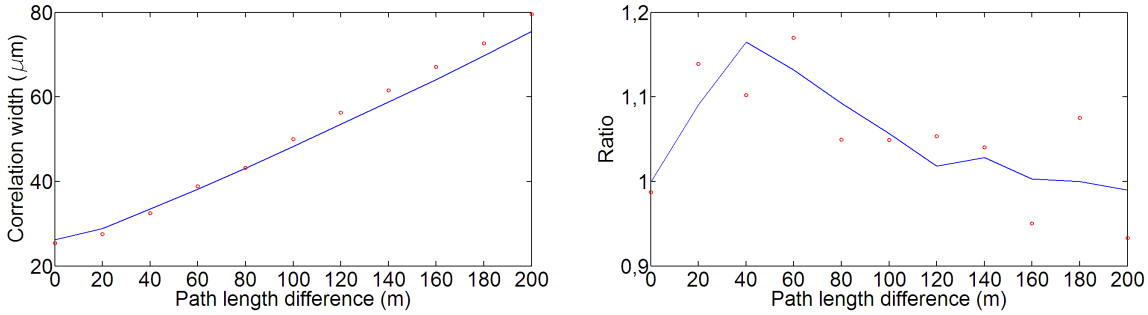

Figure 5.12: The relation between the path length difference and the properties of the cross correlation for the pulses in the experiments. (a) The widths of the cross correlations as a function of the path length difference. (b) The chirp ratio of the cross correlations as a function of the path length difference. In each case, the dots indicate measurement results and the continuous line was obtained from the simulations.

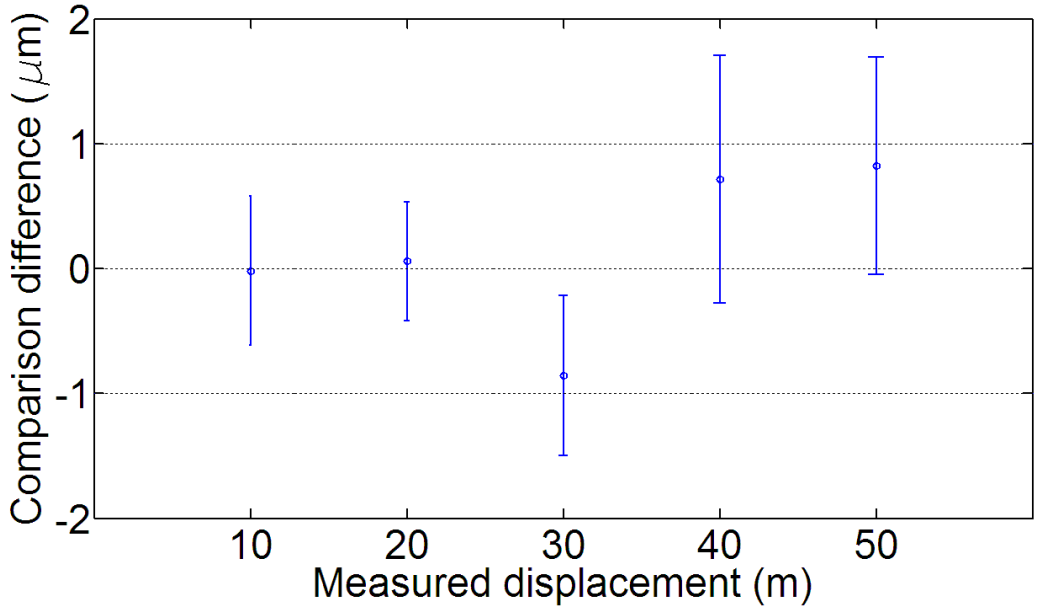

Figure 5.13: Measurement of displacements, of the measurement arm ranging from 10 m to 50 m. The error bars indicate the standard uncertainty, derived from measurement reproducibility.

the residual difference and uncertainty in the comparison measurement to vibrations of the setup and air turbulence. The agreement between the frequency comb and the He-Ne laser is much better than the achievable absolute accuracy in air, showing that the measurement result is not limited by the method chosen.

Chapter 6

Distance measurement in frequency domain

6.1 Spectral interferograms in an unbalanced Michelson interferometer

In chapter 5, we demonstrated that, cross correlation functions from an unbalanced Michelson interferometer can be used to measure the path length difference and hence absolute distances or displacements. Similar measurements can also be done in the frequency domain using spectral interferogram. In this chapter we will describe experiments demonstrating this idea. The experimental setup is very similar to the one where we measured cross correlations, except that we replace the detector with a spectrometer, as can be seen in Fig. 6.1. The physical principle of this has been described earlier in chapter 4, section 3. In this case, the frequency comb laser is used the same way as a white-light source but with much longer coherence length. Suppose the intensities of the reflected beams from the two arms are equal and the absorption of air can be ignored, the spectrum of the interfering beams from both arms is described by,

$$S(\omega) = 2|\hat{E}(\omega)|^2 \left[1 + \cos\left(\varphi_r(\omega) - \varphi_m(\omega)\right)\right] \tag{6.1}$$

Where $\hat{E}(\omega)$ is the spectral amplitude of the pulses, and the distance information is within the interference term,

$$\varphi(\omega) = \varphi_r(\omega) - \varphi_m(\omega) = n(\omega)\omega L/c \tag{6.2}$$

with $n(\omega)$ and c being the refractive index of air and the speed of light in vacuum, respectively. The distance L is the pulse separation from both arms as seen on the spectrometer.

In Fig. 6.1, in order to measure an arbitrary distance, the reference arm needs to be translated and measured with high accuracy. If the resolution of the spectrometer is high enough, the reference arm does not need to move and fringes can always be observed in a spectral interferogram. In practice if the spectrometer has a resolution around 0.01 nm, the fringes become hard to distinguish when the distance between the interfered pulses is more than 10 mm. This distance is much shorter than the inter-pulse distance for a typical femtosecond laser. Instead of moving the reference arm, there are other solutions for this problem. For example, in 2006, Joo and coworkers suggested the use of an Fabry-Perot Etalon (FPE) before the spectrometer [56]. This filtered the frequencies of the pulse and reduced the equivalent inter-pulse distance to 2 mm.

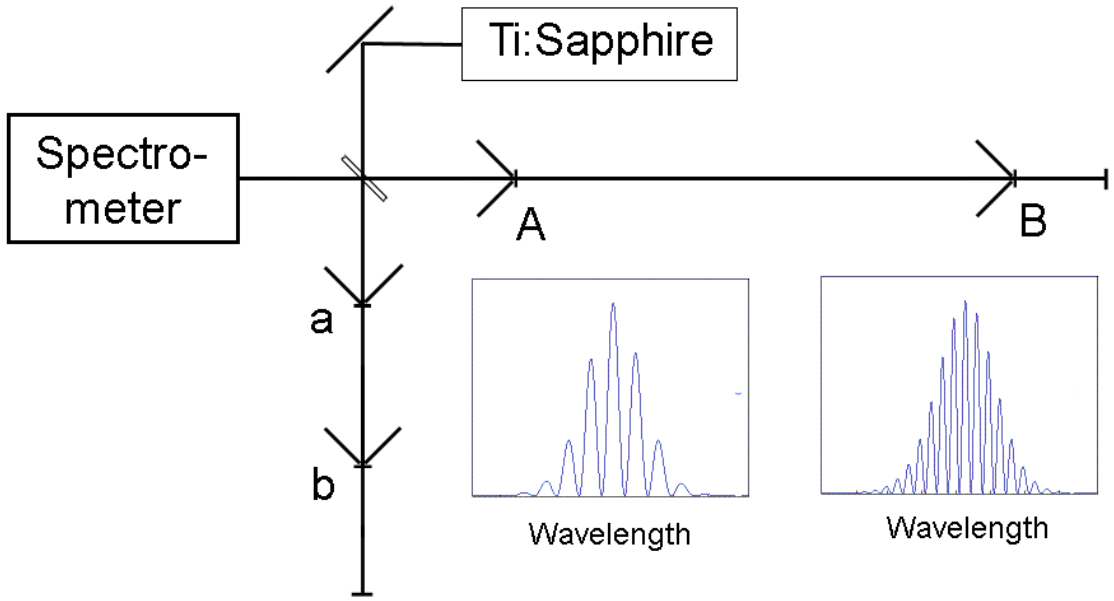

Figure 6.1: The schematic of a typical experimental setup for distance measurement using spectral interferograms

6.2 Measurement of short distances with spectral interferograms

6.2.1 Experimental setup and measurement principle

We began first by building a setup for measuring a short displacement ($l_{pp/2}$) and again comparing the results with a fringe counting laser interferometer. For a short distance, the group delay dispersion of air was ignored. Figure. 6.2 is a schematic of the optical configuration of our setup. The laser source is still the same as we used in chapter 5, section 2. The pulses from the laser are split into two at the beam splitter. One part of the pulse goes into the non-varying reference arm of the interferometer with length l_r and is reflected by a hollow gold coated retro-reflector. The other part of the pulse goes into the measurement arm with length l_m. The length of this arm can be varied with a translation stage (PI M series 15 cm translation range). Another gold coated retro-reflector was mounted on top of the translation stage. The two reflected beams coincide with each other and are focused onto an uncalibrated grating spectrometer. This spectrometer is made by a single slit, two lenses, one grating and a line CCD (Thorlab) with 3000 pixels as shown in Fig. 6.2.

Once the intensity of the spectral interference pattern containing the phase information is recorded, a Fourier filter was used to reconstruct the distance information [56, 70, 71]. The dispersed interference intensity captured by the line CCD is Fourier transformed and shown Fig. 6.3-(a) to Fig. 6.3-(b). The DC peak is only the power spectral density and contains no phase information. One of the AC peaks is band-pass filtered and inverse Fourier transformed. The phase of the inverse Fourier transform is extracted and from this the unwrapped phase is obtained as shown in Fig. 6.3-(e). Then the distance can be calculated from the derivative of the unwrapped phase,

$$L(\omega) = \frac{c}{n_g(\omega)}\left(\frac{d\varphi}{d\omega}\right) \qquad L(\lambda) = -\frac{\lambda^2}{2\pi n_g(\lambda)}\frac{d\varphi}{d\lambda}. \tag{6.3}$$

Here λ is the wavelength and n_g is the group refractive index of air. For an unchirped spectral interferogram, L tends to a constant value as shown in Fig. 6.3-(f). In the above equation, $d\varphi/d\omega$ and

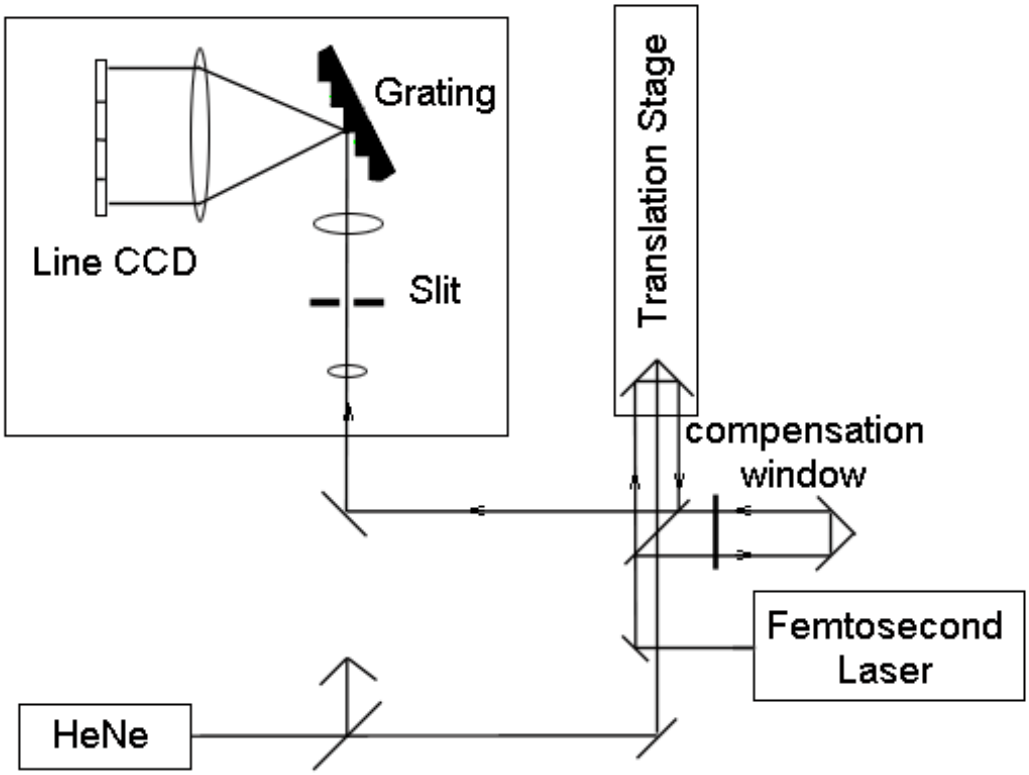

Figure 6.2: Schematic of the experimental setup used to measure a short distance using spectral interferograms. A pulse train is sent into an interferometer and spectral interferograms are measured at two positions of the translation stage, separated by a distance $l_{pp/2}$. Simultaneously, the displacement is measured with a Zeeman-stabilized HeNe fringe counting laser interferometer.

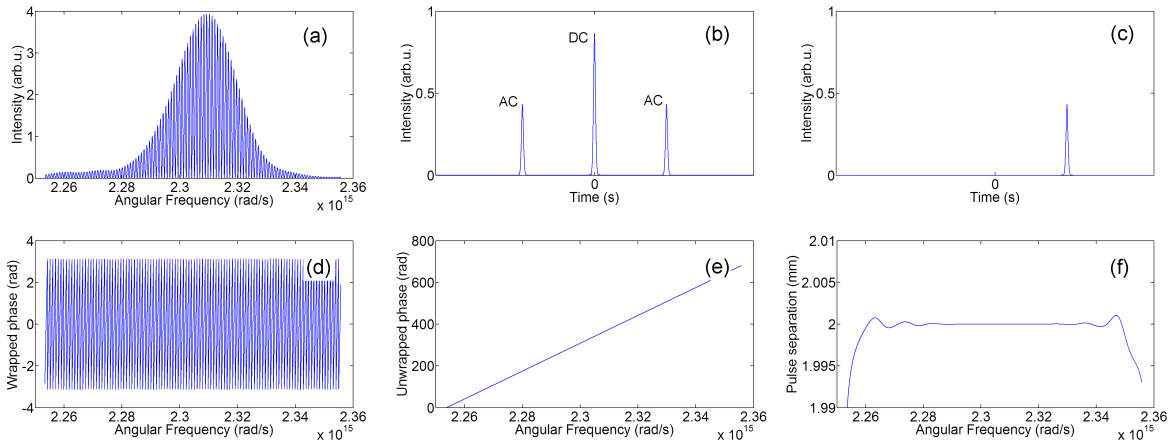

Figure 6.3: Data processing procedure for measurement of L. (a) The spectral interferogram *i.e.* dispersed interference intensity captured by the CCD line. (b) Fourier transform of the measured spectral interferogram. (c) The DC peak and one AC peak are band pass filtered. (d) The wrapped phase. (e) The unwrapped phase. (f) The pulse separation obtained from the derivative of the unwrapped phase.

$d\varphi/d\lambda$ are the derivatives of the unwrapped phase, with respect to circular frequency and wavelength respectively. In order to minimize the uncertainties introduced by Fast Fourier Transform, a zero-padding process and if necessary, a filtering window have to be used to get the best reconstruction.

In Fig. 6.4 we show the interfered spectra at different pulse separations. When the translation stage is set to the front such that the distances between the two arms are nearly equal, a modulated spectrum shown in Fig. 6.4-(a) is observed. Due to the cosine term in Eq. 6.1, the spectrum is un-distinguishable from its twin image with the same pulse separation but an opposite sign. This "'twin image"' problem can be solved by moving one arm a little bit and observing how the spectrum changes. When the separation between the two pulses becomes larger, more fringes appear in the spectrum. When the number of fringes is beyond the resolution of the spectrometer, as shown in Fig. 6.4-(b), the modulation depth becomes shallower. The fringes disappear when the distance between the two arms is larger than 20 mm, but they appear again as the translation stage moves around half of the inter-pulse distance (15 cm) because one pulse is interfering with the next, as shown in Fig. 6.4-(c). As the translation stage moves further backward, this phenomenon re-appears periodically. For this measurement, $l_{pp/2}$ can be viewed as the synthetic wavelength. Spatial overlap between the pulses can always be accomplished when the displacement of the measurement arm is around a multiple of the half inter-pulse distance,

$$\Delta l_m = m \cdot l_{pp/2} + L_A/2 - L_B/2. \tag{6.4}$$

Here m is an integer and $l_{pp/2}$ is half of the inter-pulse distance, calculated by $l_{pp/2} = v_g/(2f_r)$. The group velocity of the frequency at the center of the PSD is v_g and f_r is the repetition frequency. Δl_m is the total displacement of the measurement arm. Each spectral interferogram consists of the interference between two pulses which are slightly separated from each other. The pulse separation in the front of the translation stage is L_A and L_B is the pulse separation at the back of the translation stage, calculated by Eq. 6.3. In both cases, the sign of L_A and L_B are defined positive when the pulse from the measurement arm is ahead of the pulse from the reference arm. The factor of two comes from the back and forth propagation. If f_r is locked and stabilized, the absolute uncertainty of this method should not increase due to increasing the integer number m. This indicates that the maximum distance that can be measured by this technique is only limited by the coherence length

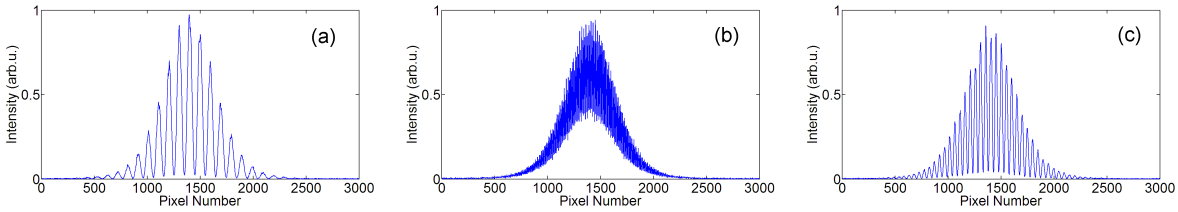

Figure 6.4: Spectral interferograms recorded for different pulse separations. (a) Two pulses at ±0.6 mm separation. (b) Two pulses at ±6mm separation. (c) After one cavity length, the fringes re-appear, where the pulse separation now is ±1.2 mm.

of the laser source, allowing for a low relative uncertainty at long distance. In this section, we only verified a short displacement of $m = 1$. Distance measurements as long as 50 m will be given in the next section.

6.2.2 A new calibration approach

The calibration of the grating spectrometer plays an important role when using this method for distance measurement. First, what is measured from the grating spectrometer is the modulated spectra, with respect to the wavelength instead of the frequency. Only when the spectrum is narrow can we use λ_c^2 to approximate λ^2 in Eq. 6.3, where λ_c is the wavelength at the maximum of the PSD. Normally it is necessary to convert the x-axis from wavelength to frequency and this conversion decreases the resolution. Secondly for a typical grating spectrometer, the read out of the line CCD is not necessarily linear to the wavelength. The spectrometer is normally calibrated as a quadratic function of the wavelength. Thirdly, although the grating spectrometer can be calibrated accurately, the wavelength calibration also drifts slightly in time due to varying environmental conditions [72]. In our experiment, instead of calibrating the grating spectrometer itself, we measure a short displacement accurately (<1 mm) and use this distance as a reference to measure the unknown distance. In this case, the calibration parameters cancel, but the ratio between the two distances can be calculated from the unwrapped spectral phases obtained from the spectrometer.

First, we need to measure a short calibrated displacement. This is down as follows: We first scan the measurement arm to make it approximately, but not exactly, equal to the reference arm and label this position as "C1". In Fig. 6.5-(a) we show the measured interferogram when the measurement arm is located at position "C1". In Fig. 6.5-(b) we show the derivative of the unwrapped phase $d\varphi_{c1}/dx$ obtained from the interferogram in Fig. 6.5-(a), with respect to the pixel number x. The deviation on both sides of the curve shown in Fig. 6.5-(b) comes from the aliasing of the Fourier transform and can be ignored. Next, the measurement arm is displaced a short distance to position "C2". This displacement is labeled as Δl_c and is simultaneously measured by a traditional counting laser with an accuracy of 10 nm. The interferogram measured at "C2" is shown in Fig. 6.5-(c) and the derivative of the unwrapped phase $d\varphi_{c2}/dx$ is calculated and shown in Fig. 6.5-(d). The exact pulse separations at "C1" and "C2" are not known because the grating spectrometer is not calibrated, but the displacement Δl_c is linked to the difference of Fig. 6.5-(b) and Fig. 6.5-(d), or in other words, $d\varphi_{c1}/dx - d\varphi_{c2}/dx$.

If we assume that the relation between the pixel number x of the CCD line camera and the circular frequency ω follows a nonlinear relation,

$$x = \Omega(\omega) \tag{6.5}$$

where x spans from 1 to 3000 pixels. When we substitute Eq. 6.5 into Eq. 6.3, we get

$$L = \frac{c}{n_g}\frac{d\varphi}{dx}\Omega^{'}(\omega) \tag{6.6}$$

where $\Omega^{'}(\omega)$ is the derivative with respect to ω. If we measure a calibrated short displacement Δl_c at approximately equal arms, we get the calibration function related to the distance,

$$2\Delta l_c = \frac{c}{n_{gc}}\left(\frac{d\varphi_{1c}}{dx}\Omega^{'}(\omega) - \frac{d\varphi_{2c}}{dx}\Omega^{'}(\omega)\right) \tag{6.7}$$

Where $d\varphi_{1c}/dx$ and $d\varphi_{2c}/dx$ are the derivatives calculated from the unwrapped phase of the modulated spectra as described earlier. n_{gc} is the group refractive index of the wavelength at the maxiumum of the PSD, measured at the time of the calibration measurement. Now if a displacement of L is as shown in Eq. 6.6 is to be measured, it is related to the calibration equation Eq. 6.7 by,

$$\frac{L}{2\Delta l_c} = \frac{n_{gc}}{n_g}\frac{d\varphi}{dx}\Big/\left(\frac{d\varphi_{1c}}{dx} - \frac{d\varphi_{2c}}{dx}\right). \tag{6.8}$$

We observe that the calibration function $x = \Omega(\omega)$ has canceled out. The derivative of the measured (unknown) unwrapped phase is $d\varphi/dx$, and n_g is the group refractive index of the wavelength at the maxiumum of the PSD, at the time of the distance measurement. In the special case when the spectral width $d\lambda$ is much less than λ in Eq. 6.3 and the read out x has a linear relation to λ, $x = \Omega(\omega)$ becomes a linear function. But we would like to emphasize that Eq. 6.8 is also valid for an arbitrary relation between x and ω.

6.2.3 Measurement procedure

When the measured interferograms are not chirped, the derivative of the unwrapped phase is expected to be a constant, as shown in Fig. 6.3-(f). In absence of an absolute calibration of the spectrometer, that is an unknown relationship between the pixel number "x" on the line CCD and frequency, even without chirp, the $d\varphi/dx$ respect to x is not a constant because the relation between x and ω is not necessarily linear.

In the actual experiment, the measurement arm was moved approximately half cavity length from position A to B as illustrated before in Fig. 6.1. The modulated spectra at both A and B are recorded and the derivatives of the unwrapped phases are obtained. If the environmental conditions at the calibration and actual distance measurements are approximately equal, from Eq. 6.8, we get,

$$L_A = 2\Delta l_c \cdot \frac{d\varphi_A}{dx}\Big/\left(\frac{d\varphi_{1c}}{dx} - \frac{d\varphi_{2c}}{dx}\right) \qquad L_B = 2\Delta l_c \cdot \frac{d\varphi_B}{dx}\Big/\left(\frac{d\varphi_{1c}}{dx} - \frac{d\varphi_{2c}}{dx}\right). \tag{6.9}$$

In Fig. 6.6-(a) and (b) we show the interferogram recorded at A and the derivative of the unwrapped phase respectively. In Fig. 6.6-(c) we show the distance L_A extracted using Eq. 6.9. The nonlinear relation between the pixel number and the frequency shown in Eq. 6.5 canceled out in Eq. 6.9. Therefore we can see almost a constant L_A most frequencies in the center of Fig. 6.6-(c). The aliasing caused by the Fourier transform does not canceled, so both sides of Fig. 6.6-(c) show deviation. A constant L_A for all pixel numbers indicates that the spectral inteferogram is not chirped with respect to ω. A similar process happens at position B and the respective interferogram, derivative of the unwrapped phase and calculated L_B are shown in Fig. 6.6-(d),(e),(f) respectively. Since half a cavity length is a small distance, we can see that Fig. 6.6-(f) still shows a fairly constant L_B.

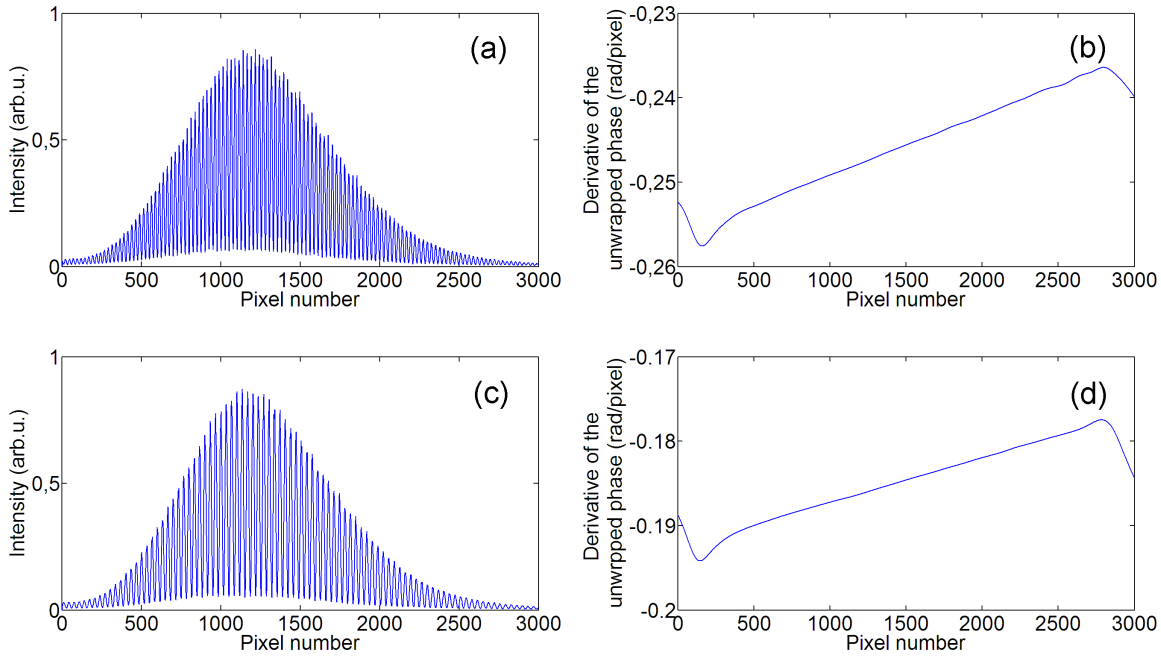

Figure 6.5: The spectral interferograms and the derivatives of the unwrapped phases at position C1 and C2 in the calibration measurement. (a) The measured interferogram when the measurement arm is located at position "C1". (b) The derivative of the unwrapped phase $d\varphi_{c1}/dx$ obtained from the interferogram in (a), with respect to the pixel number x. The deviation on both sides of the curve shown in Fig. 6.5-(b) comes from the aliasing of the Fourier transform and can be ignored. (c) The measured interferogram when the measurement arm is located at position "C2". (d) The derivative of the unwrapped phase $d\varphi_{c2}/dx$ obtained from the interferogram in (c), with respect to the pixel number x.

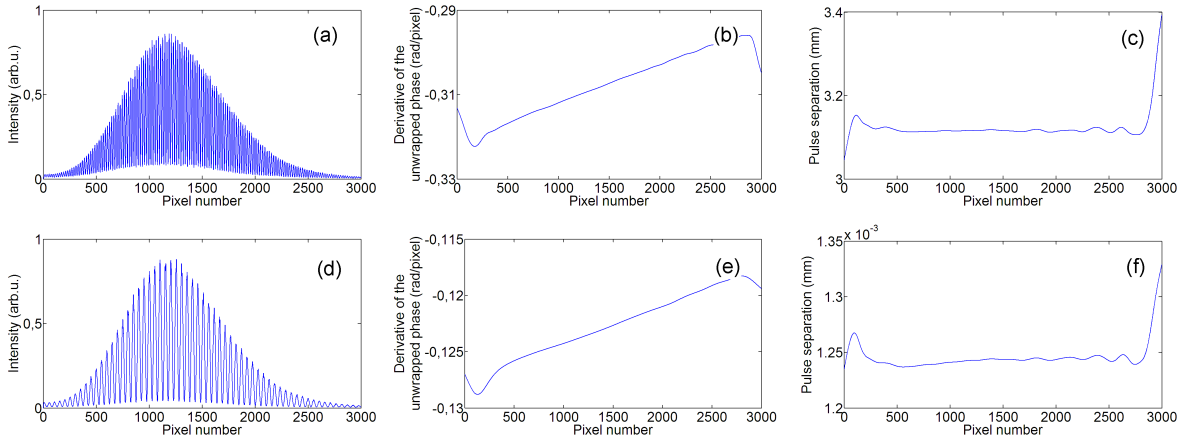

Figure 6.6: The spectral interferograms, the derivatives of the unwrapped phases and the derived pulse separations at postion A and B in the distance measurement. (a) The interferogram recorded at A. (b) The derivative of the unwrapped phase at A. (c) The distance L_A extracted using Eq. 6.9. (d) The interferogram recorded at B. (e) The derivative of the unwrapped phase at B. (f) The distance L_B extracted using Eq. 6.9.

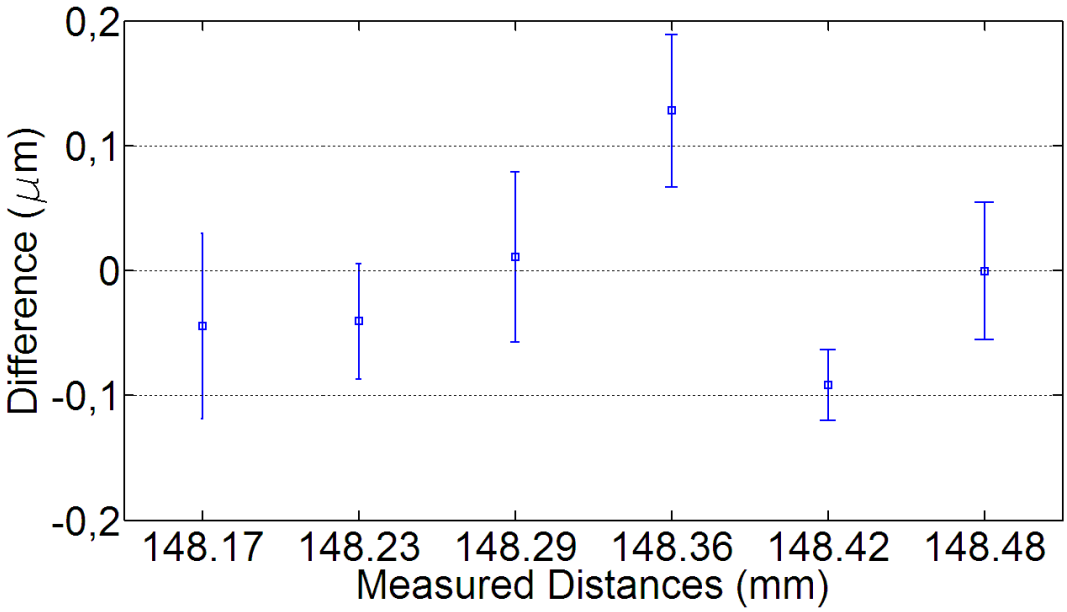

Figure 6.7: Experimental results of comparison measurement of 6 difference distances. The error bars indicate the standard uncertainty, derived from measurement reproducibility. The agreements are within 200 nm and the standard deviation of each measurement is less than 100 nm.

From these measurements, using Eq. 6.4 and Eq. 6.9 we can calculate the measured distance as,

$$\Delta l = \frac{\frac{d\varphi_A}{dx} - \frac{d\varphi_B}{dx}}{\frac{d\varphi_{c1}}{dx} - \frac{d\varphi_{c2}}{dx}} \cdot \Delta l_c + l_{pp/2} \tag{6.10}$$

where $m = 1$.

6.2.4 Measurement results

At first the translation stage was displaced from approximately 1.2 mm pulse separation (L_{c1}=1.2 mm) to about 0.6 mm pulse separation (L_{c2}=0.6 mm). The displacement was recorded by a traditional counting laser with an accuracy of about 10 nm. The calibration measurement is repeated 6 times and the average value of $d\varphi_{1c}/dx - d\varphi_{2c}/dx$ was used. Then the actual comparison experiment was carried out by measuring 6 different distances, all close to a distance of 15 cm, which is approximately the half laser cavity length. All comparison measurements start at 1.2 mm pulse separation at position A (L_A=1.2 mm), and span equally distances from 0.6 mm to 1.2 mm separation, for several position of B ($L_B = 0.6, 0.72, 0.84, 0.96, 1.08, 1.2$ mm) and each measurement consists of 5 interferograms recorded in the front and 5 interferograms at the back of the translation stage. The temperature and pressure are stabilized within 0.1 °C and 1 hPa. The measured distances are compared to a fringe counting laser interferometer. The results of the comparison are shown in Fig. 6.7 with the error bars indicating the standard deviation of our measurement.

6.2.5 Resolution of the the grating spectrometer

It is important that the spectrometer has good resolution to give the correct ratio between the reference distance Δl_c and the measured distances $L_A/2$ and $L_B/2$. The resolution of the grating spectrometer is determined by several factors, which we discuss below [73].

- **Grating resolution**. The limit of the grating resolution is determined by,

$$\lambda/d\lambda = N \cdot p \tag{6.11}$$

  Here N is the totally number of grooves used on the grating and p is the order number and in our experiments it is 1. We use a grating with groove density 1200 lines/mm, 50 mm total width. If we suppose that 70% of the grating surface is used, the grating resolution is $\delta\lambda_g$ = 0.02 nm.

- **Lateral dispersion**. The lateral dispersion is a measure of how different wavelengths are laterally displaced in the exit focal plane. It is calculated by,

$$d\lambda/dx = g \cdot \cos\beta / f \tag{6.12}$$

  where g is the groove size, β is the diffraction angle, dx is the length of one single pixel on the line CCD camera and f is the focal length of the lens behind the grating. In our experiment, we try to use all pixels of the CCD camera to obtain almost the maximum dispersion possible. The CCD camera consists by 3000 pixels in a line with 25 mm length. This limits the resolution due to lateral dispersion to $\delta\lambda_c = 0.011$ nm.

- **Slit size**. The slit size determines the bandwidth of a single input wavelength. Only two signals with their frequency difference more than the bandwidth can be distinguished by the spectrometer. This leads to a limit on the resolution due to the finite size of the slit width given by,

$$\delta\lambda_s = \frac{g}{f} \cdot \cos\beta \cdot \Delta x \tag{6.13}$$

  In our experiments, the slit size is around 20 μm. This gives a resolution of $\delta\lambda_s = 0.026$ nm because of the slit size.

The total resolution of the spectrometer in terms of wavelength,

$$\delta\lambda = \sqrt{\delta\lambda_g^2 + \delta\lambda_c^2 + \delta\lambda_s^2} = 0.035 \text{ nm} \tag{6.14}$$

The resolution of the spectrometer plays a key role in our measurement accuracy. In Fig. 6.8 we show the modulated spectra at pulse separation of 2 mm. The resolution of the spectrometer is 0.05 nm in Fig. 6.8-(a), 0.1 nm in Fig. 6.8-(b) and 0.2 nm in Fig. 6.8-(c) respectively. When the distance between the interfered pulses is fixed, a higher resolution means deeper modulation.

6.2.6 Influence of the grating spectrometer resolution on distance measurement

To estimate the uncertainty in the measured distance, arising due to the finite resolution of the grating spectrometer, let us assume that φ and λ have a linear relation. We illustrate this in Fig. 6.9.

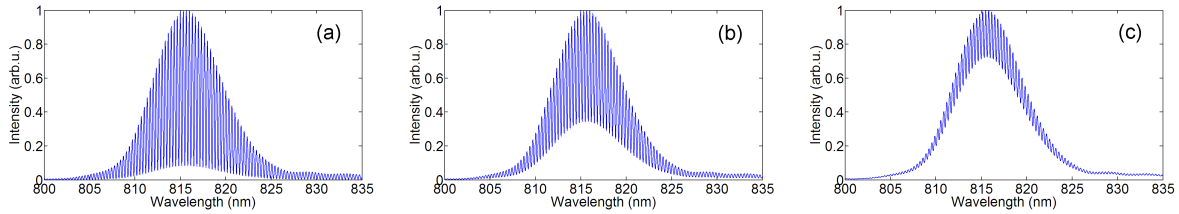

Figure 6.8: Simulated spectral interferograms arising from the interference of two pulses separated by 2 mm shown using spectrometer having resolutions of (a) 0.05 nm, (b) 0.1 nm and (c) 0.2 nm respectively.

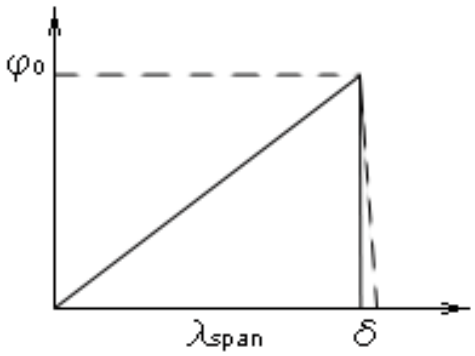

Figure 6.9: Illustration of the uncertainty caused by the influence of the grating spectrometer resolution on distance measurement

From Eq. 6.3, we can see that the distance between the two interfering pulse is proportional to φ_0/λ_{span}. Here we call the total range of the spectrometer λ_{span}, and φ_0 is the maximum of the wrapped phase. Because of the finite resolution, what we actually measure is proportional to $\varphi_0/(\lambda_{span}\pm\delta\lambda)$. The uncertainty due to this in the measurement is given by,

$$\frac{\delta L}{L} = \frac{L^{'} - L}{L} = \frac{\frac{\varphi_0}{\lambda_{span}\pm\delta\lambda} - \frac{\varphi_0}{\lambda_{span}}}{\frac{\varphi_0}{\lambda_{span}}} \approx \pm\frac{\delta\lambda}{\lambda_{span}} \tag{6.15}$$

In our experimental setup, $\lambda_{span} = 35$ nm and $\delta\lambda = 0.035$ nm. This leads to $\frac{\delta L}{L}$ equal to 10^{-3} in our case.

It should be mentioned that, δL will effect both the reference measurement and the comparison measurement. For the first order approximation, if suppose that the dependence between the pixel number and the wavelength is a linear function, from Eq. 6.10, we see that, the uncertainty of the measurement depends on $d\varphi_{1c}/d\lambda$, $d\varphi_{2c}/d\lambda$, $d\varphi_F/d\lambda$ and $d\varphi_B/d\lambda$. Beside the resolution of the grating spectrometer, the fluctuation of air, the vibration of the setup and the resolution of the Fast Fourier Transform also contribute to the uncertainty of the measurement. Our experimental result of 200 nm accuracy is beyond the resolution limit of the grating spectrometer, mainly because we derived the result by averaging five interferograms.

6.3 Measurement of long distances with spectral interferograms

6.3.1 Experimental setup and measurement procedure

A schematic of the experimental setup is shown in Fig. 6.10. As can be seen from the figure, this setup was also located in two adjacent rooms mentioned before in chapter 5. In comparison to the setup for similar measurements done using cross correlations shown in Fig. 5.4, now, the piezo element in the reference arm was removed. The combined beam of the interferometer is incident on the grating spectrometer. The grating spectrometer consists of a slit, a diffraction grating, 2 achromatic lenses and a line CCD with 3000 pixels. Here, we will point out some significant changes to the new setup as compared to the setup for distance measurement using cross correlations.

- In the cross correlation setup, the beam was transported from one room to the other by 4 mirrors and a hole on the wall. In the new setup, we used a fiber to tranport the beam as seen in Fig. 6.10. We verified that the PSD was not significantly changed due to the fiber. One advantage of this modification was that, the output beam profile from the fiber had a very good spatial distribution. At the same time, the two achromatic lenses used to minimize the beam divergence were moved to the long corridor.

- We added a third gold coated retro reflector on a small translation stage (TS1) at the beginning of the long arm of the interferometer in the measurement corridor. A second HeNe fringe counting interferometer was also added to the setup. These additions were made to enable the calibration measurements.

The calibration measurement was performed for equal arms of the interferometer. For this, the third retro reflector mounted on a small translation stage (TS1) at the beginning of the measurement arm was used. At the time of the calibration measurement, TS1 is moved into the beam path

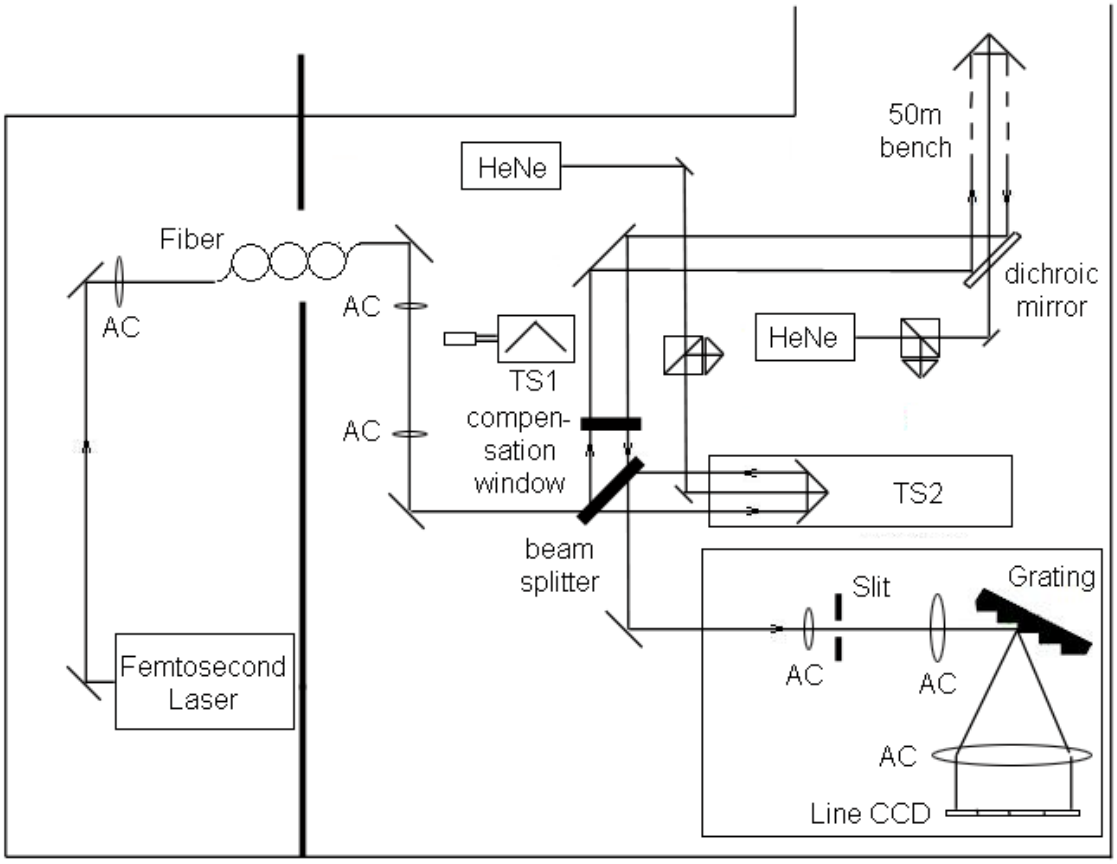

Figure 6.10: Schematic of the experimental setup used to measure distances in the 50 m corridor using spectral interferograms. We can see that the experiment was located in two adjacent rooms. The Ti:Sapphire laser based frequency comb was located in the room on the left. The beam was transported through a hole on the wall to the interferometer in the long corridor using a fiber. The reference arm consists of a hollow corner cube mounted on the translation stage (TS2). The measurement arm consists of two dispersion compensated mirrors and a gold coated retroreflector mounted on a mechanical stage of the 50 m long measurement bench. The HeNe fringe counting laser interferometer was used for a simultaneous comparison measurement. The returning beams were overlapped and focused on a grating spectrometer. A third gold coated retro reflector on a small translation stage (TS1) was added at the beginning of the long arm of the interferometer. A second HeNe fringe counting interferometer was also added to the setup to enable the calibration measurements.

and forms a short interferometer with the translation stage on the reference arm (TS2) as can be seen from Fig. 6.10. The calibration measurement is performed by moving the reference arm (TS2) in a small amount around 1 mm and recording the modulated spectra on the CCD line camera. A second HeNe fringe counting laser interferometer is used to measure the reference arm independently. After the calibration, the retroreflector on TS1 is moved out of the measurement arm. The calibration measurement was repeated several times and the averaged value was used for the long distance measurement.

After the calibration, we translate the retro reflector mounted on TS1 out of the measurement arm. Now the beam is directed to the 50 m bench using two mirrors. One of the mirrors is coated for high reflectivity for 820 nm and high transmission at 633 nm. This was done so that the HeNe fringe counting laser interferometer could be used for a comparison measurement at the same time. A compensation window is used in the long arm to compensate the dispersion of the plate beam splitter, arising due to the different lengths in glass encountered by the two beams of the interferometer. The measurement is carried out by first placing the mechanical car with the retro reflector, in the long arm, at the closest possible position to the dichroic mirror. The translation stage in the reference arm is scanned and the spectral interferogram is found and recorded. At this time the path length difference between both arms is around 1.5 m, corresponding to 9 times the half cavity length. Let us label the position of the measurement arm at this position of the retro reflector as A and the distance between the two interfering pulses as L_A. Subsequently for each measurement the mechanical car was moved over a long distance which we label as position B. This long distance was 50 m in our experiments (corresponding to $340 \cdot l_{pp/2}$). At this time the distance between the two interfered pulses is L_B and a new spectral interferogram is recorded. The total displacement of the measurement arm is calculated from Eq. 6.4, where L_A and L_B are obtained by using Eq. 6.9.

6.3.2 Numerical model for analysis

In chapter 4 section 3, we studied that, even though the spectral interferogram is significantly chirped during the long distance propagation in air, the fringe density at the small range around the maximum of the spectral interferogram remains same, as shown in Fig. 4.21. This is reflected on the derivative of the unwrapped phase. Although we used the measured power spectral density for simulations, we show that, it is not necessary to know the entire PSD to get the distance information. We only need the region around the maximum of the PSD and the group velocity of the frequency at the maximum of the PSD.

For this experiment, we obtained the PSD again from the autocorrelation verified using the ocean

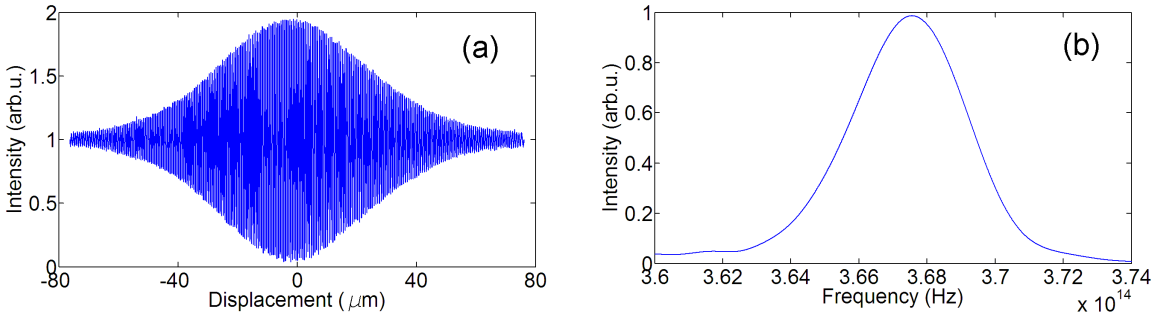

Figure 6.11: (a) Autocorrelation at equal arms. (b) PSD derived from the autocorrelation.

optics spectrometer. The autocorrelation and the derived PSD are shown in Fig. 6.11. Using this PSD, the numerical model implemented plane wave propagation at 10^6 individual frequencies, separated by the repetition frequency, using Edlèn's equation. Spectral interferograms were then calculated using Eq. 4.19. The model takes into account only path length differences and thus only the difference in spectral phase acquired by both arms in air. In Fig. 6.12-(a) we show the spectral interferogram obtained for a path length difference of 2 mm. The calculated spectral interferogram was analyzed using the procedure described in section 6.2.1. This analysis procedure is illustrated in Fig. 6.3. The curve shown in Fig. 6.12-(b) shows distance as a function of ω. We can compare this with the distance which we input into the program, *i.e.* 2 mm. We observe that, Fig. 6.12-(b) is mainly a constant at 2 mm, but has aliasing on both sides due to the Fourier transform.

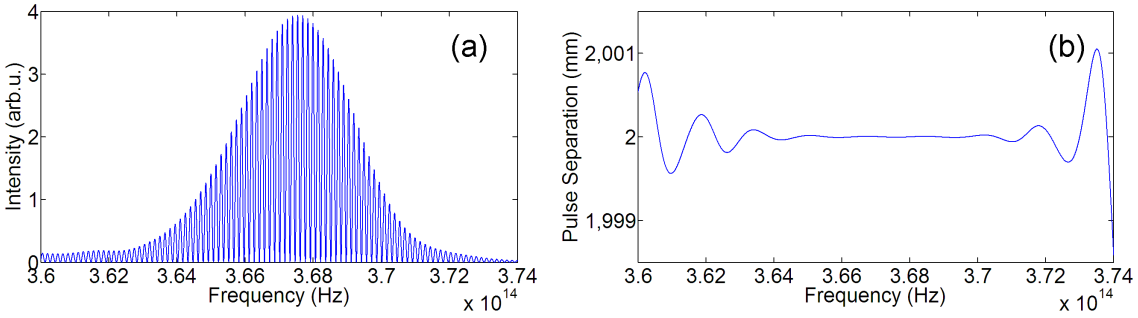

Figure 6.12: (a) Numerically simulated interferogram with path length difference equals to $0 \times L_{pp} \pm 2$ mm. (b) The derived pulse separation as a function of ω.

In Fig. 6.13-(a) and Fig. 6.13-(c) we show the simulated spectral interferograms for the path length difference of $339 \times L_{pp} + 2$ mm and $339 \times L_{pp} - 2$ mm respectively, where L_{pp} is the inter-pulse distance. In our experiments $339 \times L_{pp}$ corresponds to a distance of around 100 m. In Fig. 6.13-(a) the fringes are more separated in the high frequency side and the other way round in Fig. 6.13-(c), but these chirps can hardly be seen from the two figures. The chirp is clearly visible in the figures showing the extracted distances, that is Fig. 6.13-(b) for $339 \times L_{pp} - 2$ mm and Fig. 6.13-(d) for $339 \times L_{pp} + 2$ mm. An increasing or decreasing derivative of the unwrapped phase always means chirp of the spectral interferogram. Here the twin image ambiguity disappears: A decreasing curve in Fig. 6.13-(b) means the path length difference is shorter than $339 \times L_{pp}$. This can be understood by considering that, higher frequency waves propagate slower than lower frequency waves in air. When the path length difference between the two arms is shorter than $339 \times L_{pp}$, the pulse reflected from the long arm is in front of the pulse reflected from the short arm. The high frequency component of the pulse from the long arm are closer to the pulse from the short arm. We see that the central region of the curves in Fig. 6.13-(b) and Fig. 6.13-(d) are approximately linear. This is mainly due to the fact that for a small frequency range around 3.674×10^{14} Hz the refractive index of air is approximately a linear function of frequency.

Although the derived distances in Fig. 6.13-(b) and Fig. 6.13-(d) are functions of the frequency, the distance of 2 mm is always shown at the frequency 3.674×10^{14} Hz, as labelled with the dot in both curves. This fact implies that, for deriving the distance information, it is not necessary to know the entire distance curve in Fig. 6.13-(b) but only the small region around 3.674×10^{14} Hz is interesting. The same derived distance of 2 mm in Fig. 6.13-(b) and Fig. 6.13-(d) at 3.674×10^{14} Hz means the fringe densities in Fig. 6.13-(a) and Fig. 6.13-(c) around the frequency 3.674×10^{14} Hz is the same. These are the regions that we are interested which contain the distance information.

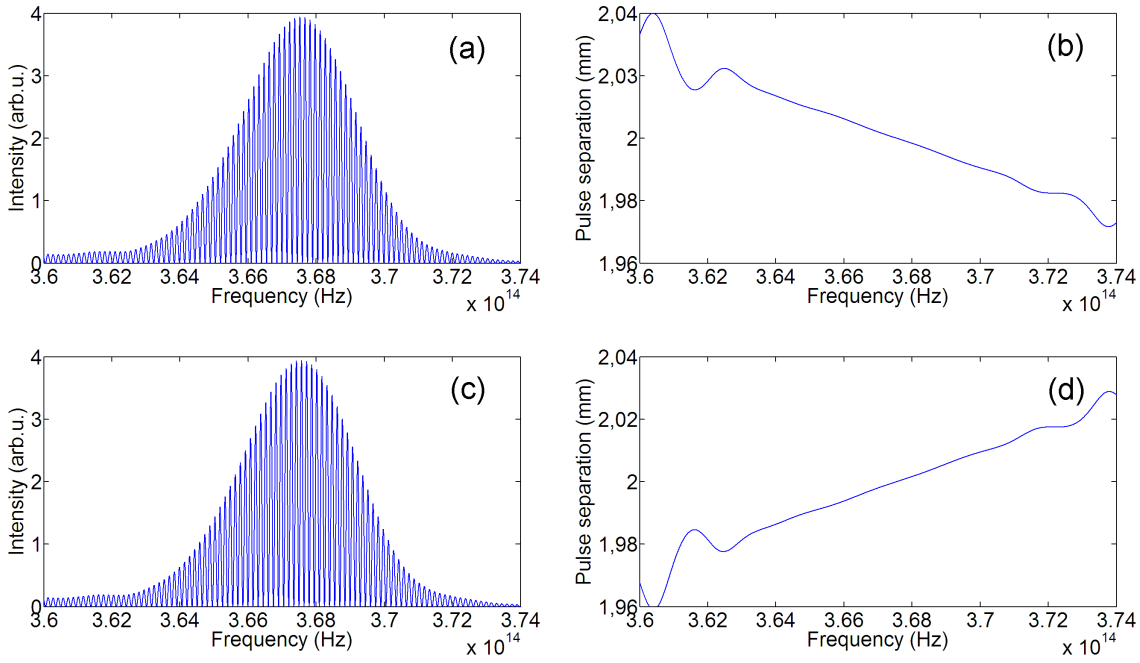

Figure 6.13: (a) Numerically simulated interferogram with path length difference equals to $339\times L_{pp}-2$ mm. (b) The derived pulse separation from the spectral interferogram shown in (a). (c) Numerically simulated interferogram with path length difference equals to $339\times L_{pp}+2$ mm. (d) The derived pulse separation from the spectral interferogram shown in (c).

6.3.3 Calculate the displacement using more frequencies

The distance information is not only contained at the peak frequency of the PSD, but also at other positions on the curve. Actually, the exact distance or path length difference which we measure can be extracted from almost the entire curves shown in Fig. 6.13-(b) and Fig. 6.13-(d), except for the small regions at the edges which have the numerical artifact due to the Fourier transform. In an ultrashort pulse, all frequency components propagate with difference velocities. The interfered fringes on the spectral interferogram, in a particular region in the frequency domain, can be considered as the interference of this particular frequency component, contained within the pulses reflected from both arms. From the previous paragraph we know that, the distance can be derived from a small region of the spectral interferogram around 3.674×10^{14} Hz. Here 3.674×10^{14} Hz is a special frequency not because it is the maximum of the PSD, but because it is the frequency which we used to calculate L_{pp}. Actually, the exact distance or path length difference which we measure can be extracted from almost the entire curves shown in Fig. 6.13-(b), except for the small regions at the edges which have the numerical artifact due to the Fourier transform. We can choose an arbitrary frequency component in Fig. 6.13-(b), but remember that L_{pp} should also be calculated from the frequency we choose.

To illustrate this more clearly, we give an example. Let us select two points from Fig. 6.13-(b), for example, point 1, $f_1 = 3.658\times10^{14}$ Hz $L_1 = 2.009$ mm and point 2, $f_2 = 3.688\times10^{14}$ Hz $L_2 = 1.997$ mm. These two frequencies correspond to two different group refractive indices in air and hence two inter-pulse distances. We have $L_{pp1} = 294.063777$ mm and $L_{pp2} = 294.063742$ mm. The total distance calculated using different frequency components,

$$339\times L_{pp1}-L_1 = 339\times L_{pp2}-L_2 = 99685.611 \quad \text{mm}, \tag{6.16}$$

is the same.

6.3.4 Spectral interferograms at 100 m path length differences

The PSD was first remeasured using the grating spectrometer. The maximum intensity appears at pixel number $x = 1150$. On comparing with the PSD measured with the Fourier transform spectrometer, we know that this corresponds to the frequency of 3.4×10^{14} Hz. We measured the largest path length difference possible ≈50 m in our setup. We recorded the spectral interferograms at several pulse separations, close to $339 \times L_{pp}$. One such spectral interferogram is shown in Fig. 6.14-(a). The reflected beam drops considerably in power, leading to a drop in the modulation depth, but the fringes were clearly visible. The derived pulse separation after calibration is shown in Fig. 6.14-(c). At pixel number $x = 1150$ the read out of the distance $L_B = 0.9455$ mm. The derived pulse separation is decreasing respected to wavelength. This means the path length difference is $339 \times L_{pp} + 0.9455$ mm. The turbulance in air causes the fringes in the spectral interferogram to vibrate, which can be seen in the corresponding curve in Fig. 6.14-(c). This leads to an uncertainty of around 2 μm. The measured spectral interferogram and the derived pulse separation are also compared with simulation. Fig. 6.14-(b) is the simulated spectral interferogram for this distance. To give a good comparison, the x-axis of Fig. 6.14-(b) was chosen to be the wavelength, and the power of the reflected beam was taken to be only 1/10 of the original. The pulse seperation calculated from the simulation is shown in Fig. 6.14-(d). Besides the aliasing on both sides, the central parts of (b) and (d) match quite well, as indicated by the red line in Fig. 6.14-(c).

We also give an example when the path-length difference between the two arms is shorter than $339 \times L_{pp}$. Fig. 6.15-(a) and Fig. 6.15-(c) show the spectral interferogram and the derived pulse separation at $L_B = -2.9228$ mm. The spectral interferometer and the derived curve of the pulse separation is also compared with the simulations, as shown in Fig. 6.15-(c) and Fig. 6.15-(d). The total displacement of the measurement arm is calculated from Eq.3, where L_{pp} is calculated by $L_{pp} = c/n_g f_r$ and n_g is the group refractive index of air at 3.674×10^{14} Hz (816 nm).

6.3.5 Measurement results

During the measurement, the fluctuation of the temperature in the laboratory was controlled to be less than 0.1 °C. The pressure and humidity have been monitored with an accuracy of 1 hPa and 1% respectively. The calibration distance of around 3 mm was used. Each time the translation stage was displaced from pulse separation of -1.5 mm to pulse separation of +1.5 mm., This process is repeated 6 times independently and the averaged calibration distance was used.

Totally 5 groups of long distance measurement were performed. We chose different f_r for each group. Within each group 6 independent measurements were performed. In each measurement, we arbitrarily chose L_1 and L_2 in Eqn.6.4. At each position the spectral interferogram is recorded 5 times to statistically minimize the uncertainty. One 50 m measurement took about 10 minutes, mostly occupied by transporting the retroreflector down the 50 m bench. The measured displacement is compared with measurement of the HeNe fringe counting laser interferometer and the result is shown in Fig. 6.16. The agreement in 5 measurements are all within one wavelength, with the standard deviation of around 1 μm. The average of all measurements shows the agreement within 200 nm on 100 m pulse propagation in air, as shown by the dotted line in Fig. 6.16.

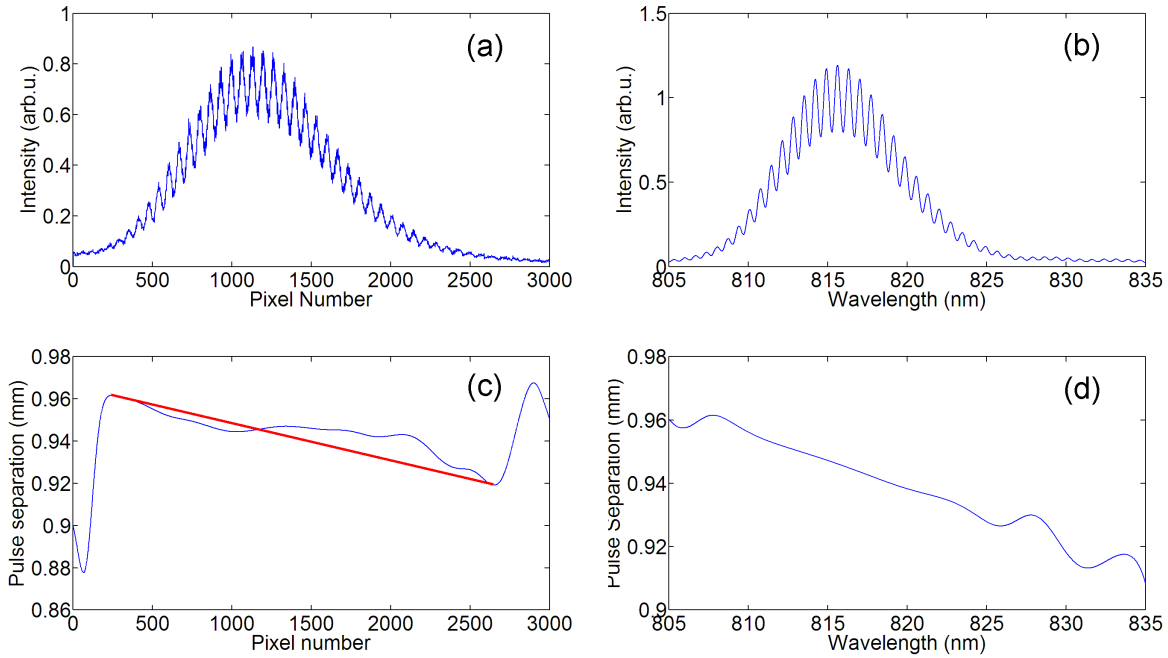

Figure 6.14: (a) A typical measured interferogram with path length difference longer than $339 \times L_{pp}$. (b) The simulated spectral interferogram using $L = 0.9455$ mm. (c) The derived pulse separation from the measurement data in (a). At pixel number $x = 1150$ the read out of the distance $L = 0.9455$ mm. The decreasing slope of the curve indicates a positive sign. (d) The pulse separation calculated from the simulation using $L = 0.9455$ mm.

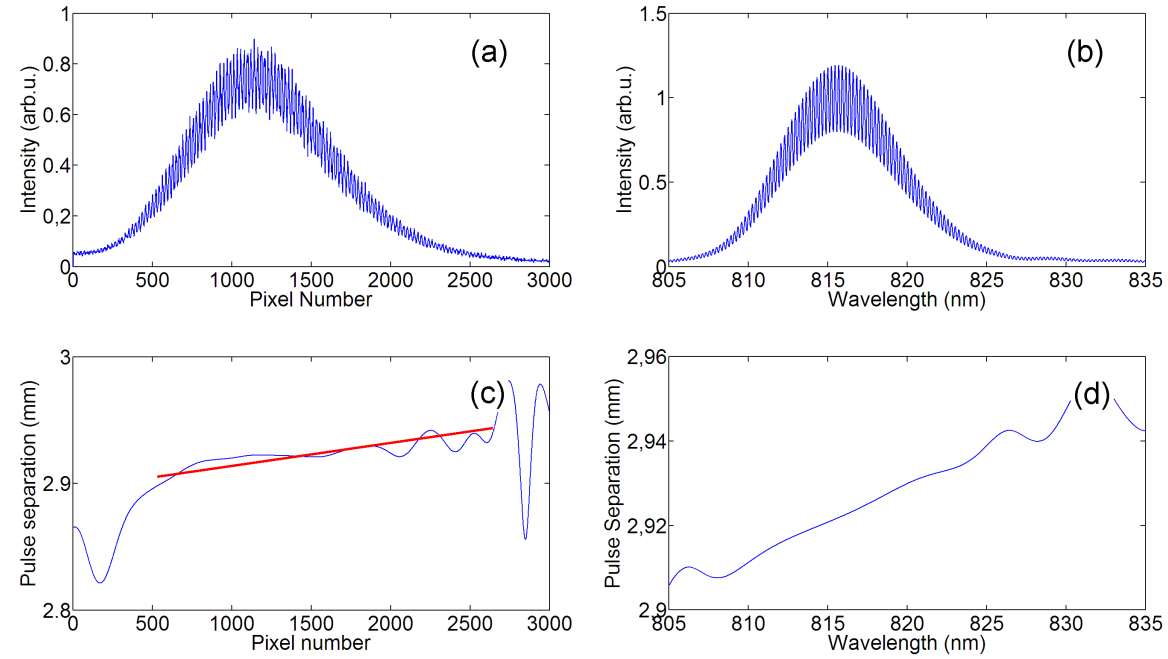

Figure 6.15: (a) A typical measured interferogram with path length difference shorter than $339 \times L_{pp}$. (b) The simulated spectral interferogram using $L = -2.9228$ mm. (c) The derived pulse separation from the measurement data in (a). At pixel number $x = 1150$ the read out of the distance $L = 2.9228$ mm. The increasing slope of the curve indicates a negative sign. (d) The pulse separation calculated from the simulation using $L = -2.9228$ mm.

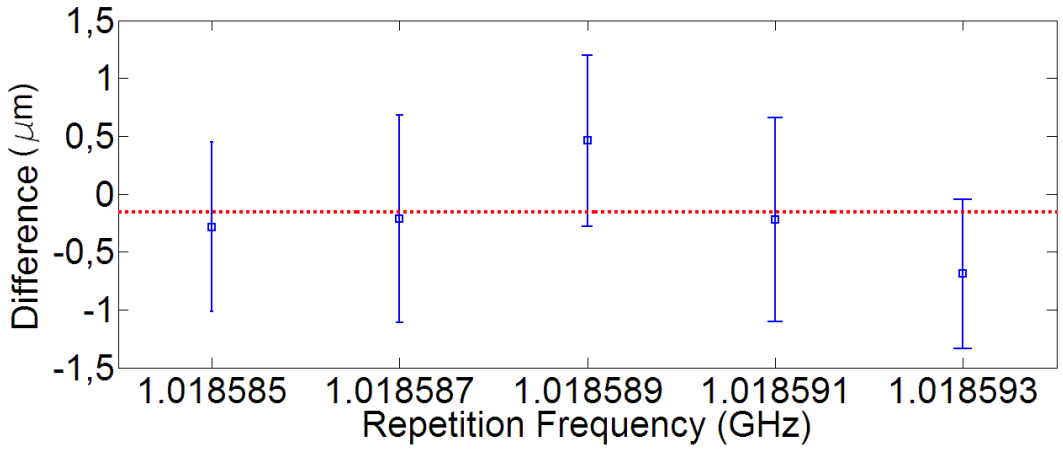

Figure 6.16: Comparison measurement of displacements of around 50 m. The error bars indicate the standard uncertainty, derived from measurement reproducibility. The average of all measurements is shown by the dotted line.

We attribute the residual difference and uncertainty in the comparison measurement to vibrations of the setup and air turbulence. The variation and uncertainty of the environmental parameters, limits the accuracy in measuring the absolute distance. For example, a typical uncertainty of 0.1°C in temperature already leads to an uncertainty of the refractive index of air of about 1×10^{-7}, corresponding to 10 μm at 100 m propagation. Also, an uncertainty of 1 hPa in pressure leads to an uncertainty of 2.7×10^{-7}, corresponding to 26 μm at 100 m propagation. Moreover the updated Edlen's equation itself has an intrinsic uncertainty of 1×10^{-8}, implying 1 μm over a path length difference of 100 m. The influences of the environmental parameters on the refractive index at the wavelengths of both the He-Ne laser and the frequency comb cancel in first order. For this is the reason the agreement between the experimental results is much better than 10 μm. The agreement between the frequency comb and the He-Ne laser is much better than the achievable absolute accuracy in air, showing that the measurement result is not limited by the chosen method.

Chapter 7

Conclusion

In this thesis we have shown two different methods using the femtosecond comb laser as a source for absolute long distance measurement. The first method is based on cross correlations, recorded by periodically moving one arm of the Michelson interferometer. The second one is based on spectral interferograms, recorded by a grating spectrometer.

We built experimental setups to measure distances up to 50 m using both techniques. Both methods have shown that accuracies less than 2 μm can be achieved. The accuracy is not limited by the measurement techniques, but the knowledge of the environment. The uncertainty in determining the refractive index of air becomes the key factor in measuring long distances in air. During the measurement, although the temperature, pressure and humidity were monitored, still the variation and uncertainty on the measurement of these environmental parameters, limits the accuracy in measuring the absolute distances.

If the experiments are performed in outer space, where the refractive index of air is not needed to be taken into account. Then the accuracy will only be influcenced by,

- **The noise properties of the femtosecond laser.** The timing error is defined as the deviation of the temporal pulse position from the corresponding position of a timing reference, which will always be assumed to be noiseless [74–76]. In the frequency domain this is the shift of each repetition frequency from its noiseless position $f_n = nf_r + f_0$ on the frequency axis. For a typical Ti:Sapphire laser locked to the cesium clock, f_r can be stablized within 1 Hz. Let us give an example, if the repetition frequency of the laser is 1 GHz, the timing jitter is 10^{-9} of the repetition frequency. Therefore if the inter-pulse distance is L_{pp} = 30 cm, an uncertainty of 30 nm arises from the timing jitter. Suppose we measure a distance of 15 km in vacuum, that is 10^5 times the half of the inter-pulse distance, the uncertainty in measuring this distance because of the timing jitter is about 30 μm. For commercial on-board femtosecond laser sources the timing jitter is larger than the cesium clock locked Ti:Sapphire laser and will cause larger inaccuracies when measuring long distances in vacuum.

- **The mechanical vibrations of the experimental setup.** This is important, especially with the experiments using the cross correlations. The accuracy of moving the piezo element is one key limit to the measured accuracy.

- **The resolution of the detector.** When the path length difference is very long, the reflected

beam from the measurement arm is expected to be very weak. Hence the sensativity and the resoltion of the detector are important. In the experiments using spectral interferogram, the resolution of the grating spectrometer will limit the measurement accuracy.

- **The calibration of the reference arm.** To measure an arbitrary distance, the short reference arm is needed to accurately calibrated. The reference arm of always less than half of the interpulse distance and can be calibrated accurately by using other technique such as a two wavelength interferometer.

The ultimate maximum distance which can be measured will be limited by the coherence length of the laser source, which depends on the linewidth of the comb lines in the particular comb source. The coherence length of a Ti:Sapphire frequency locked femtosecond laser is of tens of kilometers or more. This is a good property to expect that this method can be applied to measure very long distances, especially in space where the dispersion of air is absent.

Nomenclature

The notations used throughout this thesis are listed in Table 1), represented in the SI units. To complete the nomenclature, all abbreviations used in this thesis are described in a separate list (see Table 2).

Table 1: List of used notations

Symbol	Units	Description
L	m	path length or separation between two interfered pulses
L_m	m	path length of the measurement arm in an interferometer (back and forth)
L_r	m	path length of the reference arm in an interferometer (back and forth)
l_m	m	the length of the measurement arm in an interferometer (single way)
l_r	m	the length of the reference arm in an interferometer (single way)
Δl_m	m	the displacement of the measurement arm in an interferometer
Δl_r	m	the displacement of the reference arm in an interferometer
Δl_c	m	the calibration distance in a spectral dispersive interferometer
L_{pp}	m	the inter-pulse distance or one cavity length
$l_{pp/2}$	m	half of the inter-pulse distance or half cavity length
f_r	Hz	the repetition frequency of the comb laser
ω_r	rad/s	the angular repetition frequency of the comb laser
f_0	Hz	the carrier-envelope offset frequency of the comb laser
ω_0	rad/s	the angular carrier-envelope offset frequency of the comb laser
n_x	–	the refractive index of the x-th frequency or wavelength
n_c	–	the refractive index of the frequency at the center of the PSD
n_p	–	the phase refractive index
n_g	–	the group refractive index
n_{air}	–	the refractive index of air
n_{BK7}	–	the refractive index of BK7
$n(X)$	–	the refractive index as a function of X
n (bare)	–	the mode number in a frequency comb
c	m/s	the speed of light in vacuum
k	$1/m$	wave number
λ	m	wavelength

.....continued on next page.....

Table 1: List of used variables

Symbol	Units	Description
.....		continued from previous page .....
Λ	m	the synthetic wavelength in a two wavelength interferometer
f	Hz	the optical frequency
ω	rad/s	the angular frequency
ω_c	rad/s	the angular frequency at the center of the PSD
E	V/m	the electric field (polarization ignored)
$\|E\|$	V/m	the scalar amplitude of the electric field
ϕ	rad	the phase of the electric field
$\hat{E}$	V/m	the spectrum of the electric field
$\|\hat{E}\|$	V/m	the spectral amplitude
φ	rad	the spectral phase
I	W/m^2	the intensity of the beam
S	V^2/Hz	the power spectral density (PSD)
δ	m	the correction term obtained by comparing the peaks of two cross correlations
d_{chirp}	m	the correction term between the brightest fringe of the cross correlation and a multiple of L_{pp}

Table 2: List of abbreviations

Abbreviation	Description
AC	Achromatic Lens
AOM	Acoustic Optical Modulation
APD	Avalance Photo Diode
BBO	Beta Barium Borate
BS	Beam Splitter
CCD	Charge Coupled Device
CEO	Carrier Envelope Offset
FRAC	Fringe Resolved Auto Correlation
FROG	Frequency Resolved Optical Gating
FWHM	Full Width Half Maximum
GVD	Group Velocity Dispersion
KLM	Kerr Lens Modulation
PDA	Photo Diode Array
PSD	Power Spectral Density
FSR	Free Spectral Range
SHG	Second Harmonic Generation
SPIDER	Spectral Phase Interferometry for Direct Electric-field Reconstruction

..... continued on next page .....

Table 2: List of abbreviations

Abbreviation	Description
.....continued from previous page	
SPM	Self Phase Modulation
TS	Translation Stage
WLS	White Light Source

Bibliography

[1] T. H. Maiman, "Stimulated optical radiation in ruby," Nature **187**, 493 (1960).

[2] A. Javan, W. R. Bennett, and D. R. Herrott, "Population inversion and continuous optical maser oscillation in a gas discharge containing a HeŰNe mixture," Phys. Rev. Lett **6**, 106 (1961).

[3] Z. I. Alferov, V. M. Andreev, E. L. Portnoy, and M. K. Trukan, "AlAs-GaAs heterojunction injection lasers with a low room temperature threshold," Sov. Phys. Semicond. **3**, 1107 (1970).

[4] I. Hayashi, M. B. Panish, P. W. Foy, and S. Sumski, "Junction lasers which operate continuously at room temperature," Appl. Phys. Lett. **17**, 109 (1970).

[5] R. L. Fork, B. I. Greene, and C. V. Shank, "Generation of Optical Pulses shorter than 0.1 ps by Colliding Pulse Modelocking," Applied Physics Letters **38**, 671 (1986).

[6] J. D. Kafka, M. L. Watts, and J. W. J. Pieterse, "Picosecond and femtosecond pulse generation in a regeneratively mode-locked Ti:Sapphire laser," IEEE J. Quantum Electron **28**, 2151 (1991).

[7] D. E. Spence, P. N. Kean, and W. Sibbet, "60-fsec pulse generation from a self-mode-locked Ti:sapphire laser," Optics Letters **16**, 42 (1991).

[8] D. J. Jones, S. A. Diddams, J. K. Ranka, A. Stentz, R. S. Windeler, J. L. Hall, and S. T. Cundiff, "Carrier-Envelope Phase Control of Femtosecond Mode-Locked Lasers and Direct Optical Frequency Synthesis," Science **288**, 635 (2000).

[9] R. Holzwarth, Th. Udem, T. W. Hänsch, J. C. Knight, W. J. Wadsworth, and P. St. J. Russell, "Optical Frequency Synthesizer for Precision Spectroscopy," Phys. Rev. Lett. **85**, 2264 (2000).

[10] S. R. Jefferts, J. Shirley, T. E. Parker, T. P. Heavner, D. M. Meekhof, C. Nelson, F. Levi, G. Costanzo, A. De Marchi, R. Drullinger, L. Hollberg, W. D. Lee, and F. L. Walls, "Accuracy evaluation of NIST F-1," Metrologia **39**, 321 (2002).

[11] S. T. Cundiff, J. Ye, and J. L. Hall, "Optical frequency synthesis based on mode-locked lasers," Rev. Sci. Instr. **72**, 3749 (2001).

[12] T. Udem, J. Reichert, R. Holzwarth, and T. W. Hansch, "Accurate measurement of large optical frequency differences with a mode locked laser," Optics Letters **24**, 881 (1999).

[13] L. S. Ma, Z. Y. Bi, A. Bartels, L. Robertsson, M. Zucco, R. S. Windeler, G. Wilpers, C. Oates, L. Hollberg, and S. A. Diddams, "Optical Frequency Synthesis and Comparison with Uncertainty at the 10^{-19} Level," Science **303**, 1843 (2004).

[14] J. L. Pedersen, S. Herek and A. H. Zewail, "The Validity of the Diradical Hypothesis: Direct Femtosecond Studies of the Transition-State Structures," Science **266**, 1359–1364 (1994).

[15] S. T. Cundiff and J. Ye, "Colloquium: Femtosecond optical frequency combs," Rev. Mod. Phys. **75**, 325 (2003).

[16] K. Minoshima, T. Tomita, Y. Yamaoka, and H. Matsumoto, "Ultrafast Phenomena XIII," , in *Ultrahigh-Resolution distance meter using a frequency comb of a femtosecond mode locked laser.*, D. R. Miller, M. M. Murnane, N.F. Scherer, and A.M. Weiner, eds., vol. XIII, pp. 655–659 (Springer-Verlag, New York, 2003).

[17] J. Ye, "Absolute measurement of a long, arbitrary distance to less than an optical fringe," Opt. Lett. **29**, 1153 (2004).

[18] A. Bartels, C. W. Oates, L. Hollberg, and S. A. Diddams, "Stabilization of femtosecond laser frequency combs with subhertz residual linewidths," Optics Letters **29**, 1081 (2004).

[19] D. W. Rush, P. T. Ho, and G. L. Burdge, "The coherence time of a modelocked pulse train," Optics Communications **52**, 41 (1984).

[20] D. Adam, "Gravity measurement: Amazing grace," Nature **416**, 10 (2002).

[21] C. V. M. Fridlund, "Darwin: The Infrared Space Interferometry Mission," ESA Bulletin **103**, 20 (2000).

[22] R. Irion, "LIGO's Laser-Packing Big Sister LISA May Hunt Black Holes From Space," Science **288**, 422 (2000).

[23] T. Yoshizawa, *Handbook of optical metrology: principles and applications* (CRC Press, Florida, USA, 2009).

[24] K. M. Baira, "The Role of Interferometry in Long Distance Measurement," Metrologia **4**, 135 (1968).

[25] R. Dandliker, R. Thalmann, and D. Prongue, "Two wavelength laser interferometry using superheterodyne detection," Optics Letters **13**, 339 (1988).

[26] R. Dandliker, K. Hug, J. Politch, and E. Zimmermann, "High-accuracy distance measurements with multiple-wavelength interferometry," Opt. Exp. **34**, 2407 (1995).

[27] J. Thiel, T. Pfeifer, and M. Hartmann, "Interferometric measurement of absolute distances of up to 40 m," Measurement **16**, 1 (1995).

[28] D. Xiaoli and S. Katuo, "High-accuracy absolute distance measurement by means of wavelength scanning heterodyne interferometry," Meas. Sci. Technol. **9**, 1031 (1998).

[29] B. L. Swinkels, N Bhattacharya, and J. J. M. Braat, "Correcting movement errors in frequency-sweeping interferometry," Opt. Lett. **30**, 2242 (2005).

[30] S. Diddams and J. C. Diels, "Dispersion measurements with white light interferometry," J. Opt. Soc. Am. B **13**, 1120 (1996).

[31] U. Schnell, E. Zimmermann, and R. Dandliker, "Absolute distance measurement with synchronously sampled white-light channelled spectrum interferometry," Pure Appl. Opt. **4**, 643 (1995).

[32] M. Born and E. Wolf, *Principles of Optics*, 7th ed. (Cambridge University Press, Cambridge, 1999).

[33] B. Edlén, "The Refractive Index of Air," Metrologia **2**, 71 (1966).

[34] K. P. Birch and M. J. Downs, "An Updated Edlén Equation for the Refractive Index of Air," Metrologia **31**, 155 (1993).

[35] K. P. Birch and M. J. Downs, "Correction to the Updated Edlén Equation for the Refractive Index of Air," Metrologia **31**, 315 (1994).

[36] P. E. Ciddor, "Refractive index of air: new equations for the visible and near infrared," Applied Optics **35**, 1566 (1996).

[37] P. E. Ciddor and J. Hill, "Refractive Index of Air: 2. Group Index," Applied Optics **38**, 1163 (1999).

[38] Ciddor P. E., "Refractive index of air: 3. The roles of CO2, H2O, and refractivity virials," Applied Optics **41**, 2292 (2002).

[39] G. Bonsch and E. Potulski, "Measurement of the refractive index of air and comparison with modified Edlén's formulae," Metrologia **35**, 133 (1998).

[40] W. Sellmeier, "Zur Erklärung der abnormen Farbenfolge im Spectrum einiger Substanzen," Annalen der Physik und Chemie **219**, 272 (1871).

[41] J. C. Diels and W. Rudolph, *Ultrashort Laser Pulse Phenomena, Second Edition*, 2nd ed. (Elsevier Inc., Burlington, USA, 2006).

[42] A. Yariv, "Internal modelation in multimode laser oscillators," J. Appl. Phys. **36**, 388 (1965).

[43] D. J. Kuizenga and A. E. Siegman, "FM and AM Mode Locking of the Homogeneous Laser - Part I: Theory," IEEE J. of Quantum Electron **6**, 694 (1970).

[44] H. A. Haus, "Theory of Mode Locking with a Slow Saturable Absorber," IEEE J. of Quantum Electron **11**, 736 (1975).

[45] H. A. Haus, "Theory of Mode Locking with a fast Saturable Absorber," Appl.Phys. **46**, 3049 (1975).

[46] T. Hirayama and M. Sheik-Bahae, "Real-time chirp diagnostic for ultrashort laser pulses," Optics Letters **27**, 860 (2002).

[47] K. E. Oughstun and N. A. Cartwright, "Physical significance of the group velocity in dispersive, ultrashort gaussian pulse dynamics," Journal of Modern Optics **52**, 1089 (2005).

[48] K. E. Oughstun, "Gaussian Pulse Propagation in a Dispersive, Absorbing Dielectric," Physical Review Letters **77**, 2210 (1996).

[49] X. Hong and K. E. Oughstun, "Failure of the group-velocity description for ultrawideband pulse propagation in a causally dispersive, absorptive dielectric," J. Opt. Soc. Am. B **16**, 1773 (1999).

[50] K. L. Sala, G. Kenney-Wallace, and G. E. Hall, "CW Autocorrelation Measurements of picosecond laser pulses," IEEE J. Quantum Electron. **16**, 990 (1980).

[51] J. C. Diels, J. J. Fontaine, and F. Simoni, "Control and Measurement of Ultrashort Pulse Shapes (in Amplitute and Phase) with Femtosecond Accuracy," Applied Optics **24**, 1270 (1985).

[52] C. Iaconis and I. A. Walmsley, "Self-Referencing Spectral Interferometry for Measring Ultrashort Optical Pulses," IEEE Journal of Quantum Electronics **35**, 501 (1999).

[53] C. Dorrer and I. A. Walmsley, "Precision and consistency criteria in spectral phase Interferometry for direct electric-field reconstruction," J. Opt. Soc. Am. B **19**, 1019 (2002).

[54] K. W. DeLong, R. Trebino, J. Junter, and W. E. White, "Frequency resolved optical grating using second harmonic generation," J. Opt. Soc. Am. B **11**, 2206 (1994).

[55] D. N. Fittinghoff, J. L. Bowie, J. N. Sweetser, R. T. Jennings, M. A. Krumbuegel, K. W. Delong, R. Trebino, and I. A. Walmsley, "Measurement of the intensity and phase of ultraweek, ultrashort laser pulses," Opt. Lett. **21**, 884 (1996).

[56] K. N. Joo and S. W. Kim, "Absolute distance measurement by dispersive interferometry using a femtosecond pulse laser," Opt. Exp. **14**, 5954 (2006).

[57] K. N. Joo, Y. Kim, and S. W. Kim, "Distance measurements by combined method based on a femtosecond pulse laser," Opt. Exp. **16**, 19799 (2008).

[58] Y. Salvade, N. Schuhler, S. Leveque, and S. Le Floch, "High-accuracy absolute distance measurement using frequency comb referenced multiwavelength source," Appl. Opt. **47**, 2715 (2008).

[59] S. Hyun, Y. J. Kim, Y. Kim, J. Jin, and W. Kim, S, "Absolute length measurement with the frequency comb of a femtosecond laser," Meas. Sci. Technol. **20**, 095302 (2009).

[60] I. Coddington, W. C. Swann, L. Nenadovic, and N. R. Newbury, "Rapid and precise absolute distance measurements at long range," Nature Photonics **3**, 351 (2009).

[61] P. Balling, P. Křen, P. Mašika, and S. A. van den Berg, "Femtosecond frequency comb based distance measurement in air," Opt. Exp. **17**, 9300 (2009).

[62] D. Wei, S. Takahashi, K. Takamasu, and H. Matsumoto, "Femtosecond optical frequency comn based tandem interferometer," Journal of the European Optical Society - Rapid Publications **4**, 09043 (2009).

[63] K. Minoshima and H. Matsumoto, "High-accuracy measurement of 240 m distance in an optical tunnel by using of a compact femtosecond laser," Appl. Opt. **39**, 5512 (2000).

[64] L. Lepetit, G. Cheriaux, and M. Joffre, "Linear techniques of phase measurement by femtosecond spectral interferometry for applications in spectroscopy," J. Opt. Soc. Am. B **12**, 2467 (1995).

[65] E. Tokunaga, A. Terasaki, and T. Kobayashi, "Frequency domain interferometer for femtosecond time resolved phase spectroscopy," Optics Letters **17**, 1131 (1992).

[66] D. Reolon, I. Verrier, C. Veillas, G. Brun, and M. Jacquot, "Investigation of spectral interferometry for refractive index measurement and for lens aberations characterization," Optics Communications **281**, 4230 (2008).

[67] M. G. Zeitouny, M. Cui, N. Bhattacharya, H. P. Urbach, S. A. van den Berg, and A. J. E. M. Janssen, "From a discrete to a continuous model for interpulse interference with a frequency-comb laser," Phys. Rev. A .

[68] M. Cui, R. N. Schouten, N. Bhattacharya, and S. A. van den Berg, "Experimental demonstration of distance measurement with a femtosecond frequency comb laser," J. Eur. Opt. Soc. Rapid Publ. **3**, 08003 (2008).

[69] M. Cui, M. G. Zeitouny, N. Bhattacharya, S. A. van den Berg, H. P. Urbach, and J. J. M. Braat, "High-accuracy long-distance measurements in air with a frequency comb laser," Opt. Lett. **34**, 1982 (2009).

[70] C. Dorrer, N. Belabas, J. P. Likforman, and M. Joffre, "Spectral resolution and sampling issues in Fourier-transform spectral interferometry," J. Opt. Soc. Am. B **17**, 1795 (2000).

[71] M. Takeda, H. Ina, and S. Kobayashi, "Fourier-transform method of fringe-pattern analysis for computer-based topography and interferometry," J. Opt. Soc. Am. **72**, 156 (1982).

[72] C. Dorrer, "Influence of the calibration of the detector on spectral interferometry," J. Opt. Soc. Am. B **16**, 1160 (1999).

[73] E. Hecht, *Optics*, 3rd ed. (Addison Wesley Longman, Inc., Reading, MA, 1998).

[74] R. Paschotta, A. Schlatter, S. C. Zeller, H. R. Telle, and U. Keller, "Optical phase noise and carrier envelope offset noise of mode locked lasers," Applied Physics B **82**, 265 (2006).

[75] R. Paschotta, "Noise of mode-locked lasers (Part 1): numerical model," Applied Physics B **79**, 153 (2004).

[76] R. Paschotta, "Noise of mode-locked lasers (Part 2): timing jitter and other fluctuations," Applied Physics B **79**, 163 (2004).

Summary

This thesis is about interferometric distance measurement using ultrashort pulses, with linear measurement techniques in a dispersive medium. Several fields of expertise are combined here: ultrashort pulse propagation in dispersive media, distance measurement interefometry and linear measurement techniques. All our measurements can be mainly classified into two interferometers we built as a part of this work. The two interferometers share somethings in common but also differs: They shared the same femtosecond laser source; both had 50 m long path length differences between the two arms. The detected signals from the two methods are quite different: one is cross correlations, with measured intensity as a time sequence, and the other is spectral interferograms, measured by a grating spectrometer. But the information obtained from the two detection methods are the same: The PSD and the path length difference at certain enviroment conditions.

Although the information we obtain from a linear technique is limited, it is enough, or sometimes more than enough to extract the path length difference of the two arms. For example if the measurement is performed in vacuum, where the inter-pulse distance is only determined by the repetition frequency and the speed of light in vacuum. Then cross correlation will always be the same as an autocorrelation, and the spectral interferograms will never be chirped. The PSD is not necessary to extract the path length difference because the spectral component does not contribute to the measured distance. At this time, the deviation factor d_{chirp} in chapter 5 is always zero and the derivative of the unwrapped phase in chapter 6 is always a constant.

When the measurement is performed in air, each frequency now has its own refractive index and hence its own velocity. The situation becomes complex because the effect of the dispersion strongly depends on those frequencies we are observing. The ways to extract the path length differences from the cross correlations and the spectral interferograms are quite different: In the cross correlation technique, each point in a cross correlation is the intensity of the weighted combination of all the frequencies. Then a complete knowledge of the PSD is necessary to perdict the shape of the cross correlations hence derive the path length difference. In the spectral interferometry method, we can concentrate at one particular frequency where the modulated spectrum around this frequency is only determined by the interfering of this particular frequency component in the PSD. Thus the global knowledge of the PSD is not necessary to be known.

In this research, we investigated a new way of measuring long distances with stablized femtosecond pulses. In the end, we need to say that our research is only the first step. When this technique is developed for practical uses, for example, in space missions, many adaptions will be undertaken and many more factors will be considered. Fortunately, while the author finishing this thesis, more compact, stable and cheaper femtosecond pulse sources are being made available all around the world. Our theoretical and experimental research will be the footsteps for future researchers.

Samenvatting

In deze dissertatie staan interferometrische afstandsmetingen centraal waarbij gebruik wordt gemaakt van ultrakorte pulsen met lineaire meettechnieken in dispersieve media. Verschillende expertisegebieden zijn hierbij gecombineerd: ultrakortegolf-propagatie in dispersieve media, interferometrische afstandsmetingen, en lineaire meettechnieken. Als onderdeel van het project zijn twee typen inferometers gebouwd waarop alle metingen zijn uitgevoerd. De twee typen interferometers hebben gezamenlijke aspecten maar verschillen ook van elkaar: zo maken ze gebruik van dezelfde femtosecond laserbron en hebben beide een weglengteverschil tussen de twee armen van 50 meter. Verschillend zijn de gedetecteerde signalen bij de twee methoden: bij de ene betreft het kruiscorrelaties met een gemeten intensiteit als tijdsequentie, bij de andere bestaat het signaal uit spectrale interferogrammen welke gemeten zijn met een grating spectrometer. De informatie die wordt afgeleid uit de twee detectiemethoden is echter gelijk: de PSD en het weglengteverschil bij bepaalde omgevingscondities.

Hoewel de verkregen informatie uit een lineaire techniek beperkt is, is die voldoende, en soms meer dan genoeg, voor het bepalen van de weglengteverschillen in de twee armen. Bijvoorbeeld als de meting in vacuüm wordt uitgevoerd, waarbij de onderlinge pulsafstand alleen maar wordt bepaald door hun herhalingsfrequentie en de snelheid van het licht in vacuüm. In dat geval zal een kruiscorrelatie altijd gelijk zijn aan een autocorrelatie en de spectrale interferogrammen zullen nooit ge-'chirped' zijn. De PSD is niet nodig om een weglengteverschil te bepalen omdat de spectrale component niet bijdraagt aan de gemeten afstand. Op dit moment is de afwijkingsfactor d_{chirp} in hoofdstuk 5 altijd gelijk aan nul en is de afgeleide van de 'unwrapped phase' in hoofdstuk 6 altijd een constante.

Wanneer de meting in lucht wordt uitgevoerd heeft elke frequentie zijn eigen brekingsindex en dus zijn eigen snelheid. De situatie wordt gecompliceerd omdat het effect van dispersie sterk afhangt van de geobserveerde frequentie. De manieren om de weglengteverschillen te bepalen uit de kruiscorrelaties en de spectrale interferogrammen zijn wezenlijk verschillend: bij de kruiscorrelatietechniek is ieder punt in een kruiscorrelatie de intensiteit van de gewogen combinatie van alle frequenties. Vervolgens is volledige kennis vereist van de PSD om de vorm van de kruiscorrelaties te voorspellen en daarmee het weglengteverschil. Bij de spectrale interferometrie methode kunnen we ons concentreren op één specifieke frequentie, waarbij het gemoduleerde spectrum rondom deze frequentie alleen wordt bepaald door de mate waarin deze specifieke frequentiecomponent met de PSD interfereert. Volledige kennis van de PSD is dan ook niet noodzakelijk.

In dit onderzoek hebben wij een nieuwe manier voor het meten van lange afstanden met gestabiliseerde femtosecondpulsen onderzocht. Hierbij vermelden we dat ons onderzoek een eerste stap is. Wanneer deze techniek verder wordt ontwikkeld voor praktische toepassingen, bijvoorbeeld in ruimtevaartmissies, zullen er veel aanpassingen nodig zijn en zal er met veel meer factoren rekening gehouden moeten worden. Het is erg positief dat, op het moment van het afronden van deze

dissertatie, er een groeiend aantal compacte, stabiele en goedkopere femtosecond pulsbronnen verkrijgbaar zijn. Ons theoretisch en experimentele onderzoek zal fungeren als voetstappen voor toekomstige onderzoekers.

Acknowledgments

At the end of my four year Ph.D career I would like to say my thanks to many people who have helped me finish this research, in many different ways.

First I would like to thank to **Prof. Joseph Braat** who gave the original proposal of this work and accepted me as a PH.D student. The discussions with him in my first two years helped me a lot in understanding basics of the project.

I would like to thank to **Prof. Paul Urbach**, who succeeded Prof.J.J.M Braat as the leader of Optics group in my third year. I received not only knowledge from him, but also encouragement and support.

I am specially indebted to **Nandini Bhattacharya**. She shared a lot of her experience with me in every part of my research: how to order optical equipment; how to write a good paper; how to give a good presentation, how to write a good thesis. The most important, we worked together on the 50 m bench and collected very useful data.

I would like to thank to **Steven van den Berg**. He gave me enormous help in using his facilities and we had quite a lot of useful discussions on understanding the whole theory of this project.

I would like to thank to my colleague **Mounir Zeitouny**. He made very useful programs and brought new ideas into this project. I also thank my colleagues **Bas Swinkels** and **Adonis Reyes**, who gave me some useful suggestions.

I have benefited a lot from the discussion with people outside the optics group of TU-Delft. I would like to thank **Peter Baling** from Czech Metrology Institute, **Stefan Persijn** from VSL and **Ki-nam Joo** from Korea Advanced Institute of Science and Technology.

Thanks to all the technicians in TU-Delft, including **Roland**, **Raymond**, **Rob**, **Thim** and **Marnix**, for their help on testing and preparing experimental setups.

Thanks to the secretary in TU-Delft, **Yvonne** and **Lucia**, for their help on buying optical components and their other useful jobs.

Thanks to the secretary in FOM, **Maria** and **Annette**, for their help on extending my ID and arrange my FOM courses.

Thanks to my roommates **Oana**, **Maarten**, **Mounir**, **Gopakumar** and **Alessandro** who gave me helps and always made me laugh. Thanks to **Pascal** and **Peter** for the translation and correction of the summary into Dutch.

Thanks to all members of optics TU-Delft for a very social and warm group.

Thanks to the scientists and technicians in VSL who shared the lab with me.

Futher more, I want to thanks to all my friends for their companion and support.

I am indebted to my Parents, **Zheng Cui** and **Guizhen Zheng**, who make me up to this far. I am very proud of being your son. Thanks to my Grandma, **Qi Cui**, I will always remember the love and support from you.

I express my gratefulness to my beloved wife, **Eugenia Ma**. Thank you for your love, care and support in the last four years.

Curriculum Vitae

Moxi Cui was born in 1979 in Beijing, People's Republic of China. In 2002, he graduated from the Nankai University of China with a B.S. in Applied Optics. In the year 2003 he came to the Netherlands and joined the Master's program in the Delft University of Technology. His master's dissertation was on the optimization of the output of Organic Light Emitting Diode, for which he worked at the Philips Research Laboratory in Eindhoven. In 2006 he acquired a master's degree and started his Ph.D in the optics group, TU-Delft. During this period, he was employed by Stichting for Fundamenteel Onderzoek der Materie (FOM). The research conducted during his Ph.D study in Optics group TU-Delft and VSL is basis of this thesis. The results of his ph.D studies have been published in several refereed papers and presented in several international conferences. Starting from September 2010, he is a post-doc researcher in Netherlands Institute for Space Research (SRON).

List of Publications

Refereed publications

1. "Experimental demonstration of distance measurement with a femtosecond frequency comb laser", M. Cui, R. N. Schouten, N. Bhattacharya and S. A. van den Berg, J.E.O.S. - Rapid Publications **3** 08003 (2008)

2. "High Accuracy Long Distance Measurements in Air with a Frequency Comb Laser ", M. Cui, M. G. Zeitouny N. Bhattacharya, S. A. van den Berg, H. P. Urbach, and J. J. M. Braat, Optics Letters, vol. **34**, issue 13, p. 1982 (2009)

3. "Distance measurement with fs pulses using a dispersive interferometer", M. Cui, M. G. Zeitouny N. Bhattacharya, S. A. van den Berg, H. P. Urbach, In preparation (2010)

4. "From a discrete to a continuous model for inter-pulse interference with a frequency comb laser", M. G. Zeitouny, M. Cui, N. Bhattacharya, H. P. Urbach, S. A. van den Berg and A. J. E. M. Janssen, Physical Review A., vol. **82**, issue 2, 023808 (2010)

5. "Asymptotic analysis of inter-pulse interference from a frequency comb for large delay distances via the method of stationary phase", M. G. Zeitouny, M. Cui, N. Bhattacharya, H. P. Urbach, S. A. van den Berg and A. J. E. M. Janssen, In preparation (2010)

6. "Optimization of light extraction from OLEDs", Moxi Cui, H. Paul Urbach and Dick K. G. de Boer, Optics Express, Vol. 15, Issue 8, pp. 4398-4409 (2006)

Conference presentations

1. "Absolute Distance Measurement Using a Mode Locked Femtosecond Pulse Laser", M. Cui, S. A. van de Berg, N. Bhattacharya, Apr. 2008, Utrecht, EOS photonics

2. "Frequency comb based long distance measurement in air", M. Cui, M. G. Zeitouny, N. Bhattacharya, H. P. Urbach, S. A. van den Berg, Sep. 2009, Capri, 1st EOS Topical Meeting on Laser

3. "Long distance measurement with a frequency comb laser", M. Cui, M. Zeitouny, N. Bhattacharya, H. P. Urbach, and S. A. van den Berg, Oct. 2009, Lunteren, 33rd annual meeting NNV AMO

4. "New laser system for distance metrology", M. Cui, M. G. Zeitouny, N. Bhattacharya, S. A. van den Berg, H. P. Urbach, Jun. 2010, Chengdu, SOPO2010

Poster presentations (1st author only)

1. "Absolute Distance Measurement Using a Frequency Comb", M. Cui, S. A. van den Berg, J. J. M. Braat, N. Bhattacharya, Oct. 2006, Paris, EOS annual

2. "Correlation Functions Formed by a Femtosecond Pulse Interferometer", M. Cui, S. A. van den Berg, N. Bhattacharya, H. P. Urbach, Jun. 2008, Marseille, SPIE

3. "Cross-correlation Functions from Ultrafast Pulses for Absolute Distance Measurements", M. Cui, M. Zeitouny, N. Bhattacharya, S. A. van den Berg, H. P. Urbach, Sep. 2008, Paris, EOS anuual

4. "Distance Measurement in Air with a Femtosecond Frequency Comb", M. Cui, M. G. Zeitouny N. Bhattacharya, S. A. van den Berg, and H. P. Urbach, May. 2009, Munich, CLEO Europe

Magazines

1. "New laser system for distance metrology", M. Cui, M. G. Zeitouny, N. Bhattacharya, S. A. van den Berg, H. P. Urbach, Jun. 2009, FOTONICA magazine